COPERNICUS SPACE COMPONENT SENTINEL OPTICAL IMAGING

MISSION PERFORMANCE CLUSTER SERVICE

Data Quality Report

Sentinel-3 OLCI

July 2023

Ref.: OMPC.ACR.DQR.03.07-2023

Issue: 1.0

Date: 31/08/2023

Contract: 4000136252/21/I-BG

Customer: ESA		**Document Ref.:**	OMPC.ACR.DQR.03.07-2023
Contract No.: 4000136252/21/I-BG		**Date:**	31/08/2023
		Issue:	1.0

Project:	COPERNICUS SPACE COMPONENT SENTINEL OPTICAL IMAGING MISSION PERFORMANCE CLUSTER SERVICE		
Title:	Data Quality Report - OLCI		
Author(s):	OLCI ESL team		
Approved by:	L. Bourg, OPT-MPC OLCI ESL Coordinator S. Clerc, OPT-MPC Optical ESL Coordinator	**Authorized by**	C. Hénocq, OPT-MPC S3 Technical Manager
Distribution:	ESA, EUMETSAT, published in Sentinel Online		
Accepted by ESA	S. Dransfeld, ESA TO		
Filename	OMPC.ACR.DQR.03.07-2023 - i1r0 - OLCI DQR July 2023.docx		

Changes Log

Version	Date	Changes
1.0	31/08/2023	First version

List of Changes

Version	Section	Answers to RID	Changes

Table of content

List of Figures

List of Tables

1 Processing Baseline Version

1.1 Sentinel3-A

IPF	IPF / Processing Baseline version	Date of deployment
OL1	06.17 / OL__L1_.003.03.00 (with uncertainties activated)	25/07/2023
OL2 LAND	06.18 / OL__L2L.002.11.02	25/07/2023
SY2	06.25 / SYN_L2_.002.18.01	25/07/2023
SY2_VGS	06.12 / SYN_L2V.002.09.01	25/07/2023
SY2_AOD	01.08 / AOD_NTC.002.08.01	25/07/2023

1.2 Sentinel3-B

IPF	IPF / Processing Baseline version	Date of deployment
OL1	06.17 / OL__L1_.003.03.00 (with uncertainties activated)	18/07/2023
OL2 Land	06.18 / OL__L2L.002.11.02	18/07/2023
SY2	06.25 / SYN_L2_.002.18.01	18/07/2023
SY2_VGS	06.12 / SYN_L2V.002.09.01	18/07/2023
SY2_AOD	01.08 / AOD_NTC.002.08.01	18/07/2023

2 Instrument monitoring

2.1 CCD temperatures

2.1.1 OLCI-A

The long-term monitoring of the CCD temperatures is based on Radiometric Calibration Annotations (see Figure 1). Variations are very small (0.09 C peak-to-peak) and no trend can be identified. Data from current reporting period (rightmost data points) do not show any specificity.

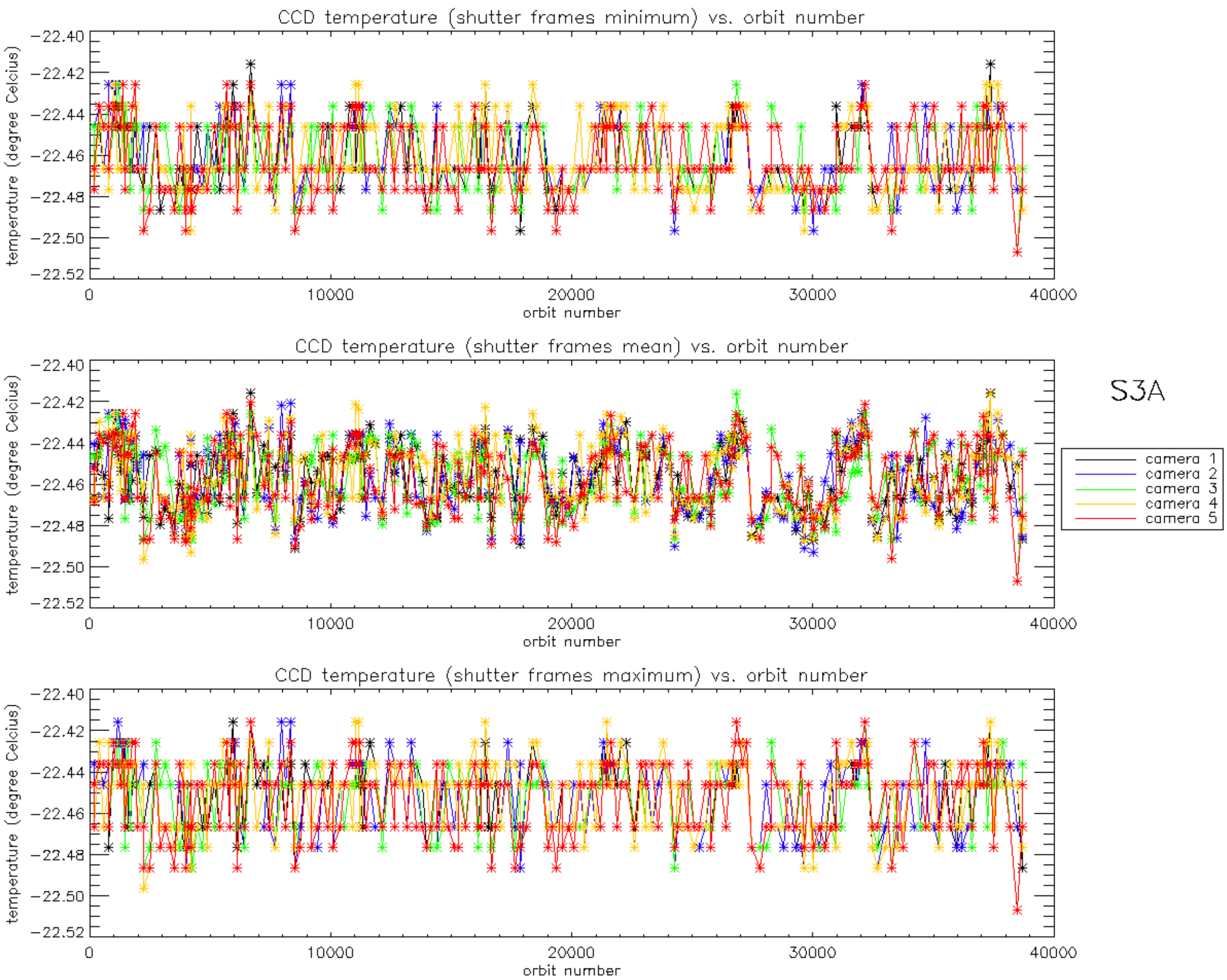

Figure 1: long term monitoring of OLCI-A CCD temperatures using minimum value (top), time averaged values (middle), and maximum value (bottom) provided in the annotations of the Radiometric Calibration Level 1 products, for the shutter frames, all radiometric calibrations so far except the first one (absolute orbit 183) for which the instrument was not yet thermally stable.

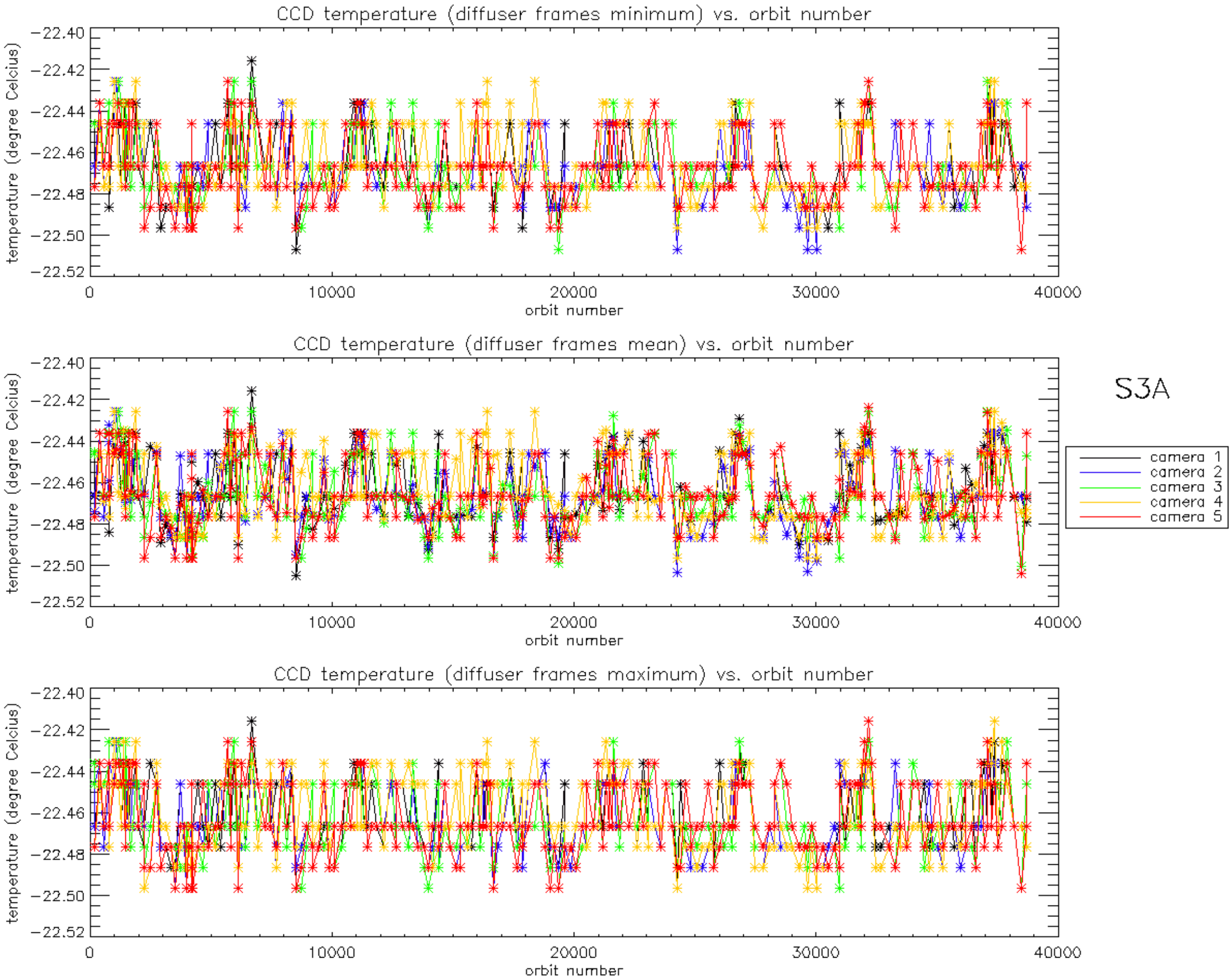

Figure 2: Same as Figure 1 for diffuser frames.

2.1.2 OLCI-B

As for OLCI-A, the variations of CCD temperature are very small (0.08 C peak-to-peak) and no trend can be identified. Data from current reporting period (rightmost data points) do not show any specificity.

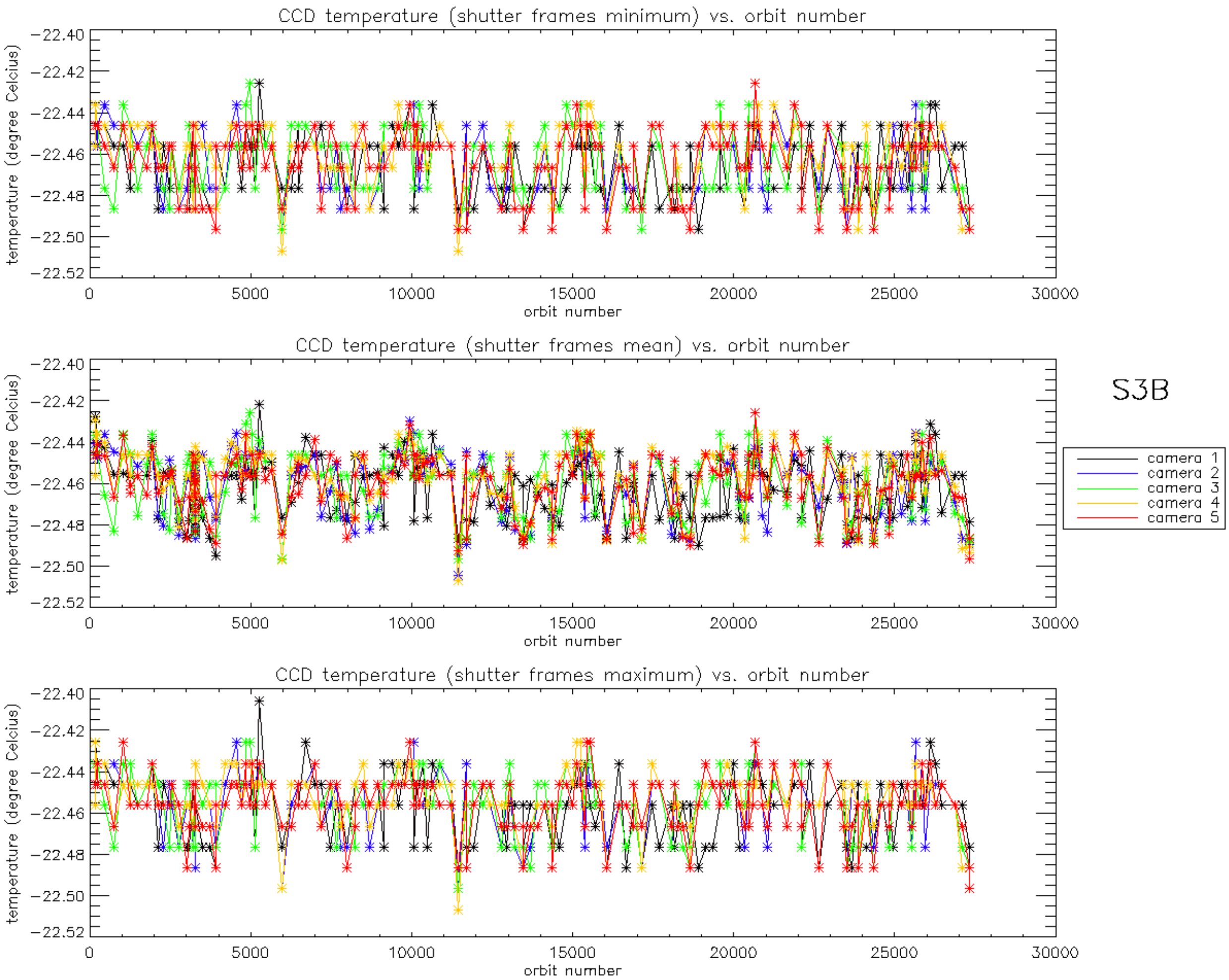

Figure 3: long term monitoring of OLCI-B CCD temperatures using minimum value (top), time averaged values (middle), and maximum value (bottom) provided in the annotations of the Radiometric Calibration Level 1 products, for the Shutter frames, all radiometric calibrations so far except the first one (absolute orbit 167) for which the instrument was not yet thermally stable.

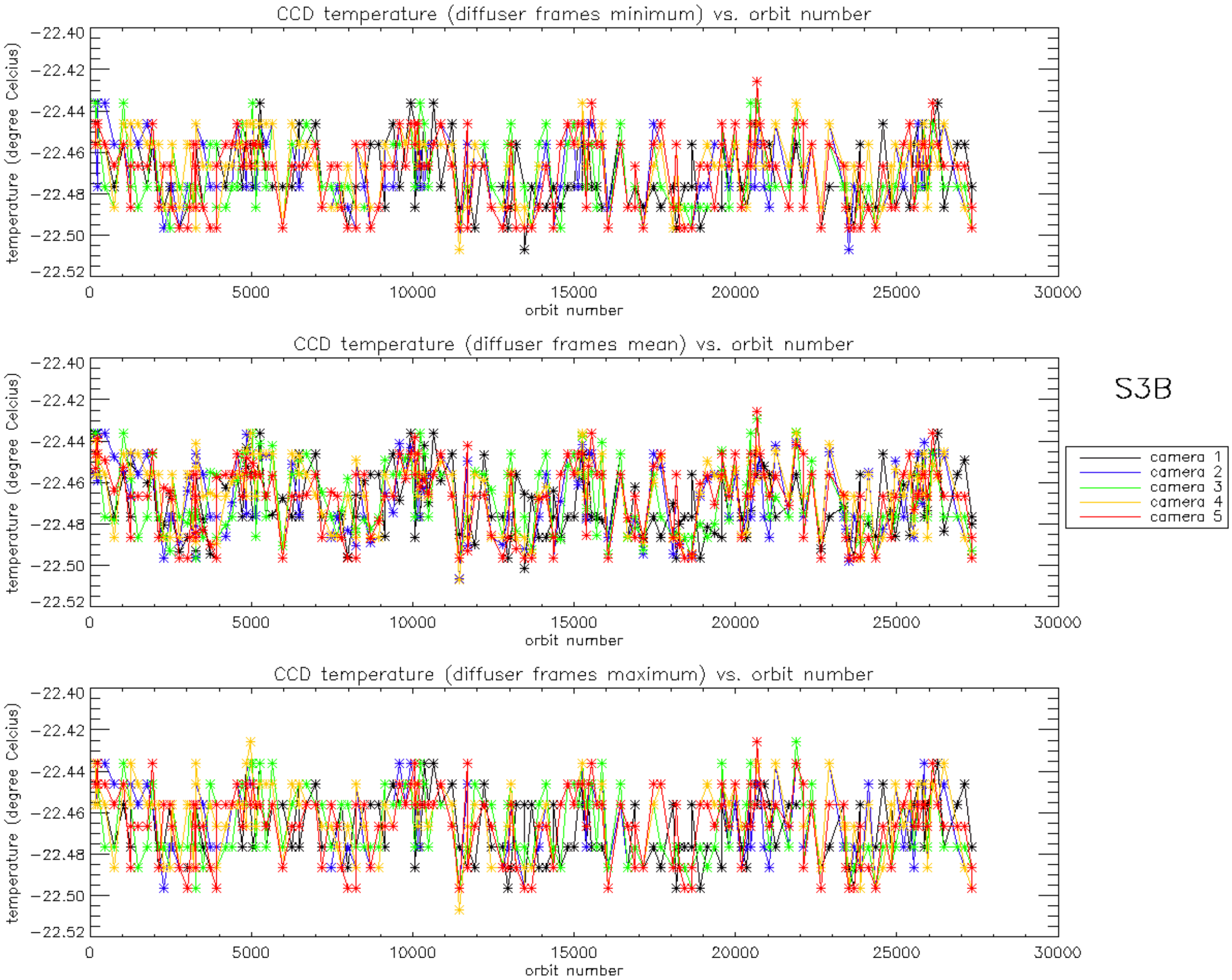

Figure 4: same as Figure 3 for diffuser frames.

2.2 Radiometric Calibration

For OLCI-A, three Radiometric Calibration sequences have been acquired during the reported period:

- S01 sequence (diffuser 1) on 06/07/2023 23:28 to 23:30 (absolute orbit 38460)
- S01 sequence (diffuser 1) on 23/07/2023 00:55 to 00:57 (absolute orbit 38689)
- S05 sequence (diffuser 2) on 23/07/2023 02:36 to 02:38 (absolute orbit 38690)

For OLCI-B, three Radiometric Calibration sequences have been acquired during the reported period:

- S01 sequence (diffuser 1) on 09/07/2023 01:19 to 01:21 (absolute orbit 27096)
- S01 sequence (diffuser 1) on 24/07/2023 21:43 to 21:45 (absolute orbit 27322)
- S05 sequence (diffuser 2) on 24/07/2023 23:24 to 23:26 (absolute orbit 27323)

The acquired Sun azimuth angles are presented on Figure 5 for OLCI-A and Figure 6 for OLCI-B, on top of the nominal values without Yaw Manoeuvre (i.e. with nominal Yaw Steering control of the satellite).

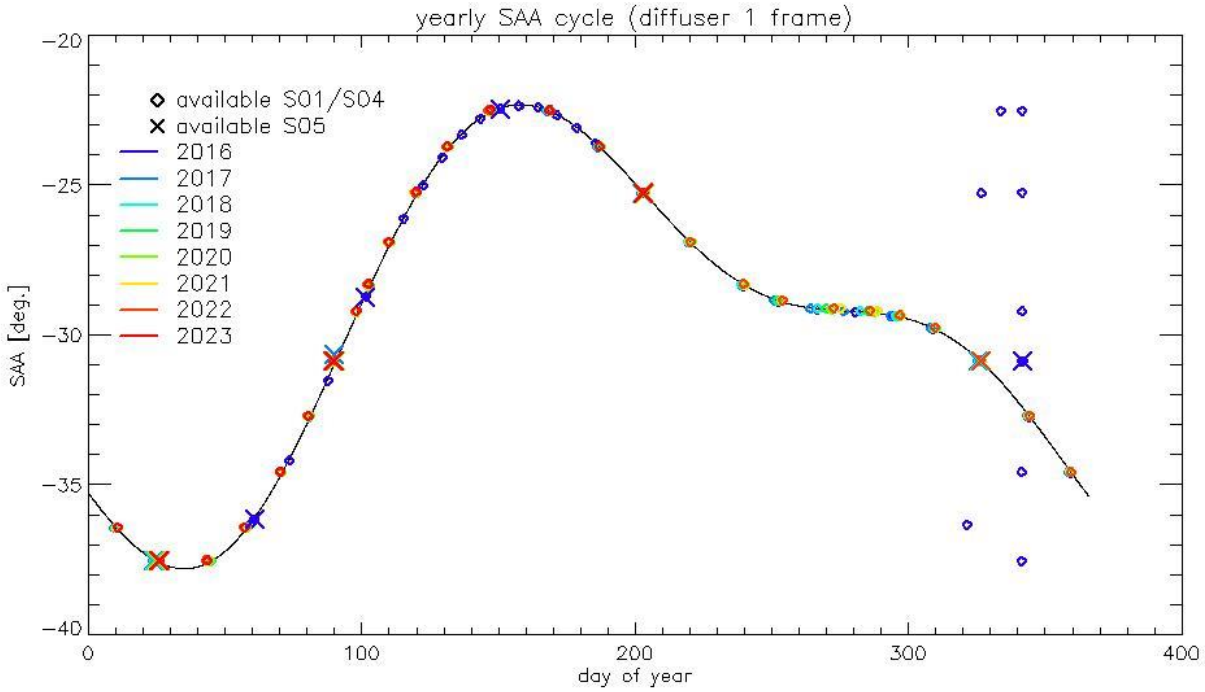

Figure 5: Sun azimuth angles during acquired OLCI-A Radiometric Calibrations (diffuser frame) on top of nominal yearly cycle (black curve). Diffuser 1 with diamonds, diffuser 2 with crosses. Different colours correspond to different years of acquisition (see the legend inside the figure).

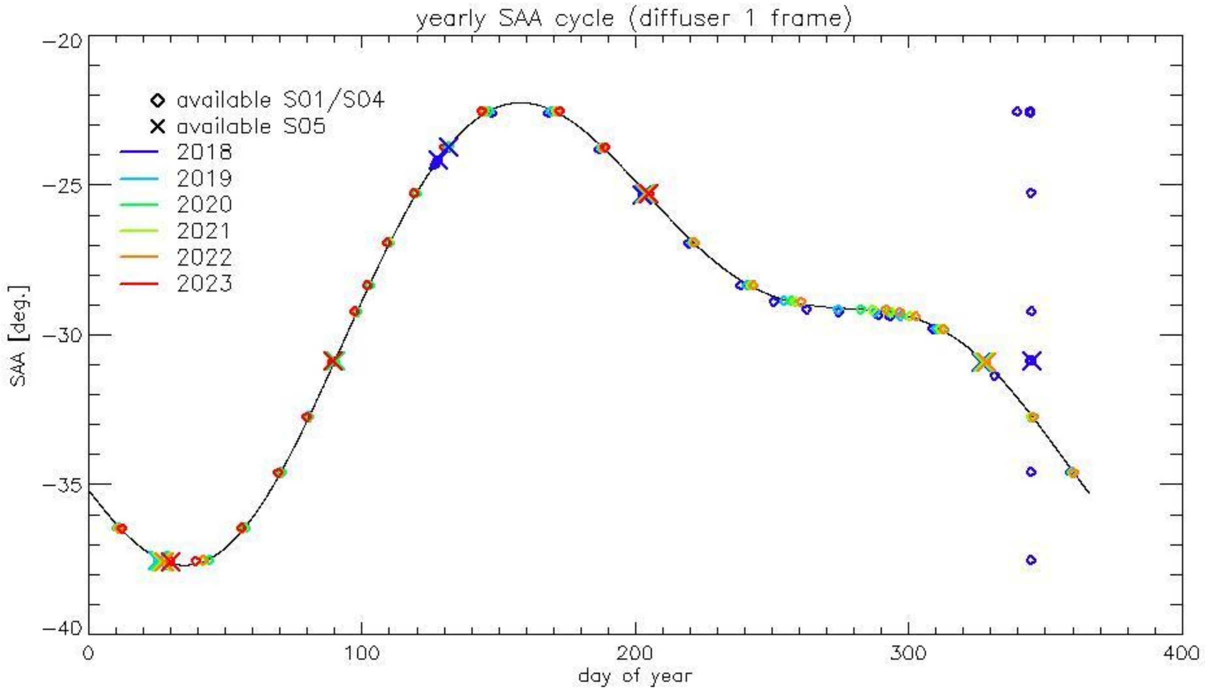

Figure 6: same as Figure 5 for OLCI-B.

Sun Zenith Angles as a function of Sun Azimuth Angles are presented in Figure 7 for OLCI-A and Figure 8 for OLCI-B.

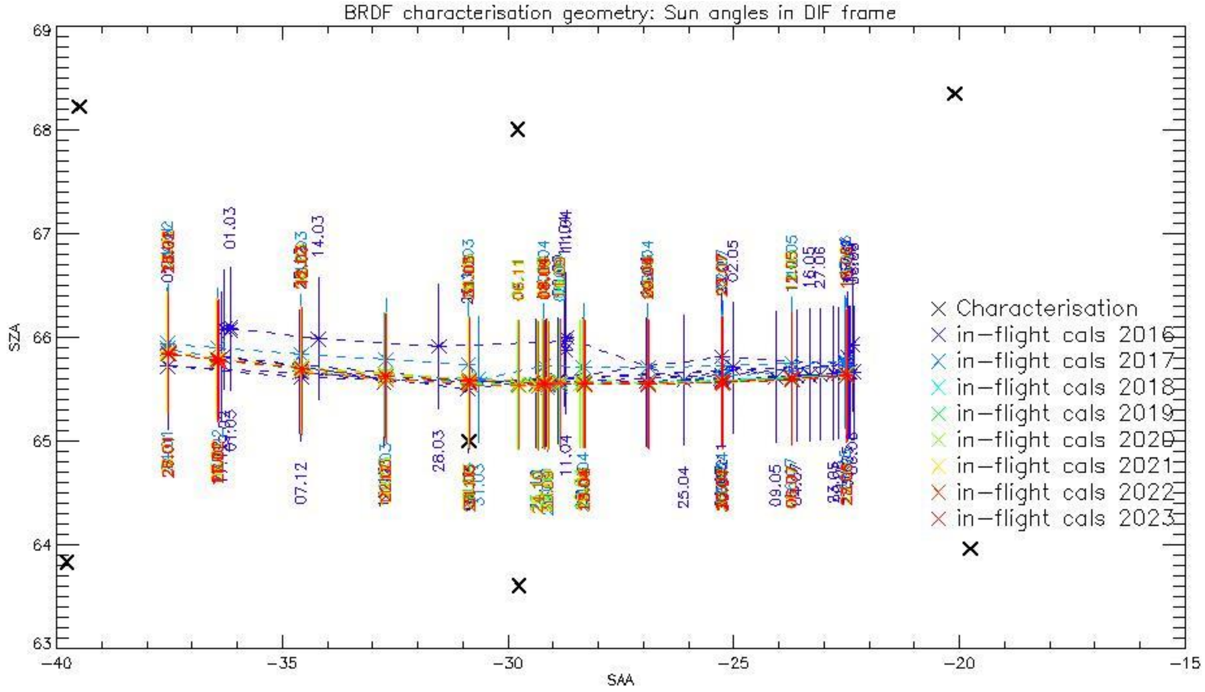

Figure 7: OLCI-A Sun geometry during radiometric Calibrations on top of characterization ones (diffuser frame)

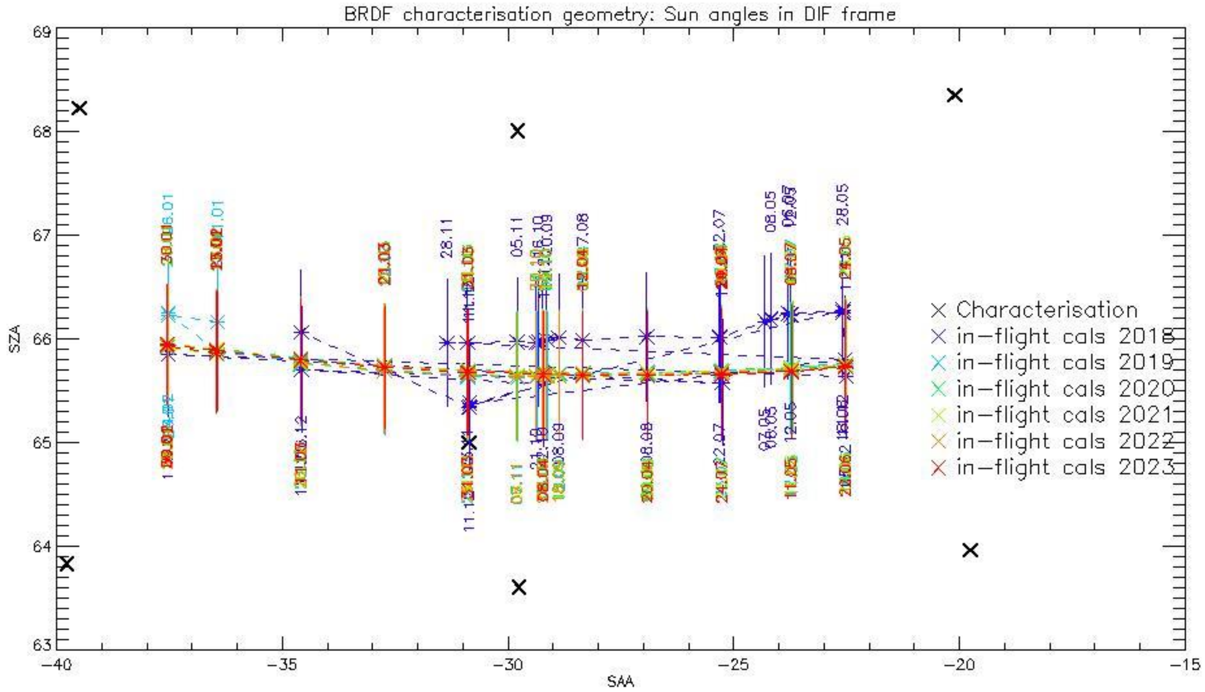

Figure 8: same as Figure 7 for OLCI-B

2.2.1 Dark Offsets [OLCI-L1B-CV-230]

Note about the High Energy Particles:

The filtering of High Energy Particle (HEP) events from radiometric calibration data has been implemented (for shutter frames only) in a post processor, allowing generating Dark Offset and Dark Current tables computed on filtered data. The post-processor starts from IPF intermediate data (corrected counts), applies the HEP detection and filtering and finally computes the Dark Offset and Dark Current tables the same way as IPF. An example of the impact of HEP filtering is given in Figure 9.

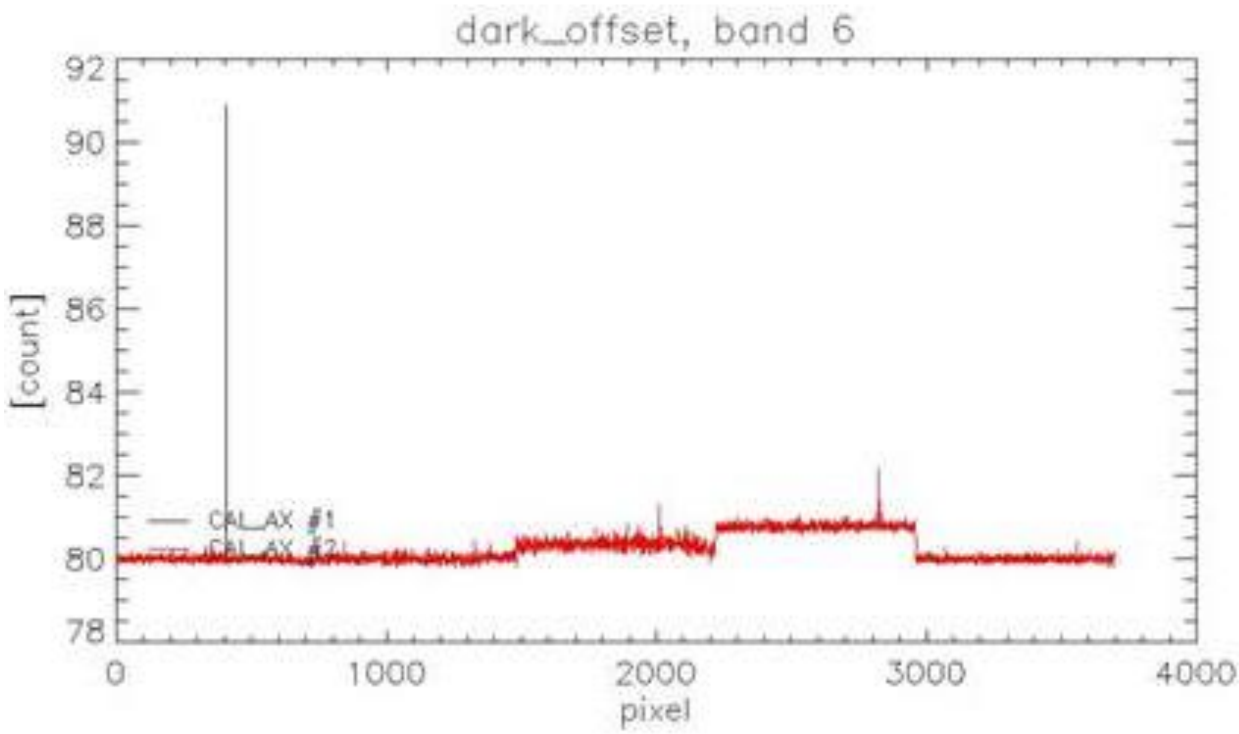

Figure 9: Dark Offset table for band Oa06 with (red) and without (black) HEP filtering (Radiometric Calibration of 22 July 2017). The strong HEP event near pixel 400 has been detected and removed by the HEP filtering.

All results presented below in this section have been obtained using the HEP filtered Dark Offset and Dark Current tables.

2.2.1.2 OLCI-A

Dark offsets

Dark offsets are continuously affected by the global offset induced by the Periodic Noise on the OCL (Offset Control Loop) convergence. Current reporting period calibrations are affected the same way as others. The amplitude of the shift varies with band and camera from virtually nothing (e.g. camera 2, band 0a1) to up to 5 counts (Oa21, camera 3). The Periodic Noise itself comes on top of the global shift with its known signature: high frequency oscillations with a rapid damp. This effect remains more or less stable with time in terms of amplitude, frequency and decay length, but its phase varies with time, introducing the global offset mentioned above.

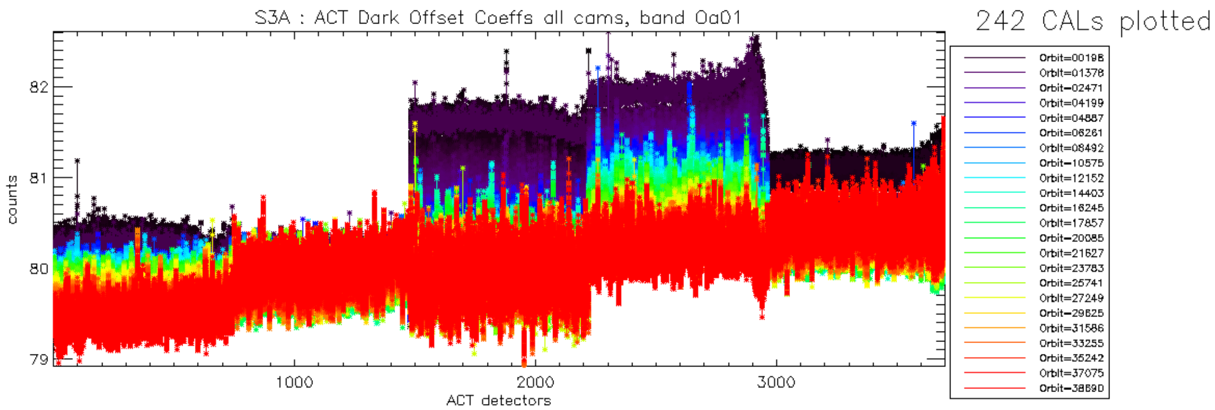

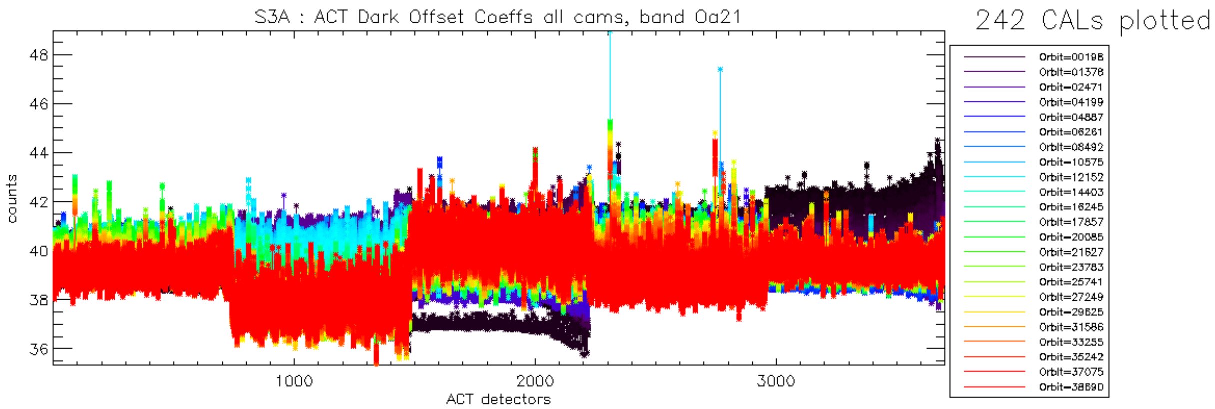

Figure 10: OLCI-A Dark Offset for band Oa1 (top) and Oa21 (bottom), all radiometric calibrations so far except the first one (orbit 183) for which the instrument was not thermally stable yet.

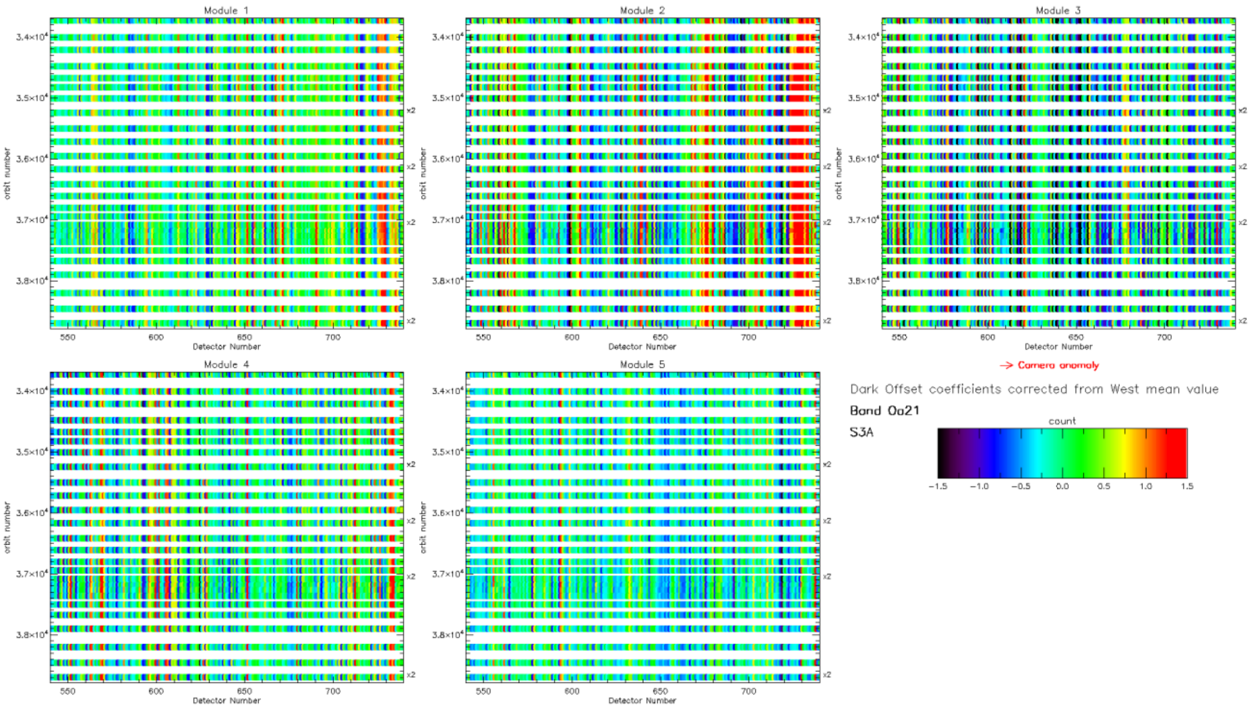

Figure 11: map of OLCI-A periodic noise for the 5 cameras, for band Oa21. X-axis is detector number (East part, from 540 to 740, where the periodic noise occurs), Y-axis is the orbit number. Y-axis range is focused on the most recent 5000 orbits. The counts have been corrected from the West detectors mean value (not affected by periodic noise) in order to remove mean level gaps and consequently to have a better visualisation of the long term evolution of the periodic noise structure. At the beginning of the mission the periodic noise for band Oa21 had strong amplitude in camera 2, 3 and 5 compared to camera 1 and 4. However PN evolved through the mission and these discrepancies between cameras have been reduced. At the time of this Cyclic Report Camera 2 still shows a slightly higher PN than other cameras.

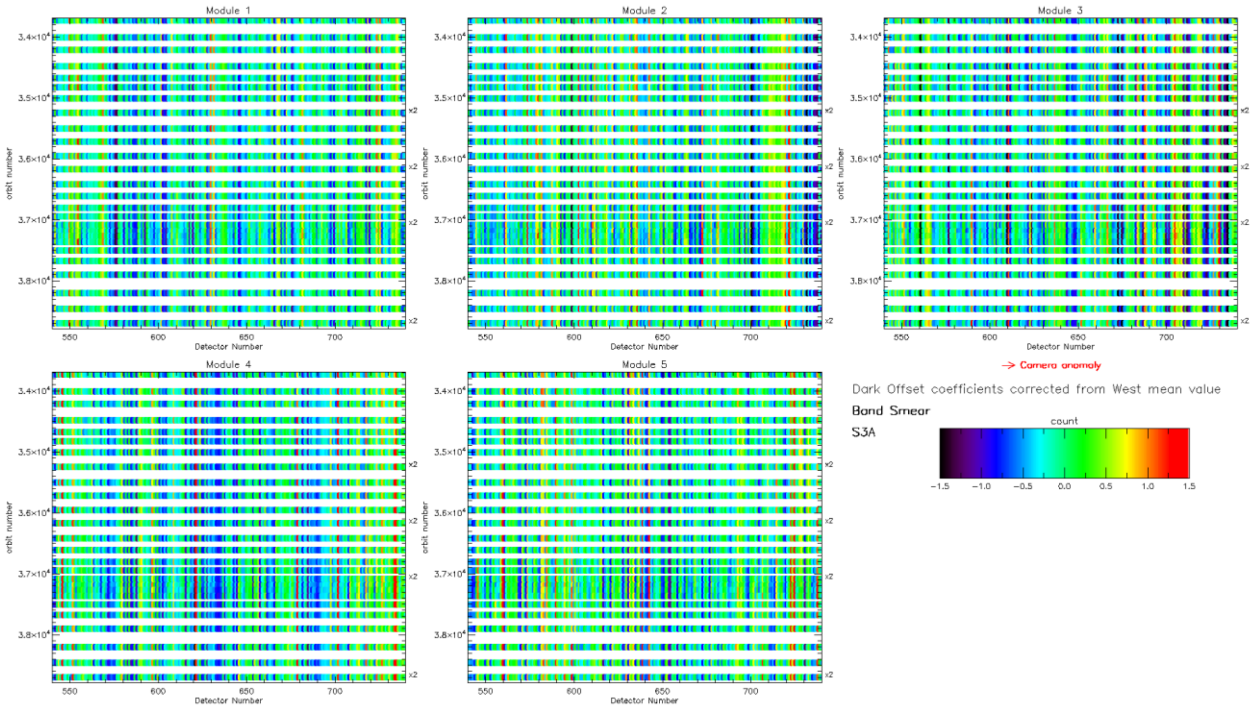

Figure 12: same as Figure 11 for smear band.

Figure 11 and Figure 12 show the so-called ‘map of periodic noise’ in the 5 cameras, for respectively band 21 and smear band. These maps have been computed from the dark offsets after removal of the mean level of the WEST detectors (not impacted by PN) in order to remove mean level gaps from one CAL to the other and consequently to highlight the shape of the PN. Maps are focused on the last 200 EAST detectors where PN occurs and on a time range covering only the last 5000 orbits in order to better visualize the CALs of the current reporting period.

Figure 11 and Figure 12 show that at this stage of the mission the PN is very stable in all cameras. There is no special behaviour noticed during the reporting period.

Dark Currents

Dark Currents (Figure 13) are not affected by the global offset of the Dark Offsets, thanks to the clamping to the average blind pixels value. However, the oscillations of Periodic Noise remain visible. There is no significant evolution of this parameter during the current reporting period except the small regular increase (almost linear), for all detectors, since the beginning of the mission (see Figure 14).

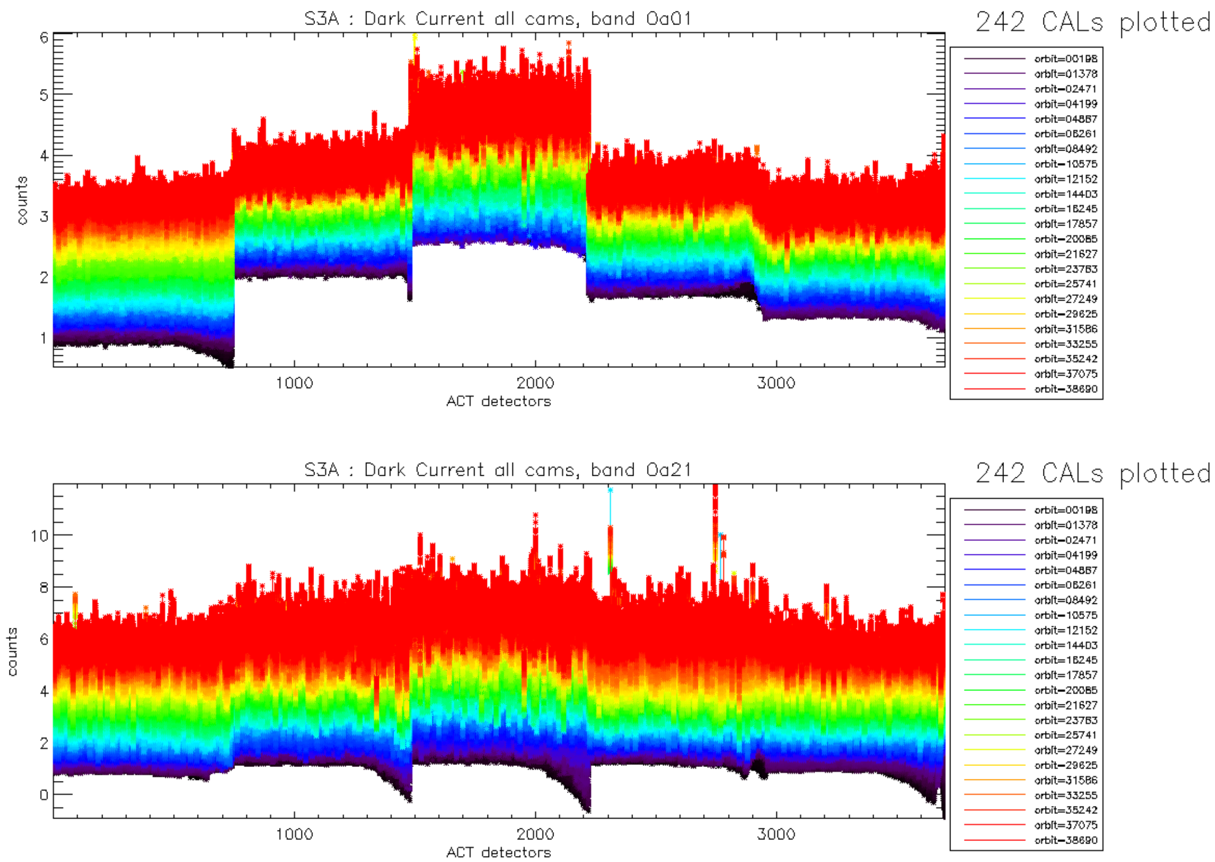

Figure 13: OLCI-A Dark Current for band Oa1 (top) and Oa21 (bottom), all radiometric calibrations so far except the first one (orbit 183) for which the instrument was not thermally stable yet.

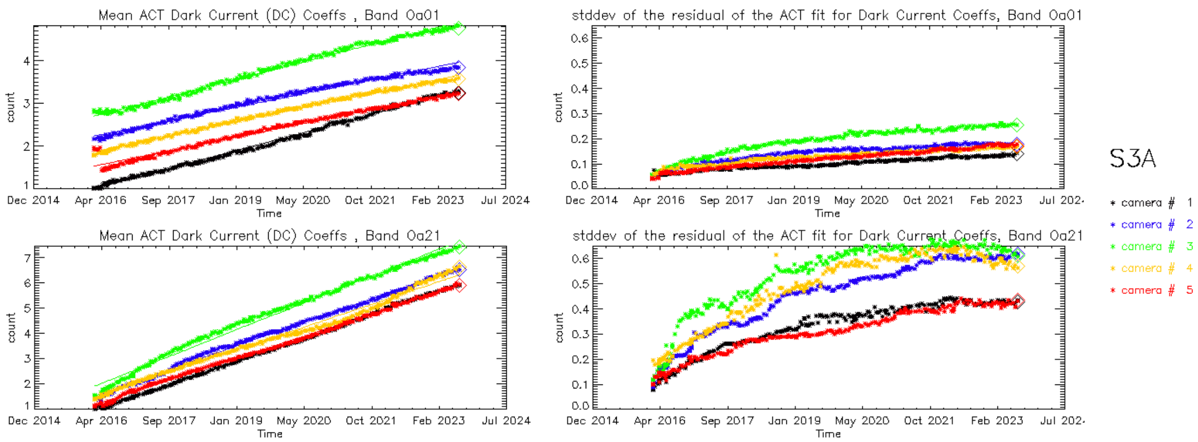

Figure 14: left column: ACT mean on 400 first detectors of OLCI-A Dark Current coefficients for spectral band Oa01 (top) and Oa21 (bottom). Right column: same as left column but for Standard deviation instead of mean. We see an increase of the DC level as a function of time especially for band Oa21.

A possible explanation of the regular increase of DC could be the increase of the number of hot pixels which is more important in Oa21 because this band is made of more CCD lines than band Oa01 and thus receives more cosmic rays impacts. It is known that cosmic rays degrade the structure of the CCD, generating more and more hot pixels at long term scales. Indeed, when computing the time slopes of the spatially averaged Dark Current as a function of band, i.e. the slopes of curves in left plots of Figure 14, one can see that Oa21 is by far the most affected, followed by the smear band (Figure 15, left); when plotting these slopes against total band width (in CCD rows, regardless of the number of micro-bands), the correlation between the slope values and the width becomes clear (Figure 15, right).

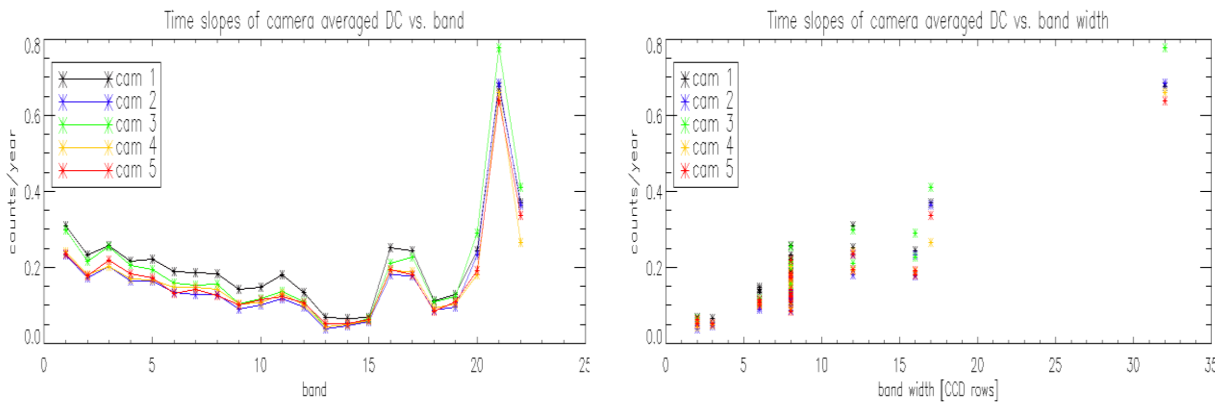

Figure 15: OLCI-A Dark current increase rates with time (in counts per year) vs. band (left) and vs. band width (right)

2.2.1.3 OLCI-B

<u>Dark Offsets</u>

Dark offsets for OLCI-B show a similar behaviour than for OLCI-A: mean level gaps between different orbits, induced by the presence of a pseudo periodic noise on the east edge of the cameras with a drifting phase.

Evolution of OLCI-B Dark Offset coefficients for band Oa01 and Oa21 are represented in Figure 16.

The periodic noise maps are shown for band Oa21 and smear band respectively in Figure 17 and Figure 18. As it happened for OLCI-A after a few thousands of orbits, the strong periodic noise phase and amplitude drift, present at the very beginning of the mission is now showing a clear stabilization.

Despite this overall stabilization, small evolutions are still noticeable in some bands/camera, like for example camera 1 in band Oa21 (upper left map in Figure 17) or in camera 1 band smear (upper left map in Figure 18).

Globally, OLCI-B PN is slightly less stabilized than OLCI-A PN.

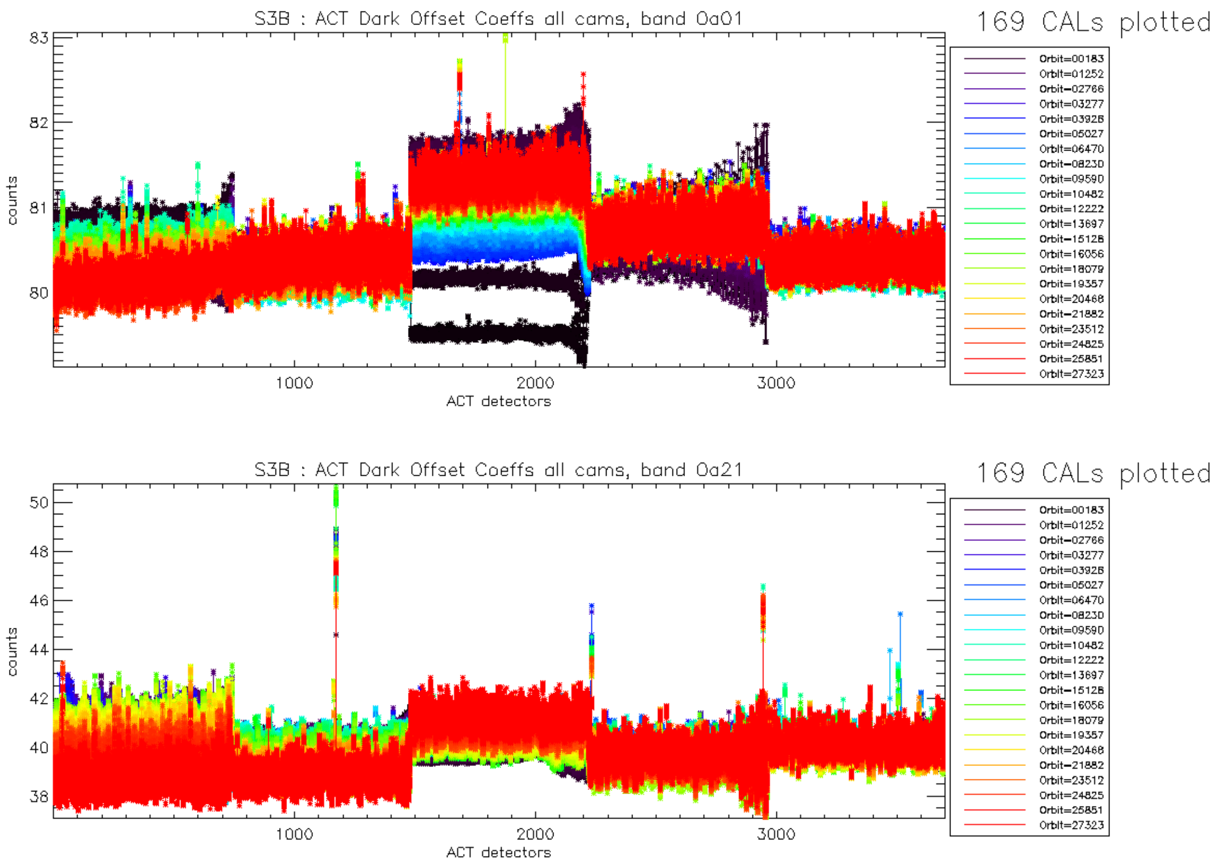

Figure 16: OLCI-B Dark Offset for band Oa1 (top) and Oa21 (bottom), all radiometric calibrations so far except the first one (orbit 167) for which the instrument was not thermally stable yet.

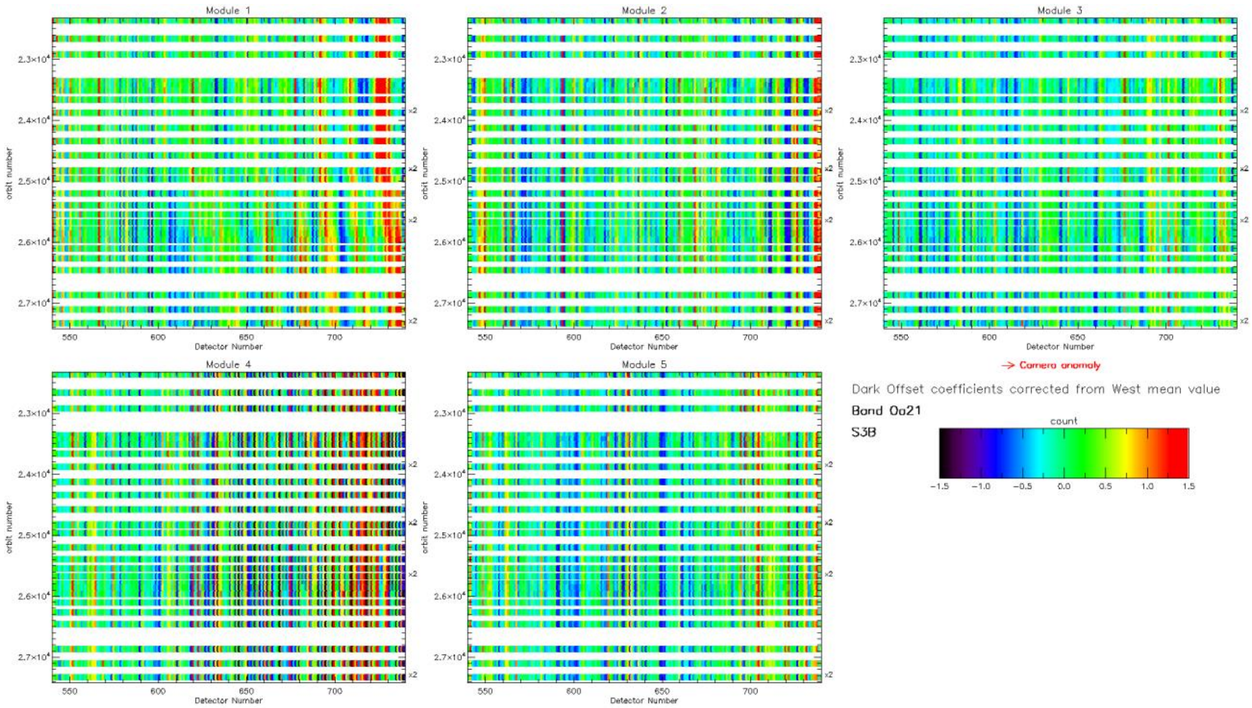

Figure 17: OLCI-B map of periodic noise for the 5 cameras, for band Oa21. X-axis is detector number (East part, from 540 to 740, where the periodic noise occurs), Y-axis is the orbit number. The counts have been corrected from the West detectors mean value (not affected by periodic noise) in order to remove mean level gaps and consequently to have a better visualization of the long term evolution of the periodic noise structure.

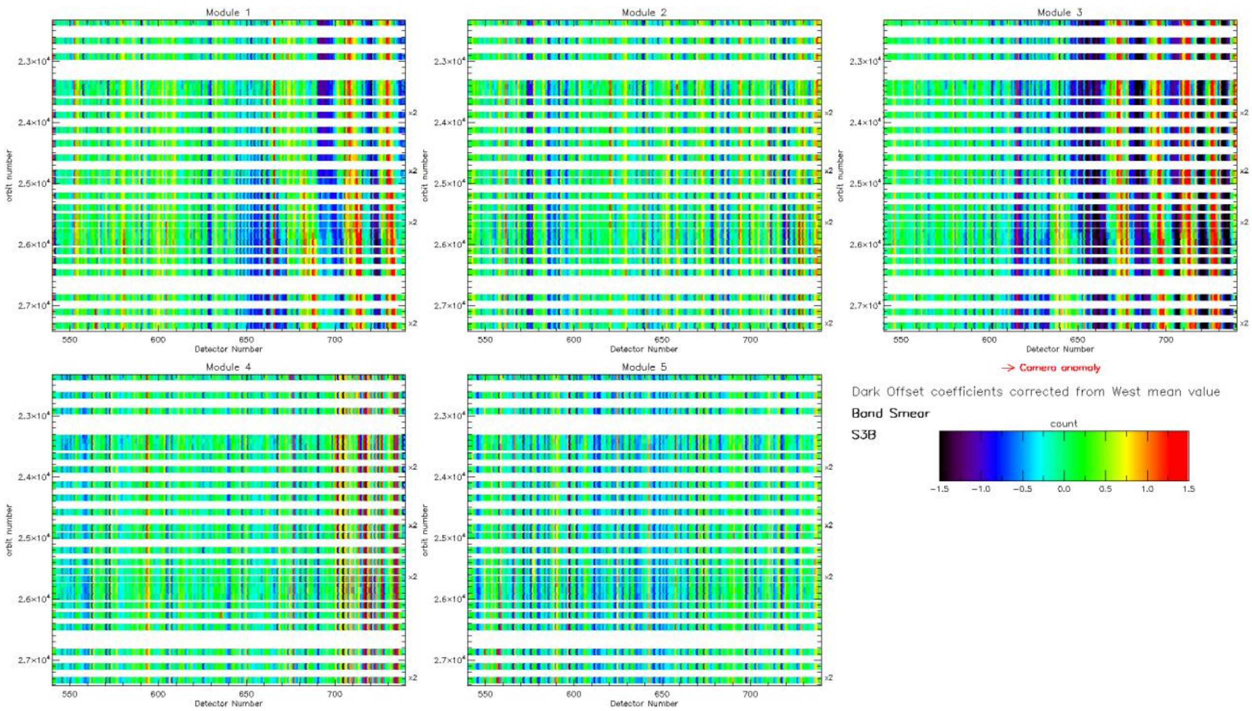

Figure 18: same as Figure 17 for smear band.

Dark Currents

As for OLCI-A there is no significant evolution of the Dark Current coefficients (Figure 19) during the current reporting period except the small regular increase (almost linear), for all detectors, since the beginning of the mission (see Figure 20) probably due to an increase of hot pixels (see Figure 21).

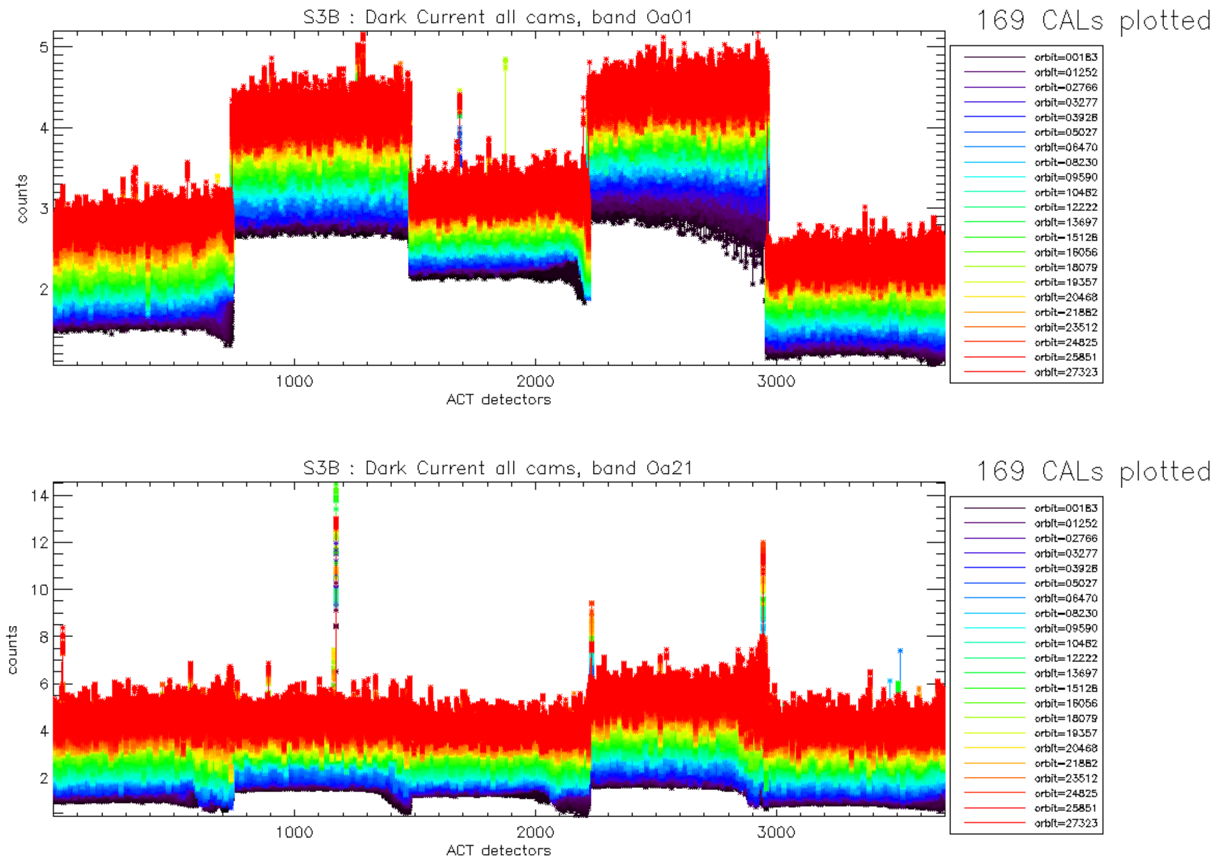

Figure 19: OLCI-B Dark Current for band Oa1 (top) and Oa21 (bottom), all radiometric calibrations so far except the first one (orbit 167) for which the instrument was not thermally stable yet.

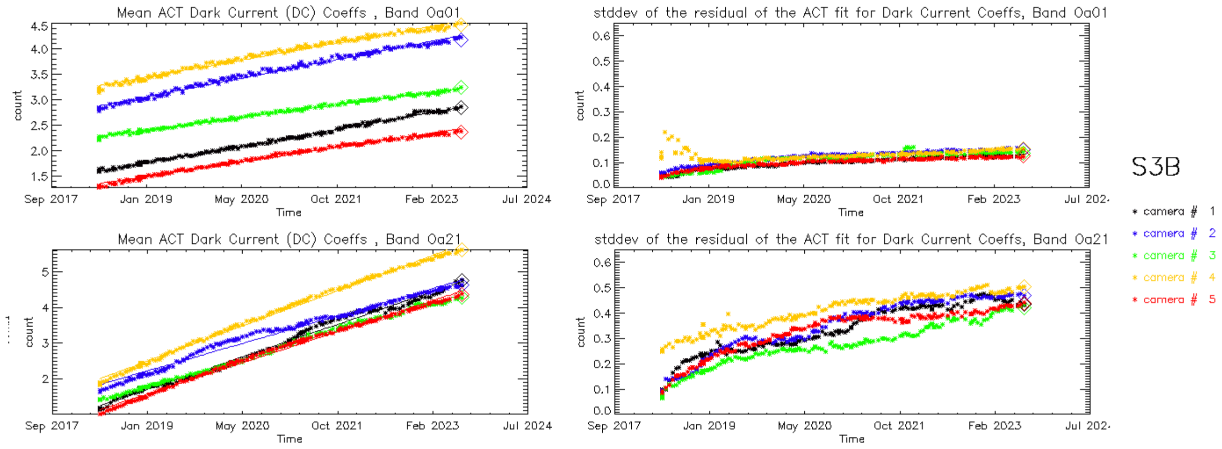

Figure 20: left column: ACT mean on 400 first detectors of OLCI-B Dark Current coefficients for spectral band Oa01 (top) and Oa21 (bottom). Right column: same as left column but for Standard deviation instead of mean. We see an increase of the DC level as a function of time especially for band Oa21.

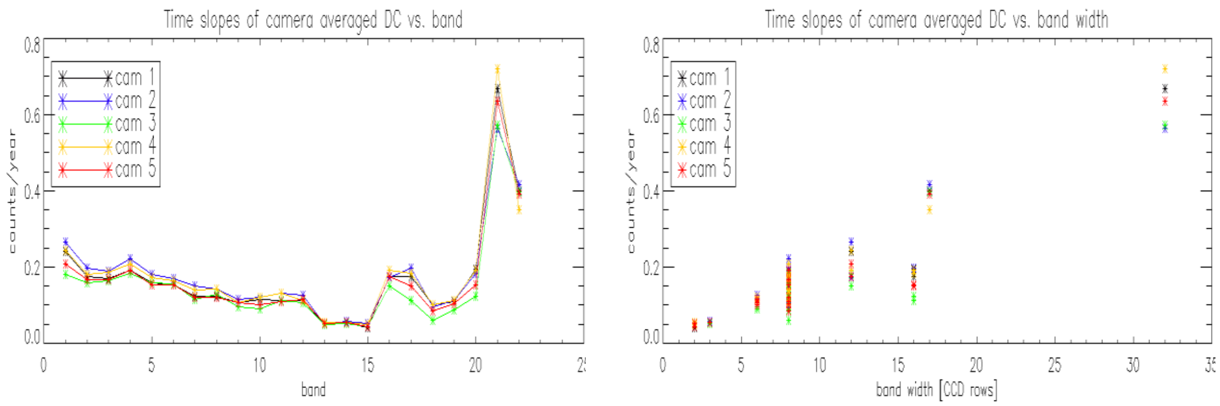

Figure 21: OLCI-B Dark Current increase rates with time (in counts per year) vs. band (left) and vs. band width (right)

2.2.3 Instrument response and degradation modelling [OLCI-L1B-CV-250]

2.2.3.1 Instrument response monitoring

2.2.3.1.1 OLCI-A

Figure 22 shows the gain coefficients of every pixel for two OLCI-A channels, Oa1 (400 nm) and Oa21 (1020 nm), highlighting the significant evolution of the instrument response since early mission.

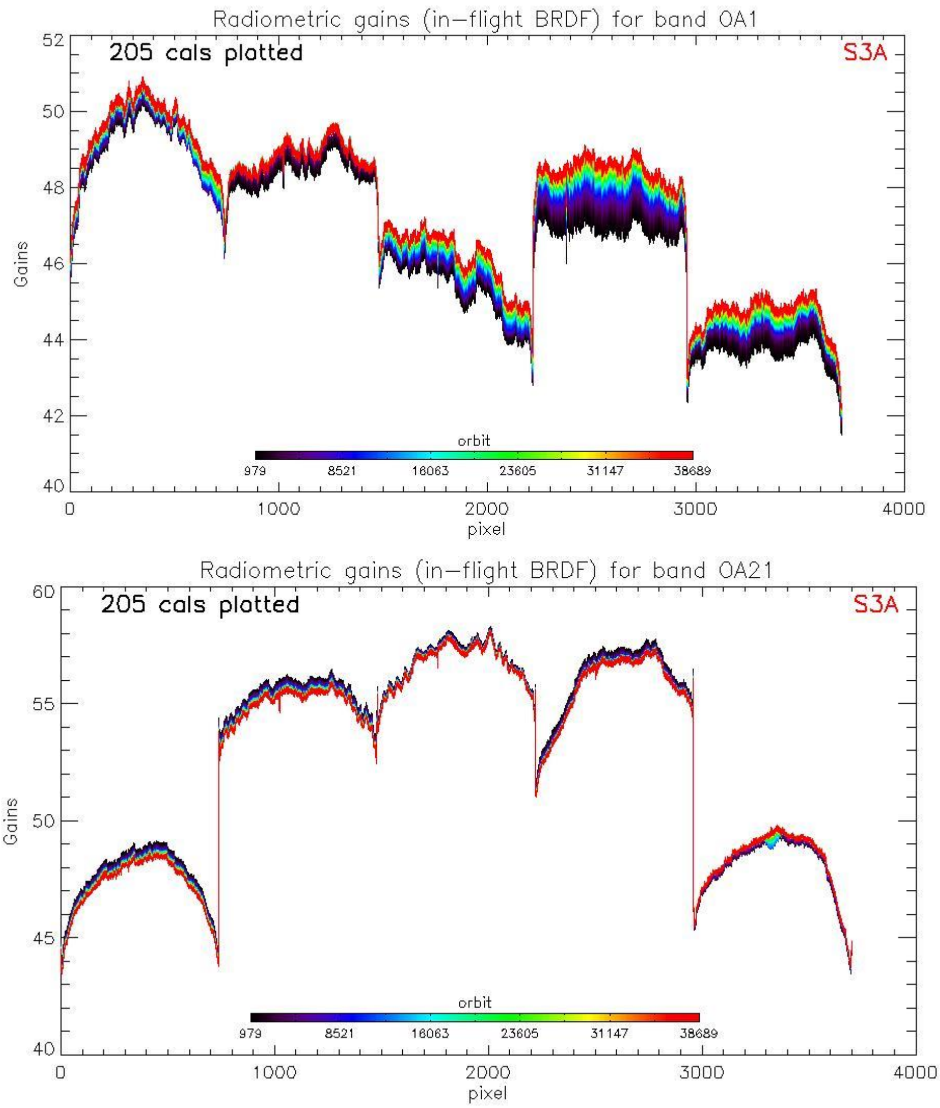

Figure 22: OLCI-A Gain Coefficients for band Oa1 (top) and Oa21 (bottom), derived using the in-flight BRDF model. The dataset is made of all diffuser 1 radiometric calibrations since orbit 979.

Figure 23 displays a summary of the time evolution of the cross-track average of the gains (in-flight BRDF, taking into account the diffuser ageing), for each module, relative to a given reference calibration (the 25/04/2016, change of OLCI channel settings). It shows that, if a significant evolution occurred during the early mission, the trends tend in general to stabilize, with some exceptions (e.g. band 1 of camera 1 and 4, bands 2 & 3 of camera 5).

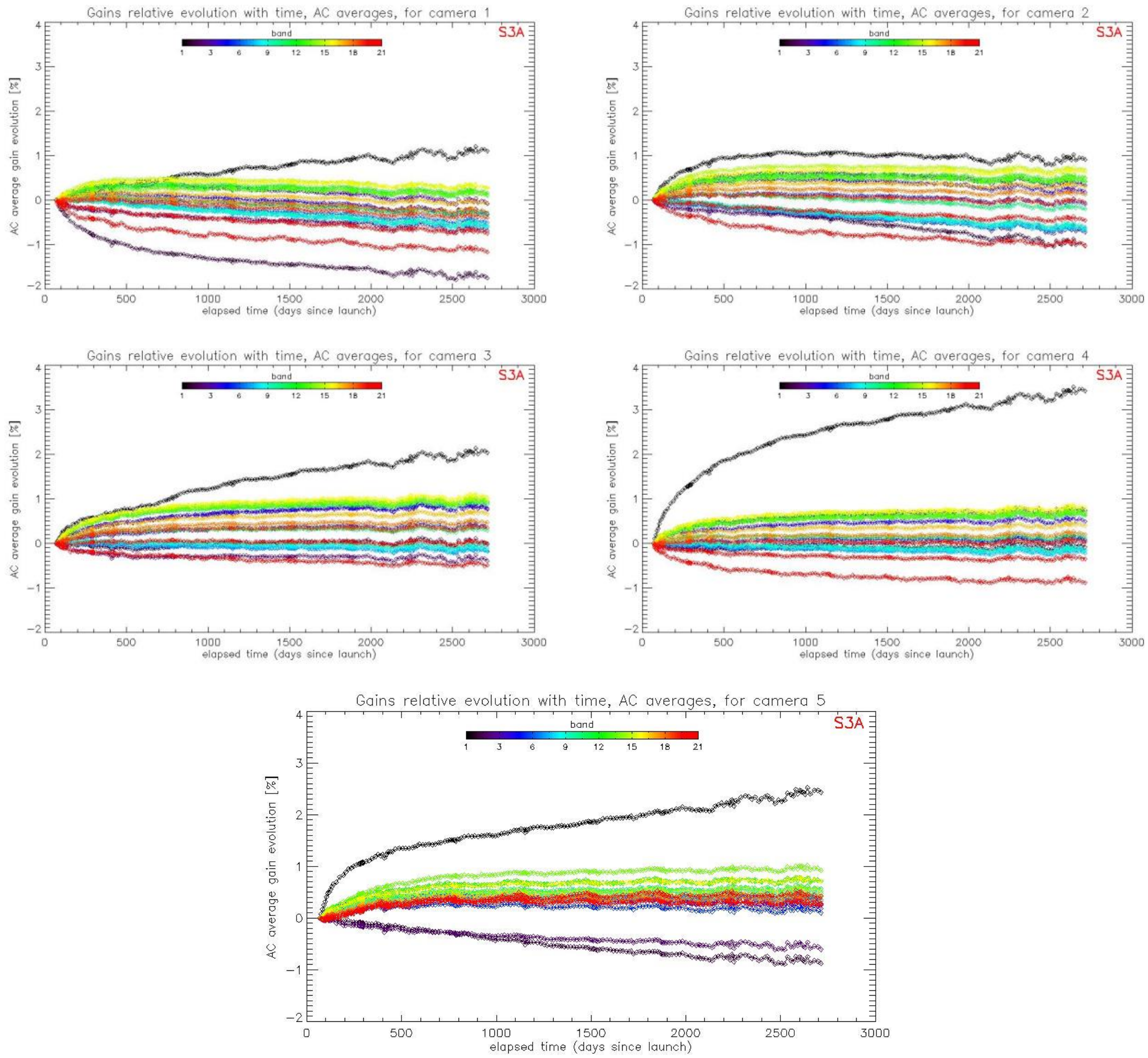

Figure 23: camera averaged gain relative evolution with respect to calibration of 25/04/2016 (change of OLCI channel settings), as a function of elapsed time since the beginning of the mission; one curve for each band (see colour code on plots), one plot for each module. The diffuser ageing is taken into account.

2.2.3.1.2 OLCI-B

Figure 24 shows the gain coefficients of every pixel for two OLCI-B channels, Oa1 (400 nm) and Oa21 (1020 nm), highlighting the significant evolution of the instrument response since early mission.

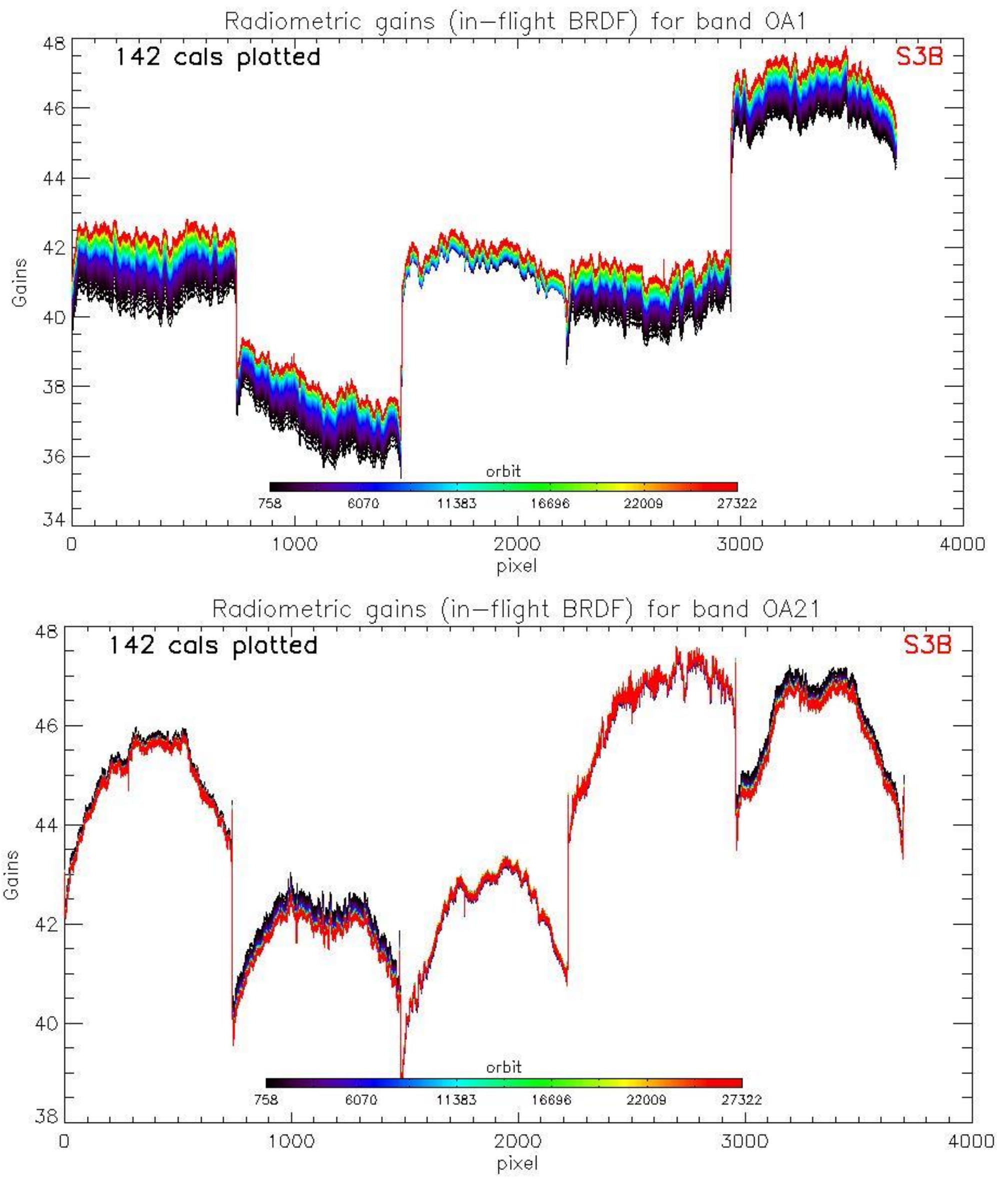

Figure 24: OLCI-B Gain Coefficients for band Oa1 (top) and Oa21 (bottom), derived using the in-flight BRDF model. The dataset is made of all diffuser 1 radiometric calibrations since orbit 758.

Figure 25 displays a summary of the time evolution of the cross-track average of the gains (in-flight BRDF, taking into account diffuser ageing), for each module, relative to a given reference calibration (first calibration after channel programming change: 18/06/2018). It shows that, if a significant evolution occurred during the early mission, the trends tend to stabilize. The large amount of points near elapsed time = 220 days is due to the yaw manoeuvre campaign. The slight discontinuity near "day 920 since launch" is due to the upgrade of the Ageing model.

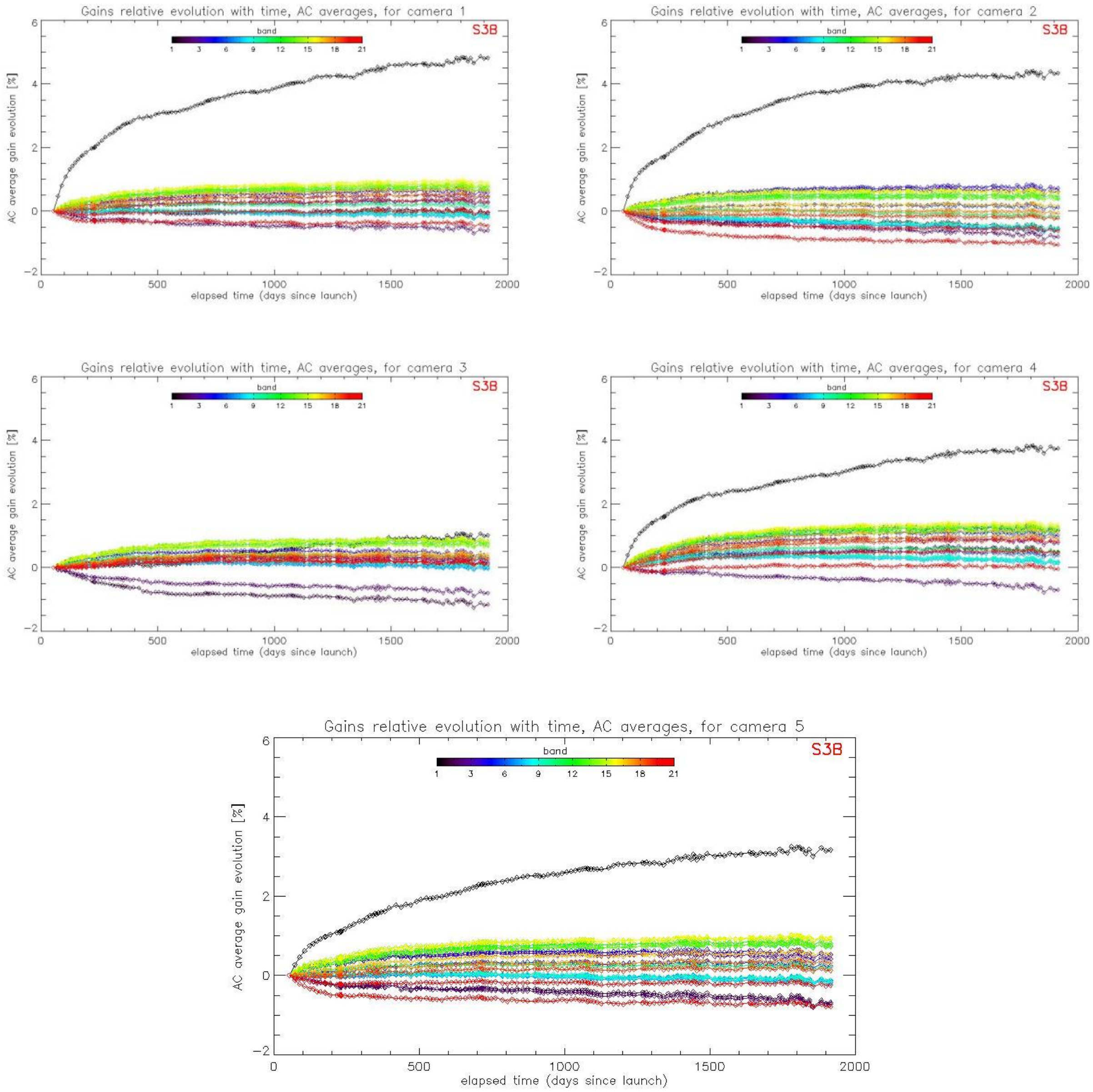

Figure 25: OLCI-B camera averaged gain relative evolution with respect to first calibration after channel programming change (18/06/2018), as a function of elapsed time since the beginning of the mission; one curve for each band (see colour code on plots), one plot for each module. The diffuser ageing is taken into account.

2.2.3.2 Instrument evolution modelling

2.2.3.2.1 OLCI-A

A new OLCI-A Radiometric Gain Model has been put in operations at PDGS the 18/07/2023 (Processing Baseline 3.23). This model has been derived on the basis of an extended (compared to the previous model) Radiometric Calibration dataset, going from 11/04/2016 to 28/05/2023. It includes the correction of the diffuser ageing for the six bluest bands (Oa1 to Oa6) for which it is clearly measurable. The model performance over the complete dataset (including the 3 calibrations in extrapolation over about 2 months) remains better than about 0.13% for all bands. The previous model, trained on a Radiometric Dataset limited to 30/04/2022, shows a clear drift of the model with respect to most recent data (Figure 27), that motivated the change. Comparison of the two figures shows the improvement brought by the updated model over almost all the mission. Performance shown on Figure 26 adopts, as for OLCI-B, the multiple model approach, i.e. different models (two for OLCI-A since this new PB, three for OLCI-B since PB 1.57) are used to cover the whole mission (red dashed line on Figure 26), each model being fitted on a partial dataset (green dashed line on Figure 26) whose coverage is optimized to provide best performance.

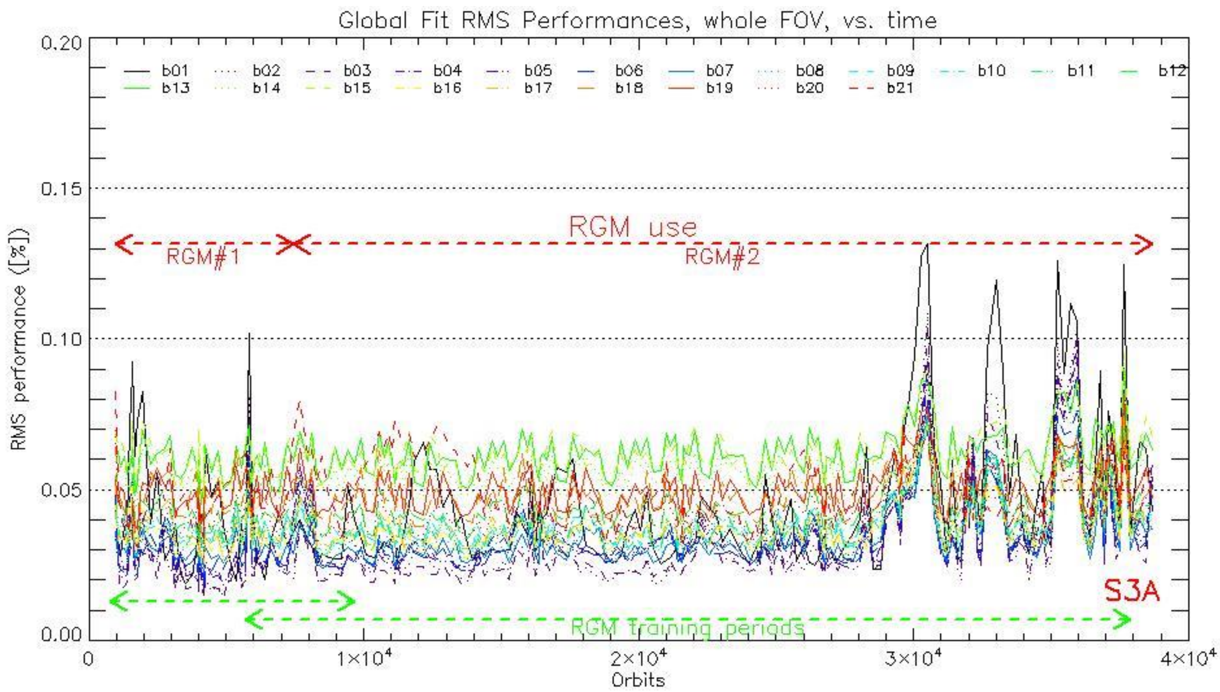

Figure 26: RMS performance of the OLCI-A Gain Model of the current processing baseline as a function of orbit.

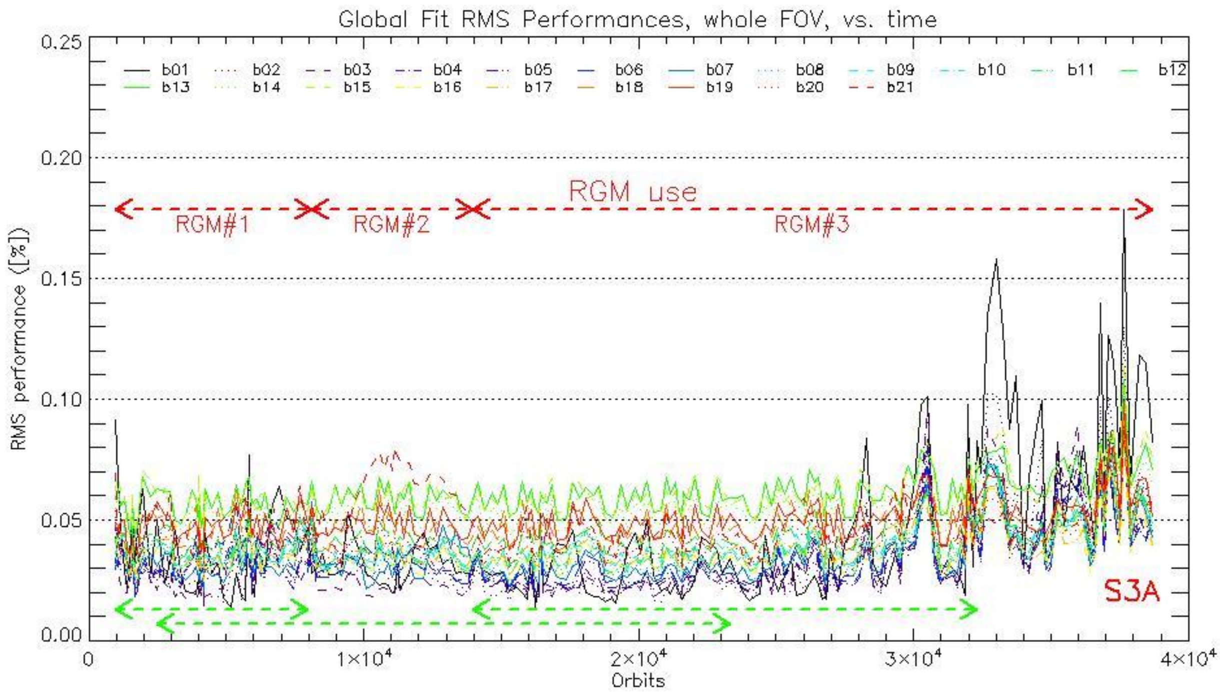

Figure 27: RMS performance of the OLCI-A Gain Model of the previous Processing Baseline as a function of orbit.

The overall instrument evolution since channel programming change (25/04/2016) is shown on Figure 28.

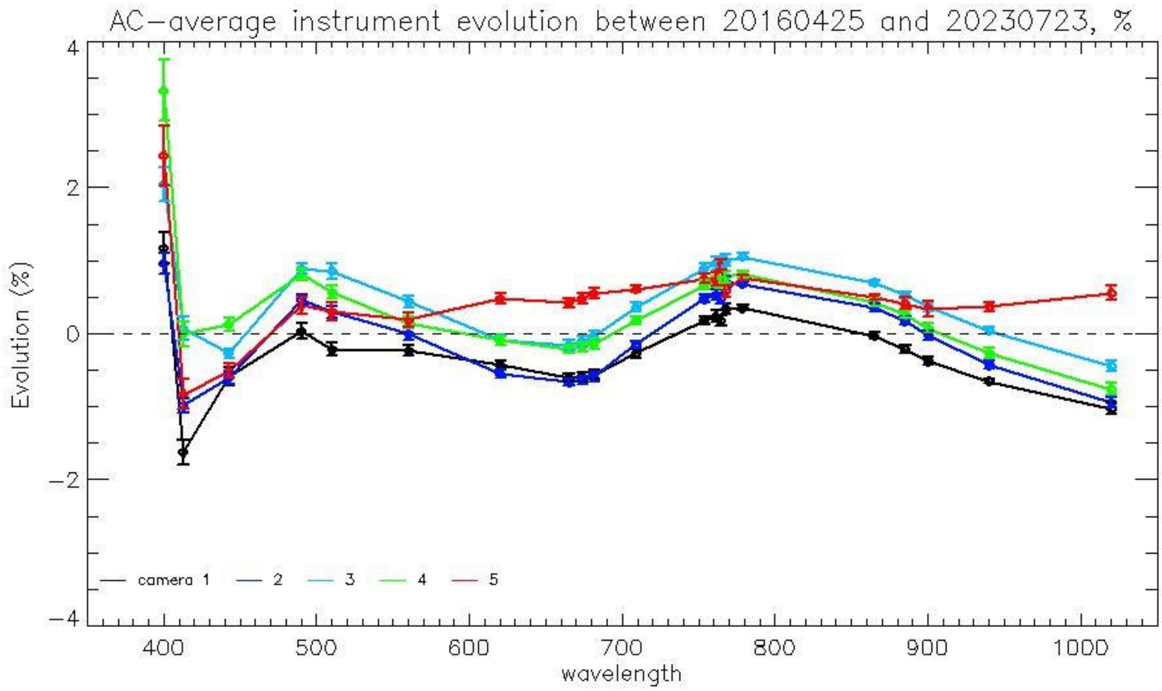

Figure 28: OLCI-A Camera-averaged instrument evolution since channel programming change (25/04/2016) and up to the most recent calibration (23/07/2023) versus wavelength.

The overall per camera performance, as a function of wavelength, and at each orbit is shown on Figure 29 as the average and standard deviation of the model over data ratio.

Finally, Figure 30 to Figure 32 show the detail of the model performance, with across-track plots of the model over data ratios at each orbit, one plot for each channel.

Comparisons of Figure 30 to Figure 32 with their counterparts in DQR of July 2022 clearly demonstrate the improvement brought by the new model whatever the level of detail.

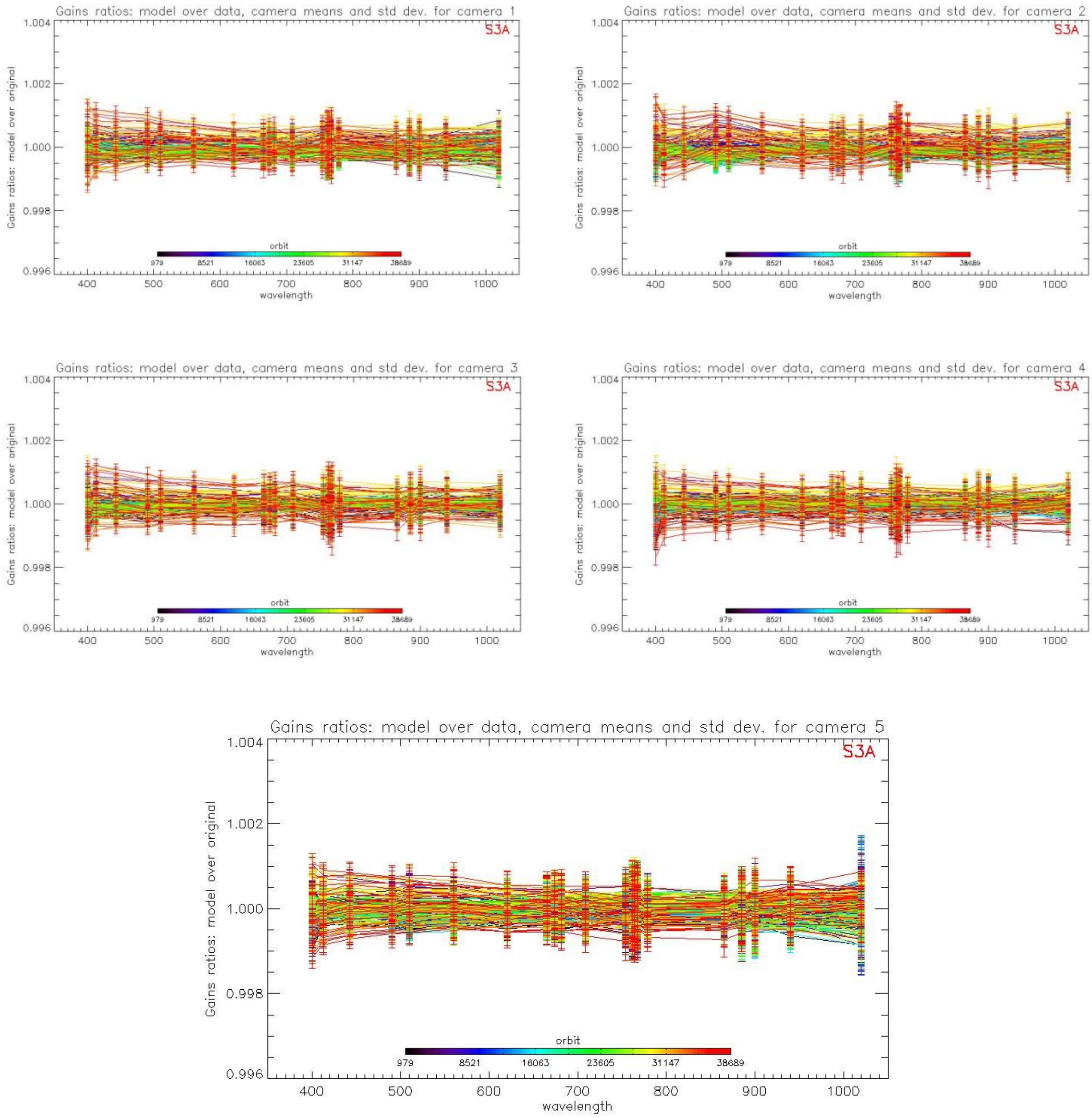

Figure 29: For the 5 cameras: OLCI-A Evolution model performance, as camera-average and standard deviation of ratio of Model over Data vs. wavelength, for each orbit of the test dataset, including 3 calibrations in extrapolation, with a colour code for each calibration from blue (oldest) to red (most recent).

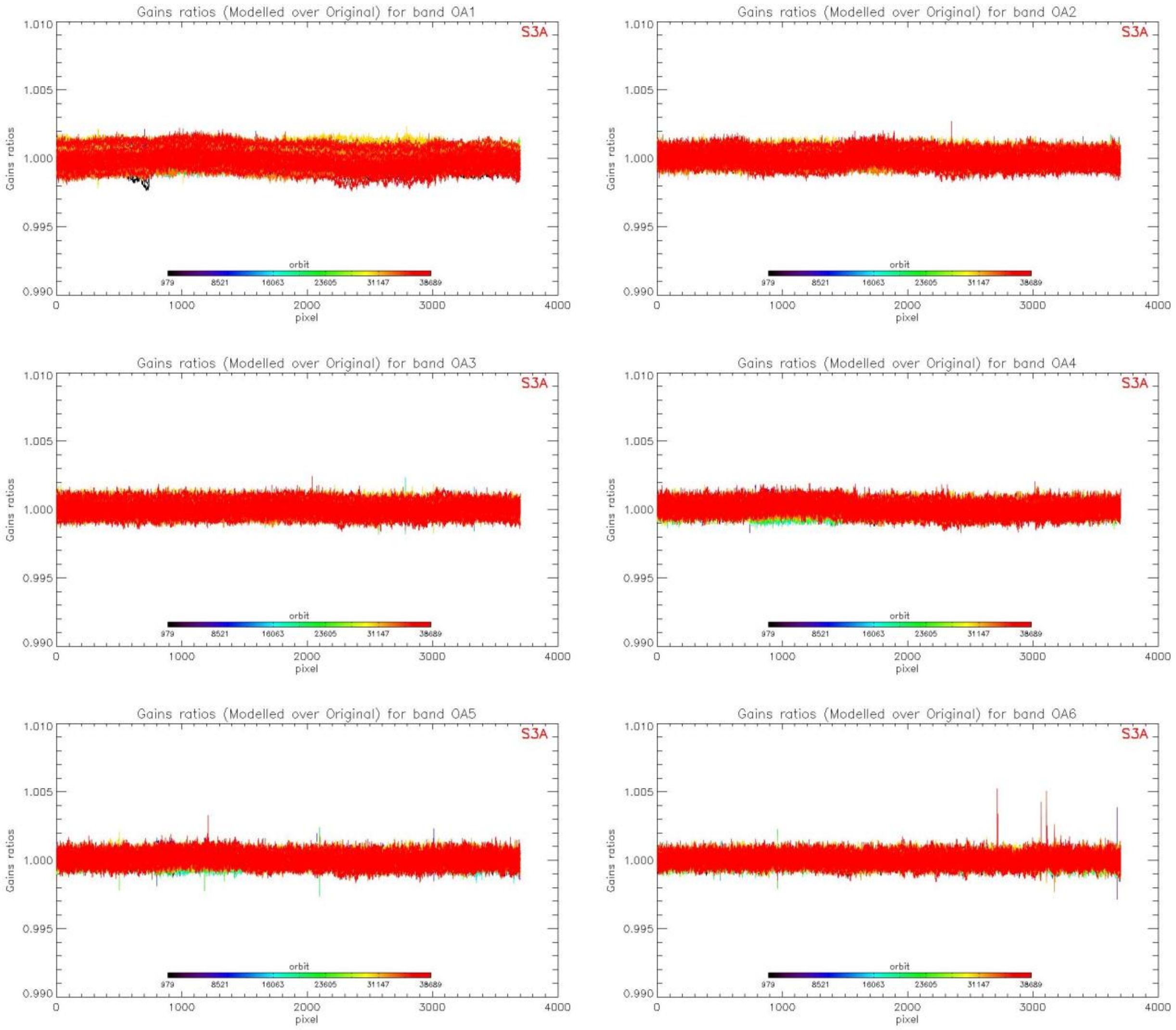

Figure 30: OLCI-A evolution model performance, as ratio of Model over Data vs. pixels, all cameras side by side, over the whole current calibration dataset (since instrument programming update), including 3 calibrations in extrapolation, channels Oa1 to Oa6.

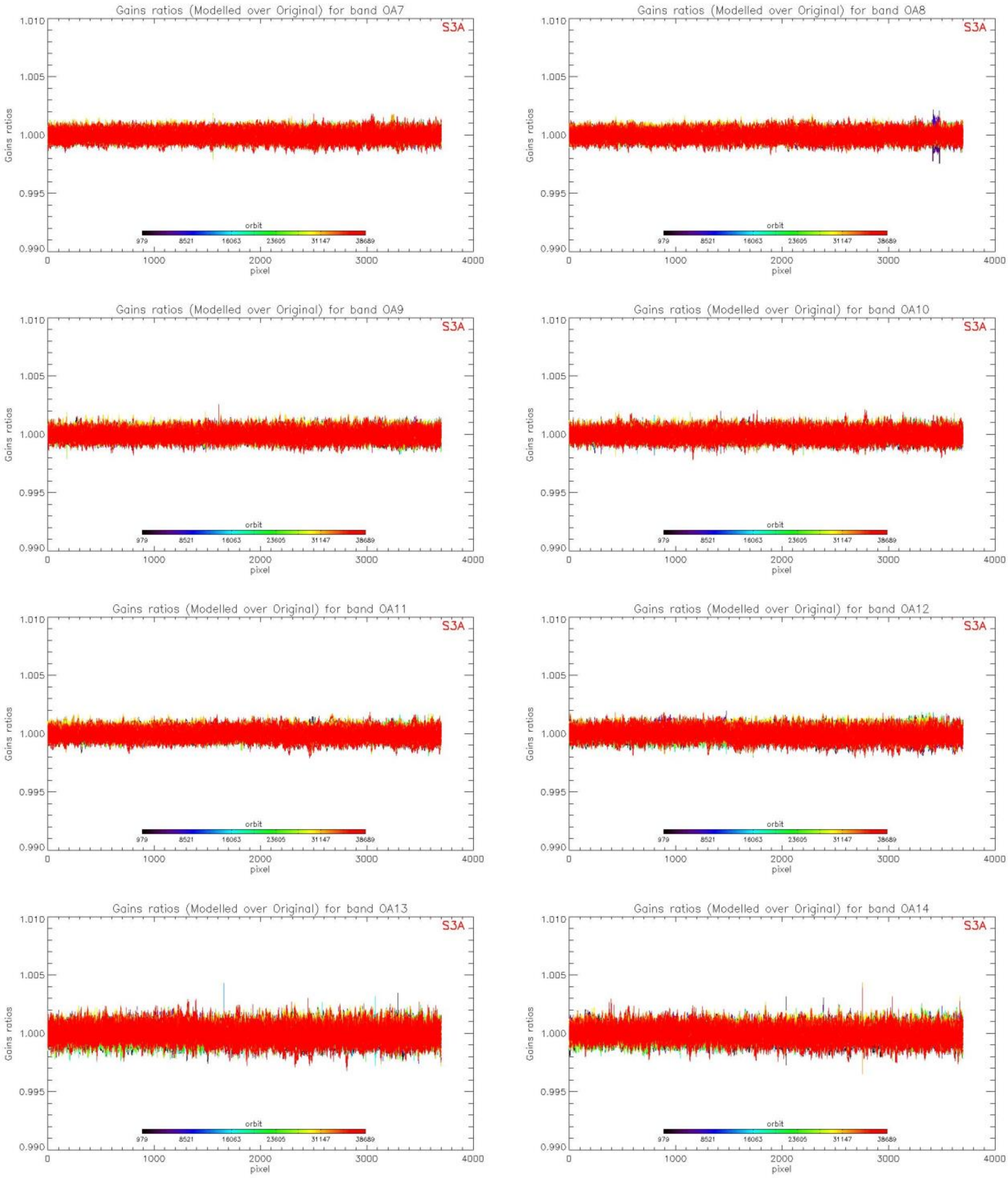

Figure 31: same as Figure 30 for channels Oa7 to Oa14.

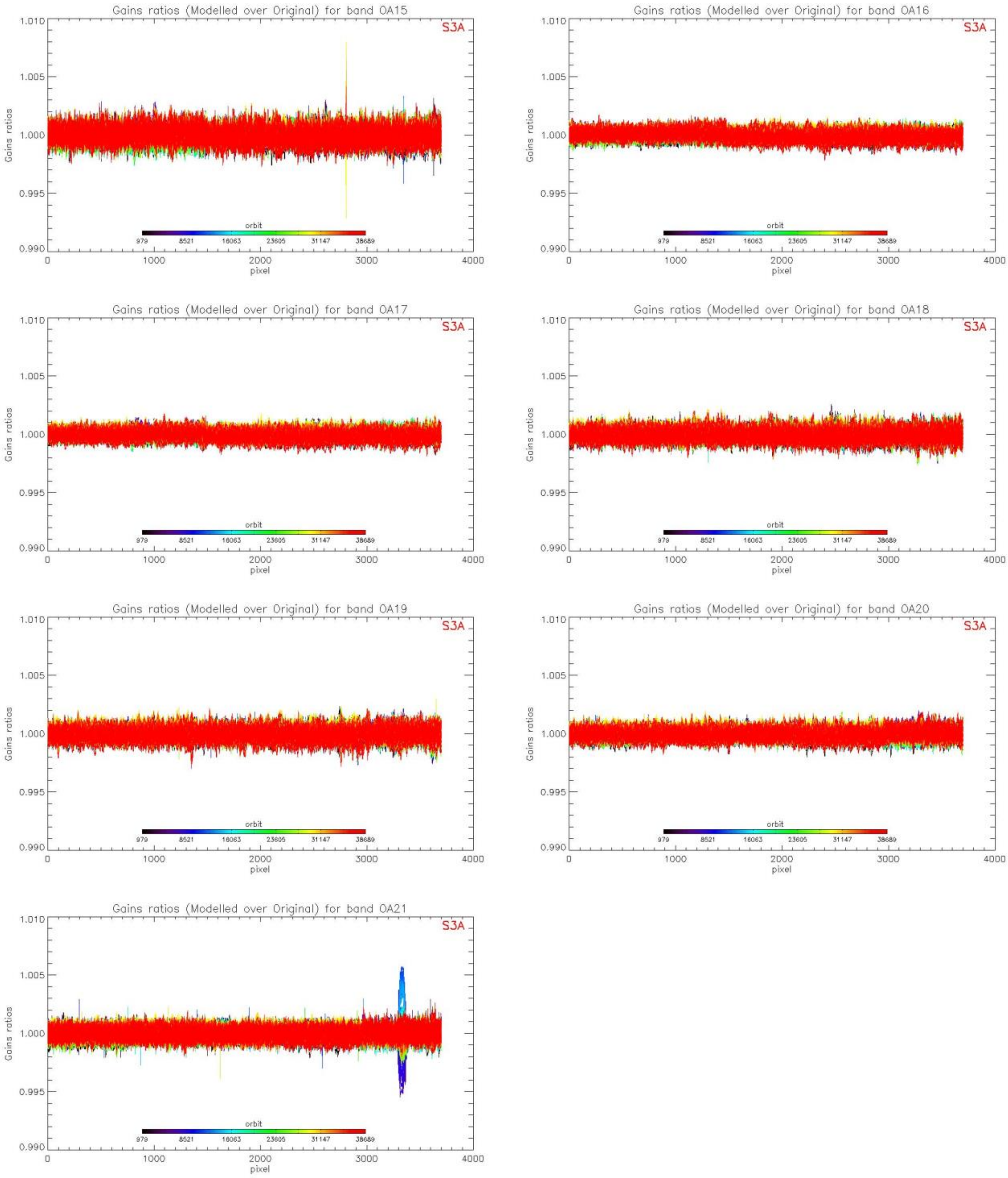

Figure 32: same as Figure 30 for channels Oa15 to Oa21.

2.2.3.2.2 OLCI-B

A new OLCI-B Radiometric Gain Model has been put in operations at PDGS on 25/07/2023 (Processing Baseline 3.23). This model has been derived on the basis of an extended Radiometric Calibration dataset (from 08/05/2018 to 24/05/2023). It includes the correction of the diffuser ageing for the five bluest bands (Oa1 to Oa5) for which it is clearly measurable. The model performance over the complete dataset (including 3 calibrations in extrapolation over about 2 months) is illustrated in Figure 33. It remains better than about 0.11% when averaged over the whole field of view for all bands at the exception of a spike near orbit 26500 reaching about up to 0.20 % for Oa02. The previous model, trained on a Radiometric Dataset limited to 29/04/2022, shows a significant drift of the model with respect to most recent data(Figure 34). Comparison of the two figures shows the improvement brought by the updated Model over all the mission.

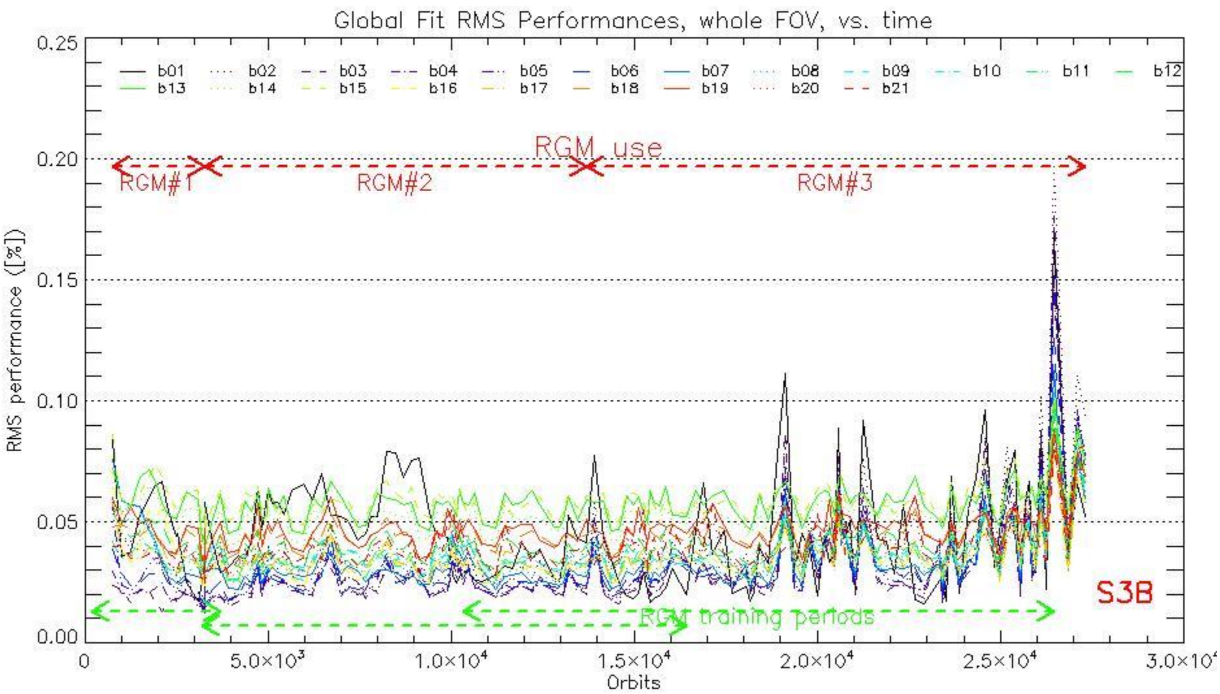

Figure 33: RMS performance of the OLCI-B Gain Model of the current processing baseline as a function of orbit.

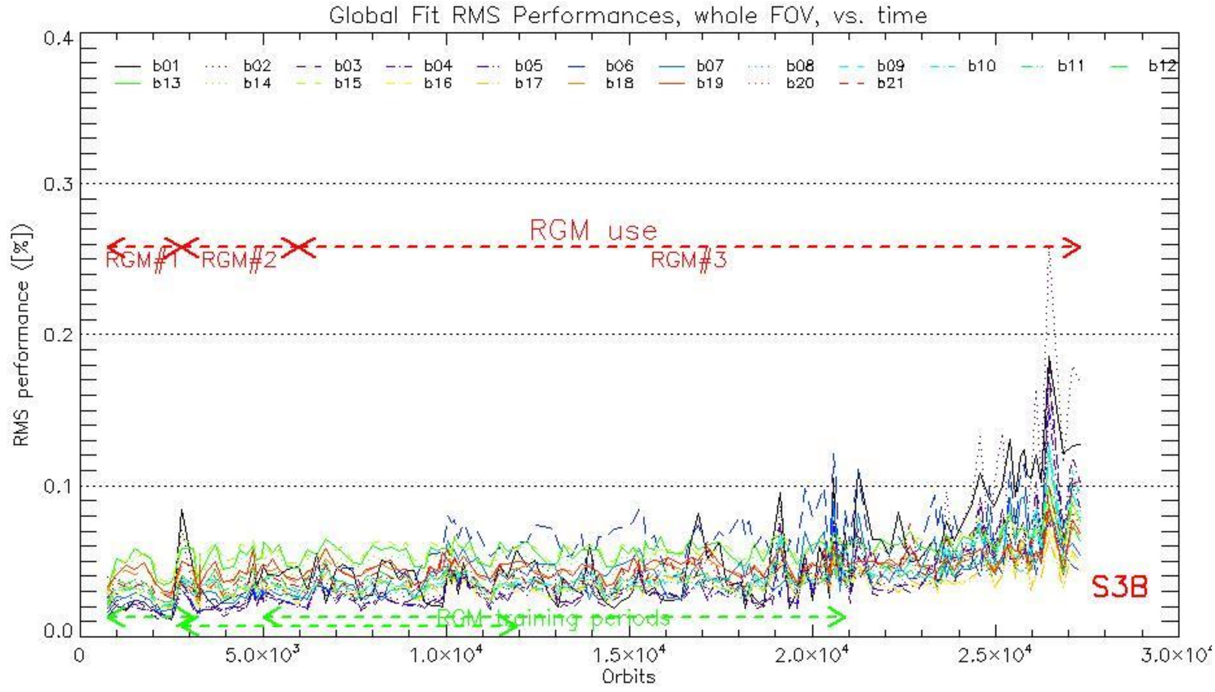

Figure 34: RMS performance of the OLCI-B Gain Model of the previous processing baseline as a function of orbit (please note the different vertical scale with respect to Figure 33).

The overall instrument evolution since channel programming change (18/06/2018) is shown on Figure 35.

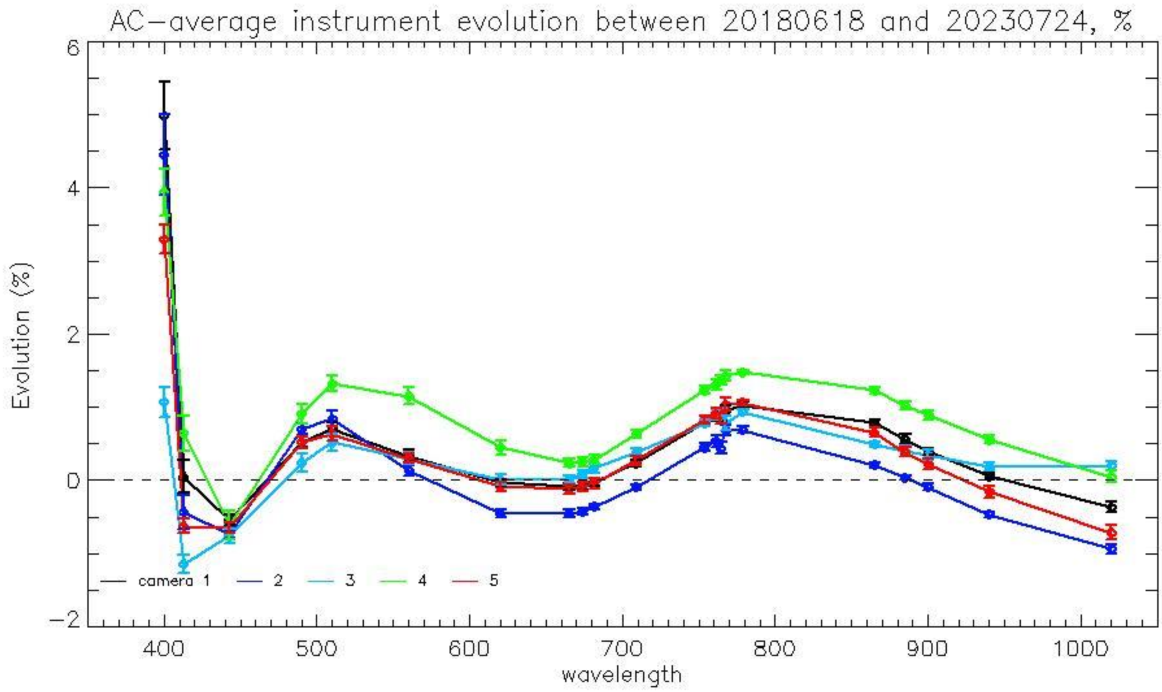

Figure 35: OLCI-B Camera-averaged instrument evolution since channel programming change (18/06/2018) and up to most recent calibration (24/07/2023) versus wavelength.

The overall per camera performance, as a function of wavelength, and at each orbit is shown on Figure 36 as the average and standard deviation of the model over data ratio.

Finally, Figure 37 to Figure 39 show the detail of the model performance, with across-track plots of the model over data ratios at each orbit, one plot for each channel.

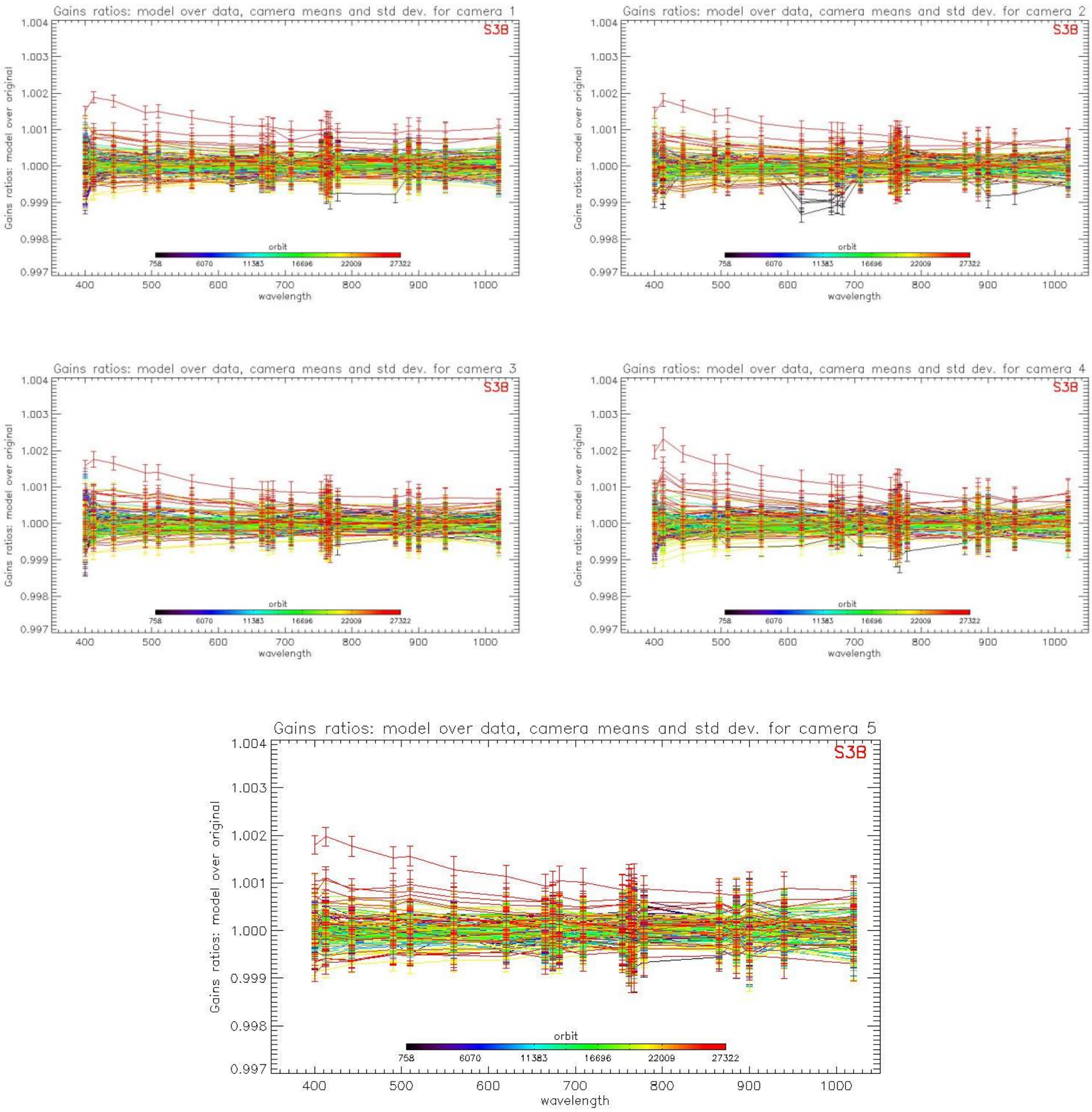

Figure 36: For the 5 cameras: OLCI-B Evolution model performance, as camera-average and standard deviation of ratio of Model over Data vs. wavelength, for each orbit of the test dataset, including 3 calibrations in extrapolation, with a colour code for each calibration from blue (oldest) to red (most recent).

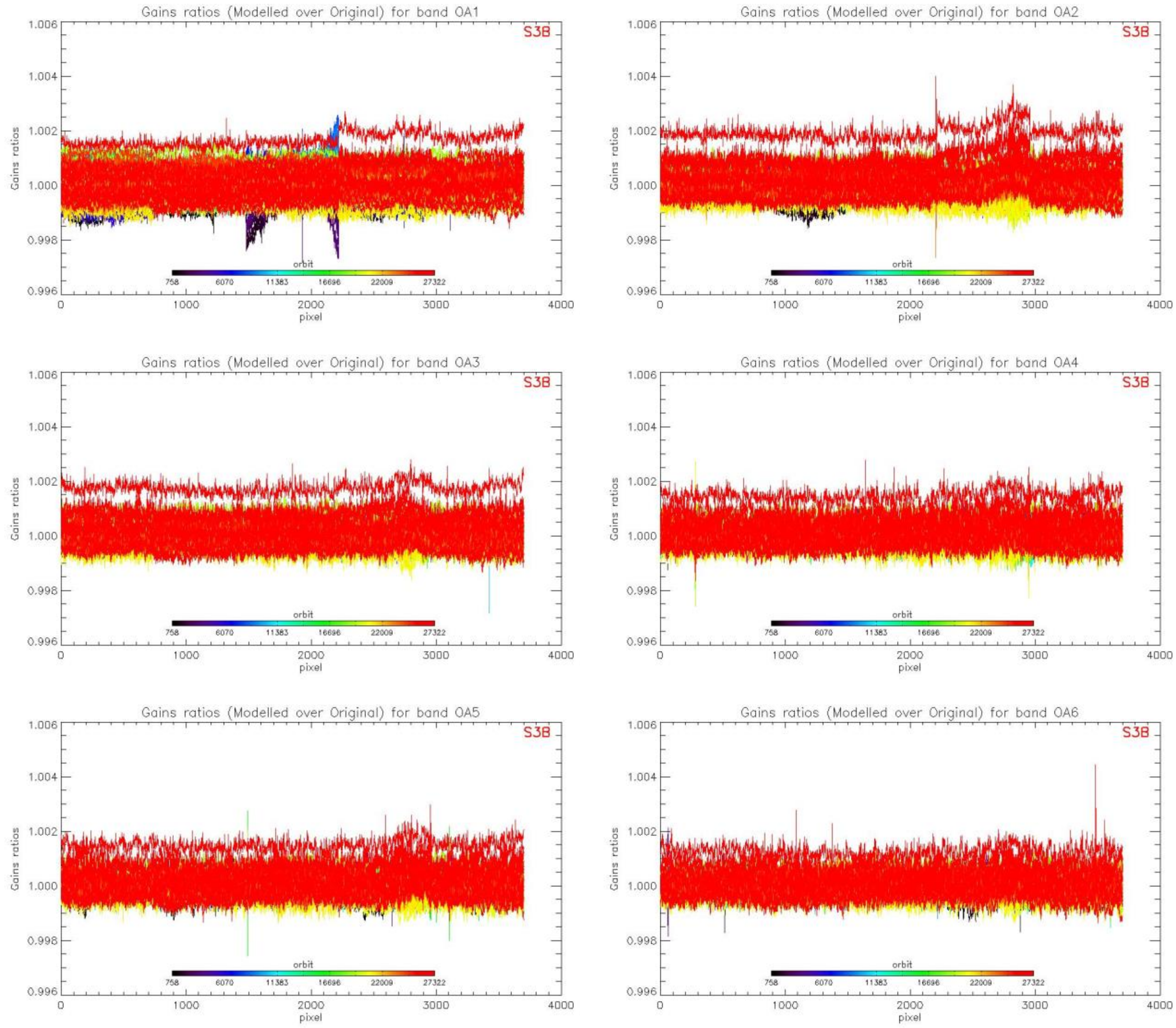

Figure 37: OLCI-B evolution model performance, as ratio of Model over Data vs. pixels, all cameras side by side, over the whole current calibration dataset (since instrument programming update), including 3 calibrations in extrapolation, channels Oa1 to Oa6.

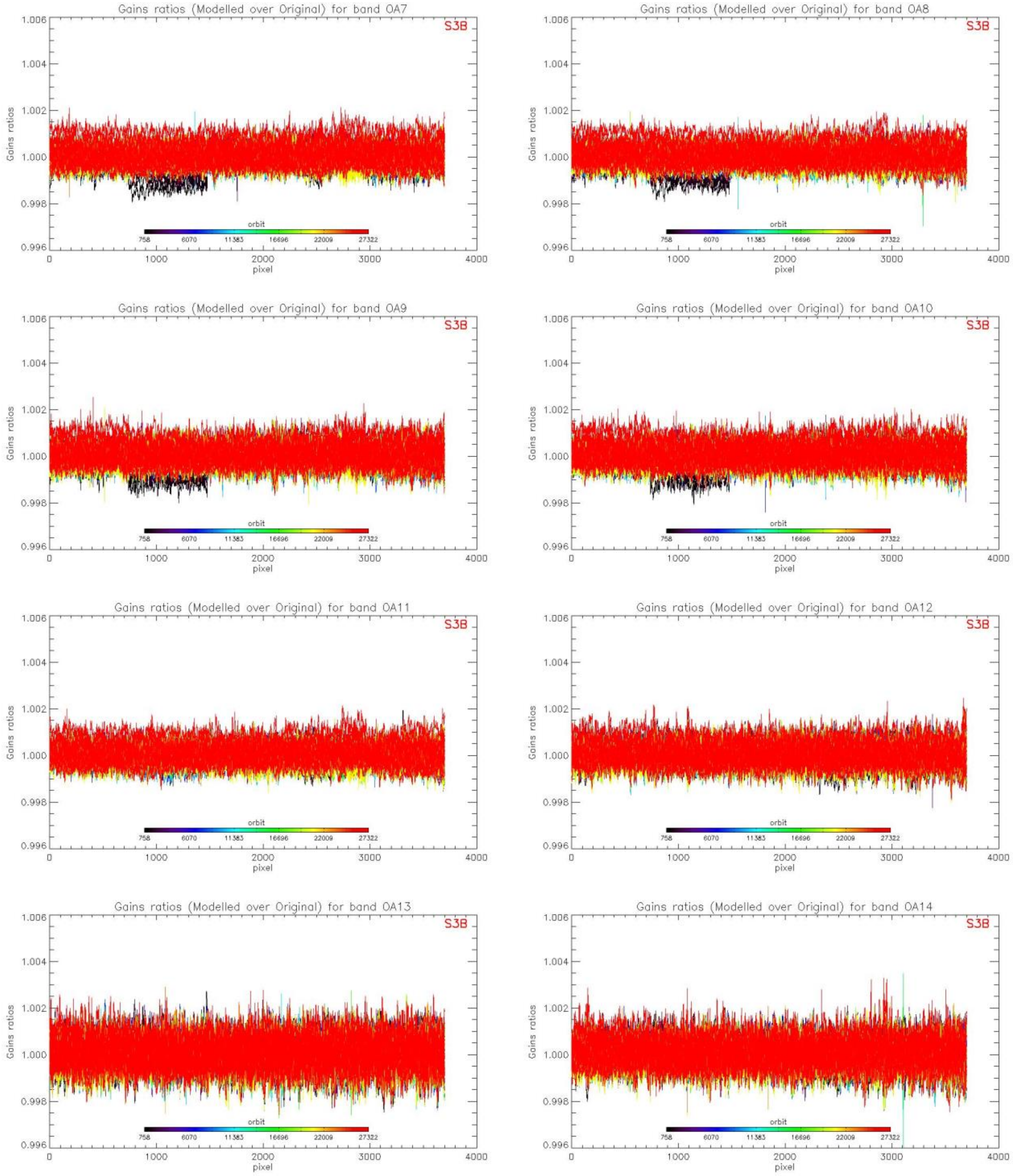

Figure 38: same as Figure 37 for channels Oa7 to Oa14.

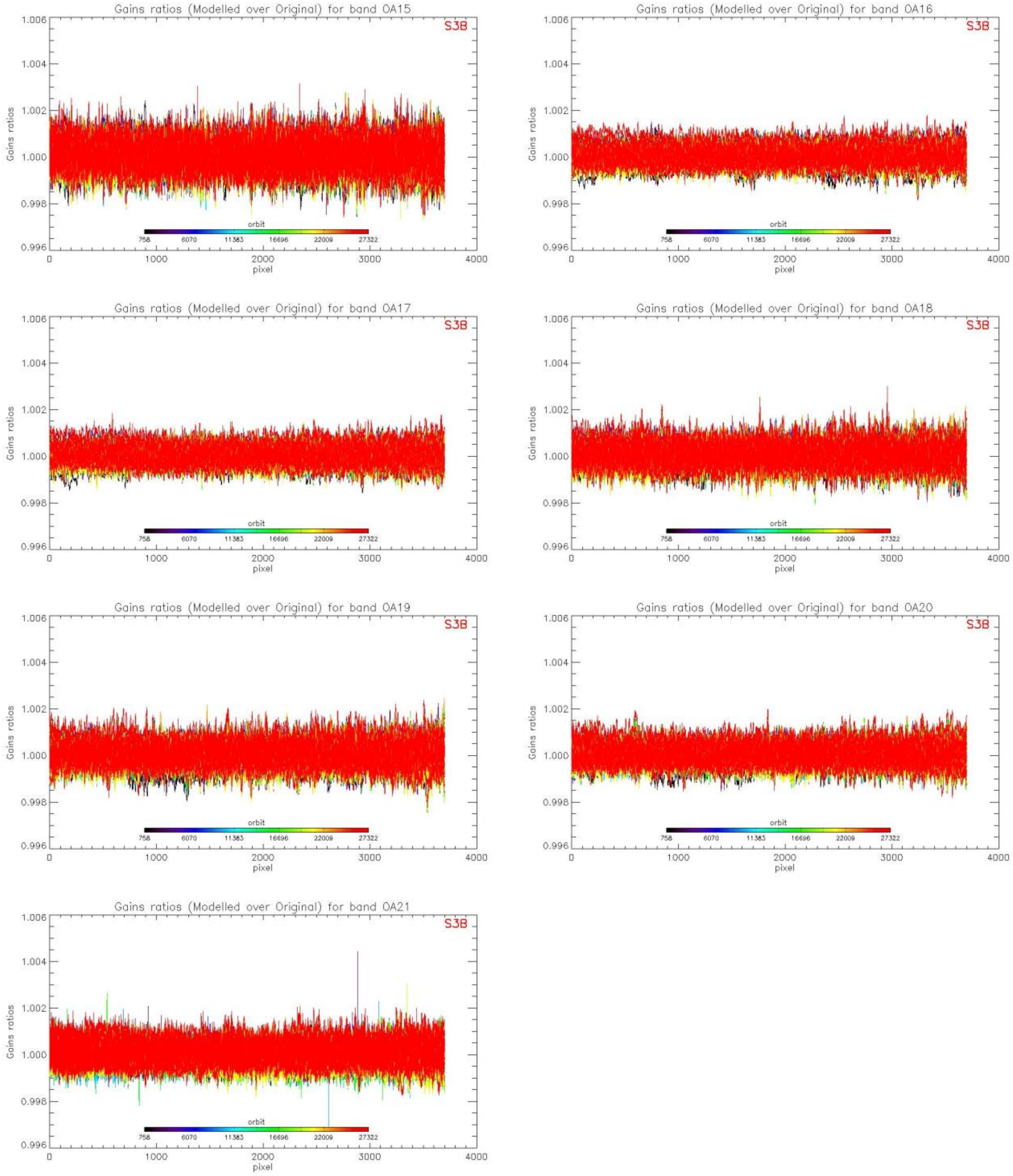

Figure 39: same as for channels Oa15 to Oa21.

2.2.4 Ageing of nominal diffuser [OLCI-L1B-CV-240]

2.2.4.1 OLCI-A

There has been one calibration sequence S05 (reference diffuser) for OLCI-A during the current reported period:

- S05 sequence (diffuser 2) on 23/07/2023 02:36 to 02:38 (absolute orbit 38690)

With the associated S01 sequence (nominal diffuser) in order to compute ageing:

- S01 sequence (diffuser 1) on 23/07/2023 00:55 to 00:57 (absolute orbit 38689)

The diffuser 1 Ageing is computed for each 3700 detector and each spectral band by formula:

Ageing(orb)=G1(orb)/G2(orb)- G1(orb_ref)/G2(orb_ref)

Where:

- G1 is the diffuser 1 (= nominal diffuser) Gain coefficients
- G2 is the diffuser 2 (= reference diffuser) Gain coefficients
- orb_ref is a reference orbit chosen at the beginning of the mission

Ageing is represented in Figure 40 for band Oa01 and in Figure 41 for band Oa17. The negative shift of the sequence at orbit 5832 (for which a slight increase would be expected instead) is not explained so far and still under investigation. It should be noted that the corresponding orbit of diffuser 1 (nominal) has also been detected as an outlier in the modelling of the radiometric long-term trend with an unexpected excess of brightness.

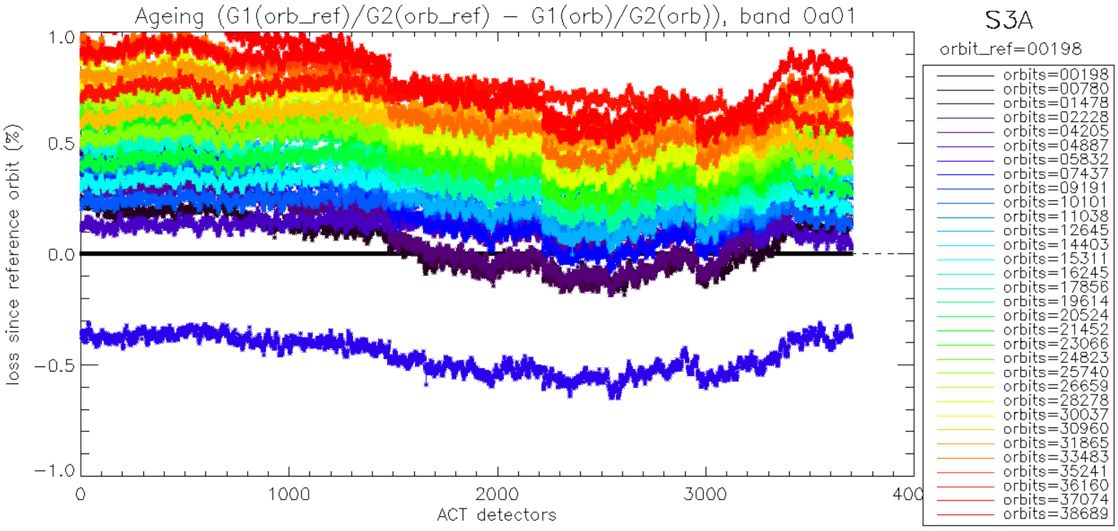

Figure 40: diffuser 1 ageing for spectral band Oa01. We see strong ACT low frequency structures that are due to residual of BRDF modelling.

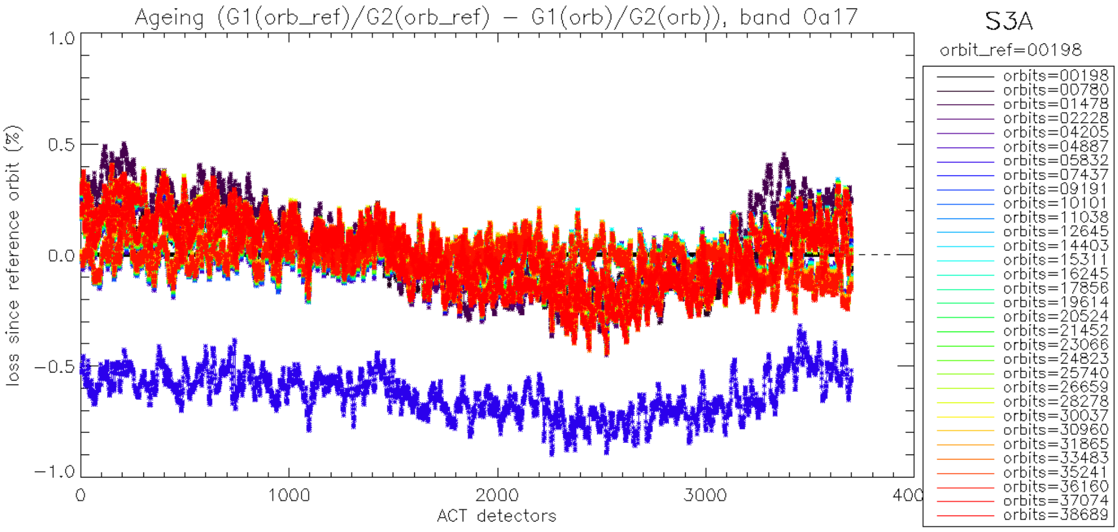

Figure 41: same as Figure 40 for spectral band Oa17. We use this band in order to normalize other bands and remove the ACT structures due to residual of BRDF modelling. Normalized curve for spectral band Oa01 is presented in Figure 42.

Figure 40 and Figure 41 show that the Ageing curves are impacted by a strong ACT pattern which is due to residuals of the bad modelling (on-ground) of the diffuser BRDF. This pattern is dependant of the azimuth angle. It is a 'white' pattern which means it is the same for all spectral bands. As such, we can remove this pattern by normalizing the ageing of all bands by the curve of band Oa17 which is expected not to be impacted by ageing because in the red part of the spectrum. We use an ACT smoothed version (window of 100 detectors) of band Oa17 in order to reduce the high frequency noise. Normalized ageing for spectral band Oa01 is represented in Figure 42 where we can see that this band is impacted by ageing of the diffuser.

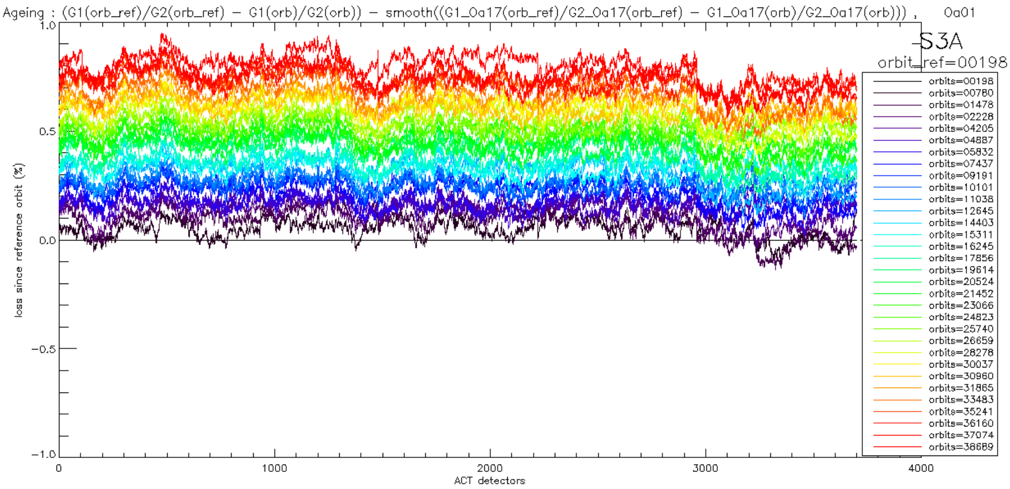

Figure 42: same as Figure 40 after normalization by band Oa17. Ageing of the diffuser 1 is now visible in the 5 cameras.

Camera averaged ageing (normalized by band Oa17) as a function of wavelength is represented in Figure 43 where we can see that ageing is stronger in the 'bluest' spectral bands (short wavelengths). Ageing is clearly visible only for the 6 first spectral bands so far in the OLCI mission life.

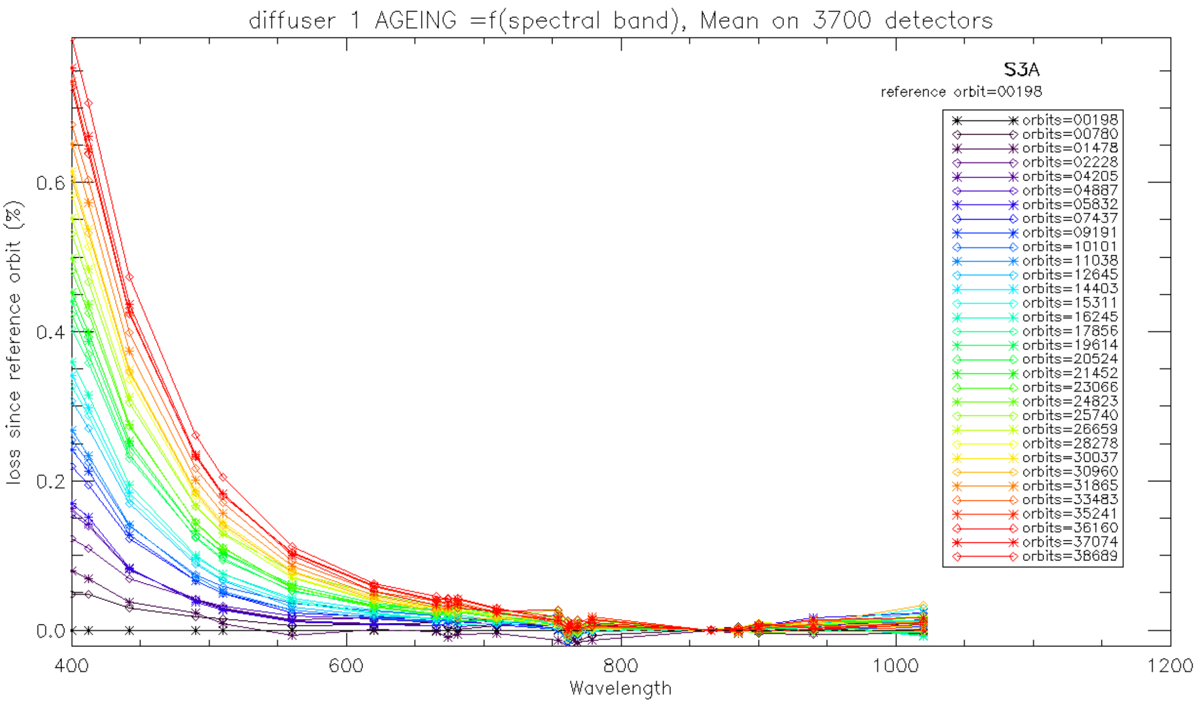

Figure 43: Diffuser 1 ageing as a function of wavelength (or spectral band). Ageing is clearly visible in spectral band #1 to #6. Note that all ageing sequences are plotted but in order to fit in the figure the box legend only displays 1 ageing sequence over 2 (including the most recent one).

Figure 44 shows the evolution, for spectral band Oa01, of the 5 cameras averaged ageing as a function of time.

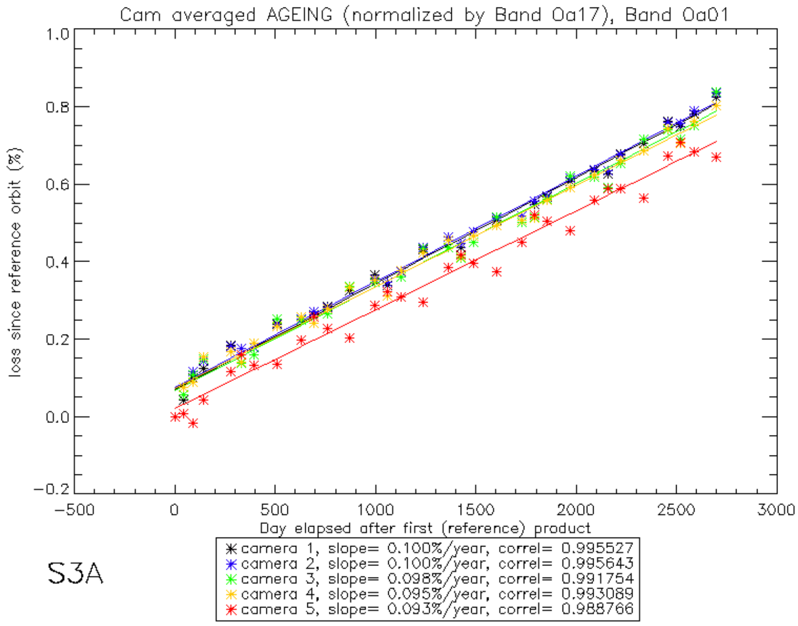

Figure 44: Camera averaged ageing for band Oa01 (normalized by band Oa17) as a function of elapsed time. Linear fit for each camera is plotted. The slope (% loss per year) and the correlation coefficient.

A model of diffuser ageing as a function of cumulated exposure time (i.e. number of acquisition sequence on nominal diffuser, regardless of the band setting) has been built and is described in Cyclic #23 Report. The results of this model confirm the need to model ageing against cumulated exposure rather than elapsed time, as it provides a more linear trend, even if not perfect (see Figure 21 of Cyclic #23 Report).

The slope of this ageing model (% of loss per exposure) as a function of wavelength is presented in Figure 45).

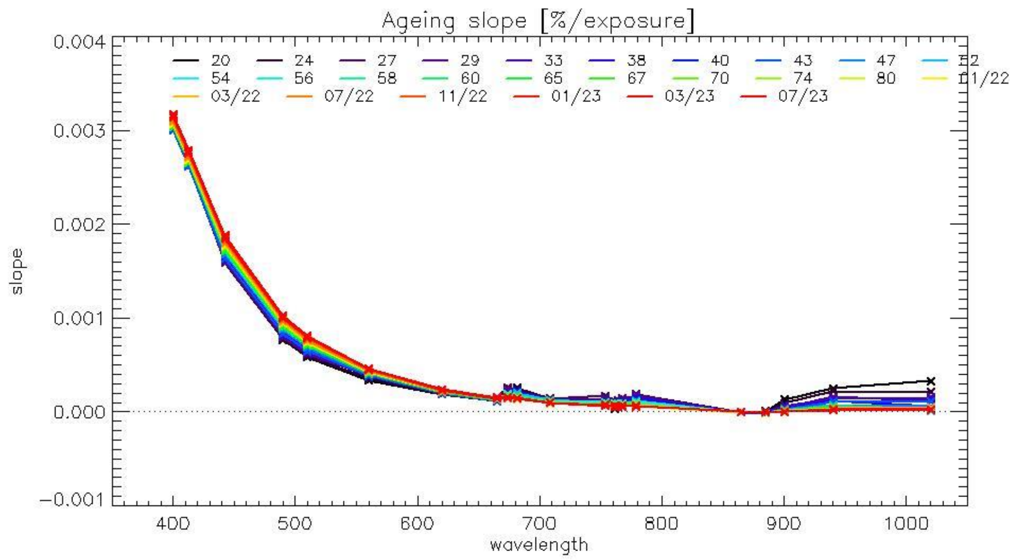

Figure 45: Slope of ageing fit (% of loss per exposure) vs wavelengths, using all the available ageing sequence at the time of the current reporting period (red curve) and at the time of previous reporting periods for which an ageing sequence was measured (see legend within the figure).

In Figure 45, we see that the Ageing slopes have not significantly changed between the current reporting period and the last 25 reporting periods containing a S05 sequence (month #202303, #202301, #202211, #202207, #202203, #202201, cycles #80, #74, #70, #67, #65, #60, #56, #58, #54, #52, #47, #43, #40, #38, #33, #29, #27, #24 and #20). Cycle #47 has been used to derive the Ageing Correction model used for the currently operational Gain Model. The exposure time dependent ageing model is used to derive the Gain Model, the most recent version of which has been put in operations in PDGS on 18th November 2021 (Processing Baseline 3.01).

2.2.4.2 OLCI-B

There has been one calibration sequence S05 (reference diffuser) for OLCI-B during acquisition Cycle 63:

- S05 sequence (diffuser 2) on 24/07/2023 23:24 to 23:26 (absolute orbit 27323)

with the associated S01 sequence in order to compute ageing:

- S01 sequence (diffuser 1) on 24/07/2023 21:43 to 21:45 (absolute orbit 27322)

The diffuser 1 Ageing is computed for each 3700 detector and each spectral band by formula:

Ageing(orb)=G1(orb)/G2(orb)- G1(orb_ref)/G2(orb_ref)

Where:

- G1 is the diffuser 1 (= nominal diffuser) Gain coefficients
- G2 is the diffuser 2 (= reference diffuser) Gain coefficients
- orb_ref is a reference orbit chosen at the beginning of the mission

Ageing is represented in Figure 46 for band Oa01 and in Figure 47 for band Oa17.

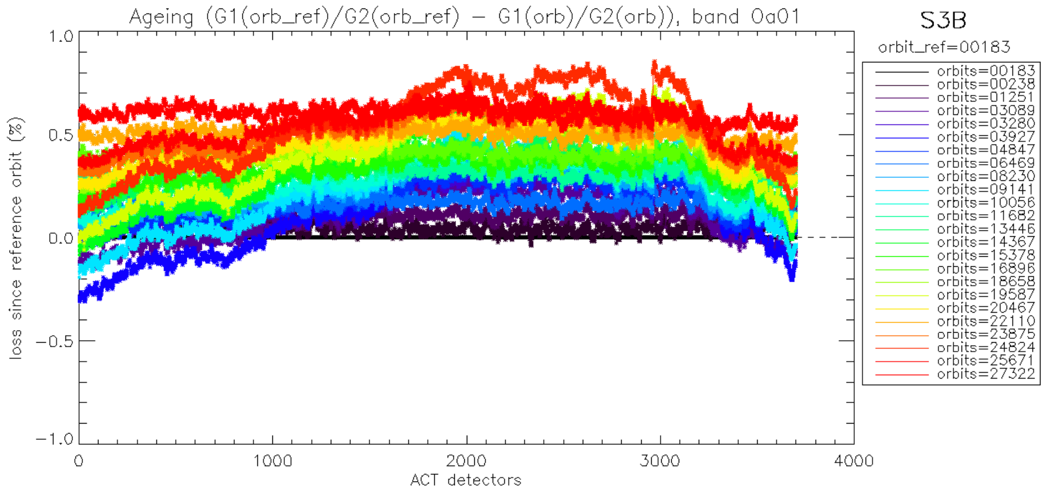

Figure 46: OLCI-B diffuser 1 ageing for spectral band Oa01. We see strong ACT low frequency structures that are due to residual of BRDF modelling.

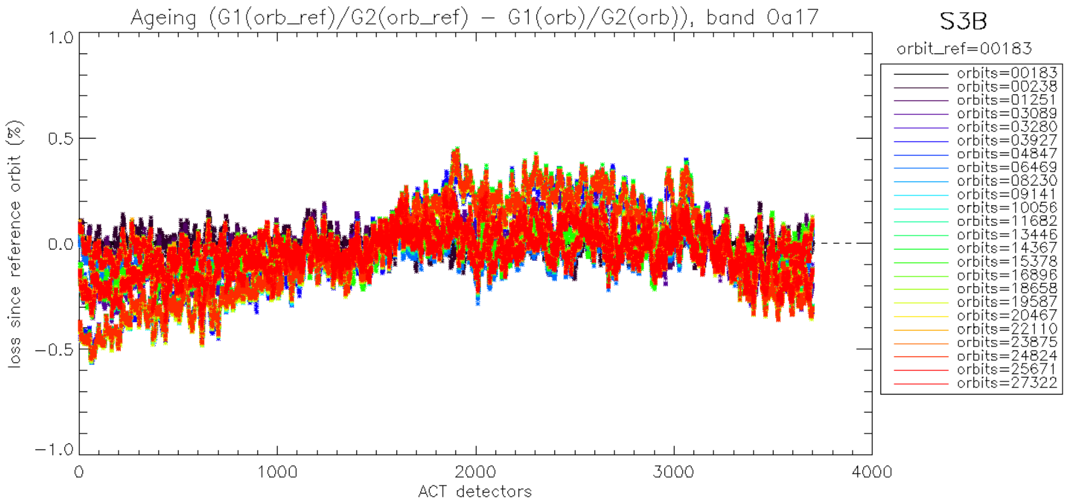

Figure 47: same as Figure 46 for spectral band Oa17. We use this band in order to normalize other bands and remove the ACT structures due to residual of BRDF modelling. Normalized curve for spectral band Oa01 is presented in Figure 48.

Figure 46 and Figure 47 show that the Ageing curves are impacted by a strong ACT pattern which is due to residuals of the bad modelling (on-ground) of the diffuser BRDF. This pattern is dependant of the azimuth angle. It is a 'white' pattern which means it is the same for all spectral bands. As such, we can remove this pattern by normalizing the ageing of all bands by the curve of band Oa17 which is expected not to be impacted by ageing because in the red part of the spectrum. We use an ACT smoothed version (window of 100 detectors) of band Oa17 in order to reduce the high frequency noise. Normalized ageing for spectral band Oa01 is represented in Figure 48 where we can see that this band is impacted by ageing of the diffuser.

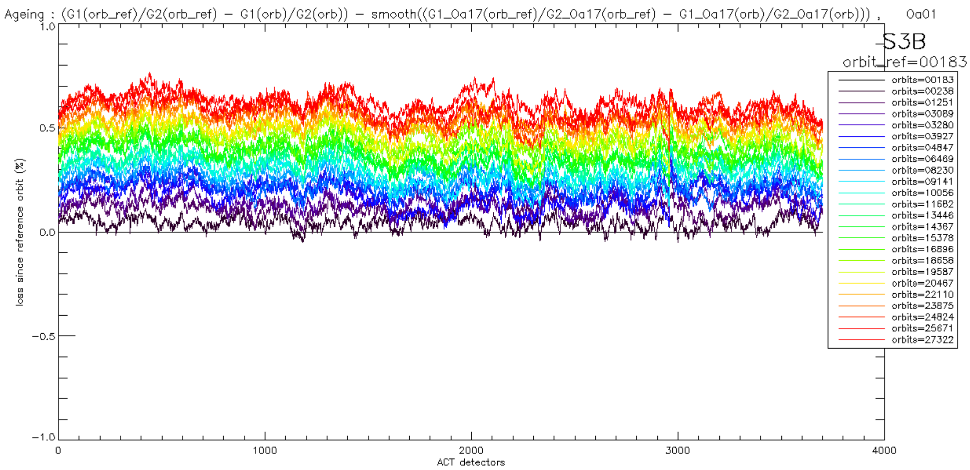

Figure 48: same as Figure 46 after normalization by band Oa17. Ageing of the diffuser 1 is now visible in the 5 cameras.

Camera averaged ageing (normalized by band Oa17) as a function of wavelength is represented in Figure 49 where we can see that ageing is stronger in the 'bluest' spectral bands (short wavelengths). Ageing is clearly visible only for the 5 first spectral bands so far in the OLCI-B mission life. We see a bump around 680 nm which is probably due to characterisation errors that are strongly geometry dependant and affect differently the various camera.

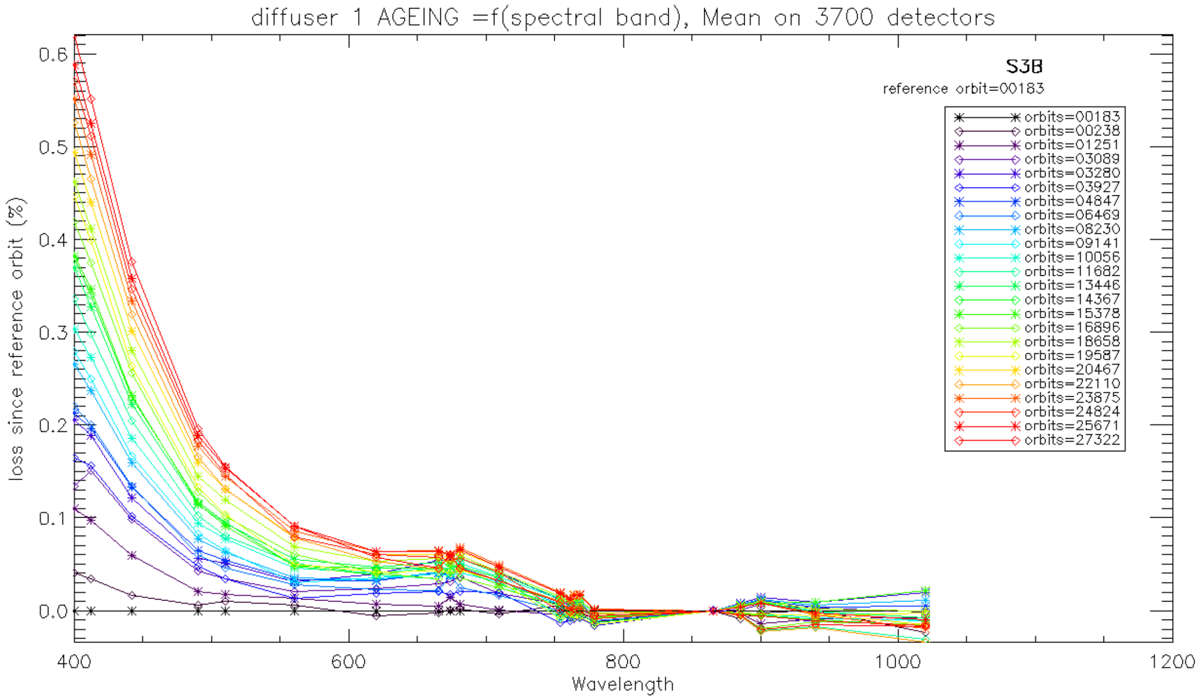

Figure 49: OLCI-B Diffuser 1 ageing as a function of wavelength (or spectral band). Ageing is clearly visible in spectral band #1 to #5.

As for OLCI-A, the OLCI-B Diffuser Ageing has been modelled as a function of cumulated exposure time (i.e. number of acquisition sequence on nominal diffuser, regardless of the band setting). The OLCI-A modelling methodology has been applied to OLCI-B. The results of this modelling, iterated at each new Ageing Sequence acquisition, expressed as the rate of ageing (% of loss per exposure) as a function of wavelength is presented in Figure 50.

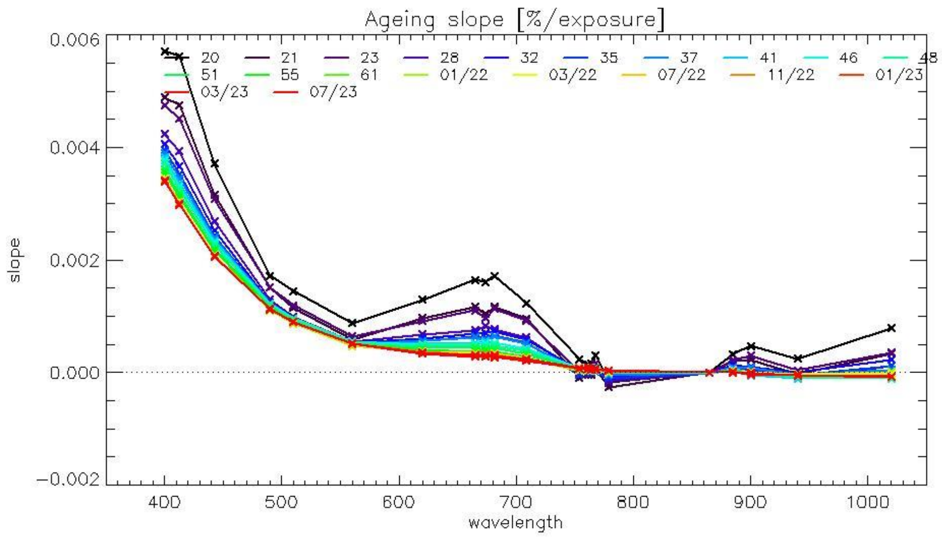

Figure 50: Slope of ageing fit (% of loss per exposure) vs wavelengths, using all the available ageing sequence at the time of the current reporting period (red curve) and at the time of previous reporting periods for which an ageing sequence was measured (see legend within the figure).

The general behaviour of the ageing assessment strongly differs to that of OLCI-A (Figure 45) in two ways: variability with time is much higher and the spectral shape is not as expected. This is interpreted as an unexpected dependency of the *ratio* of diffusers BRDF with illumination conditions. This justified the used of an alternative method using direct comparisons of two nominal diffuser observations, acquired under the same geometry (i.e. directly comparable) and the same day (i.e. with no significant instrument sensitivity evolution) but separated by 7 more exposures to light (during the Yaw Manoeuvres dedicated to the in-flight BRDF modelling). This is in theory the best ageing measurement but as composed of only one measure, it is subject to a large uncertainty. At the time it was derived, it showed a reliable spectral shape up to 850 nm and a good agreement with the nominal assessment in the blue (Figure 51), so that it was used until recently to derive the Radiometric Gain Models. It is referred to as the “YM model”.

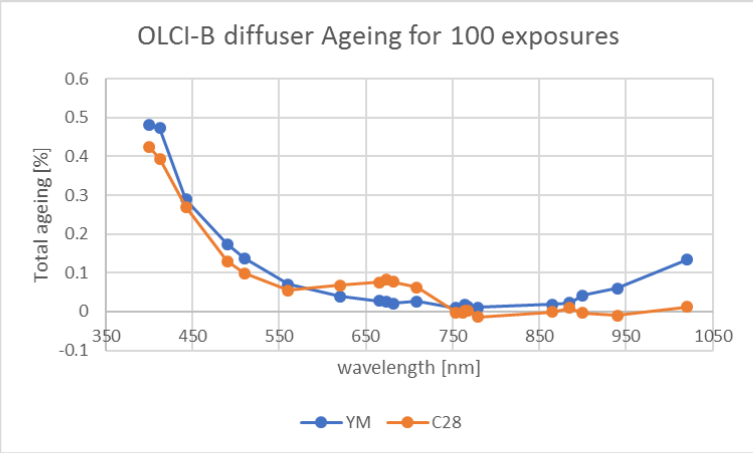

Figure 51: OLCI-B diffuser ageing (after 100 exposures, i.e. about two years) according to direct assessment from Yaw Manoeuvres (blue) and nominal method at Cycle 28 (orange).

The regular decrease of the ageing slopes according to the nominal method makes YM ageing model more and more overestimated, and a new method has been defined and presented in previous DQM. This method has been applied, including the latest ageing assessment mentioned above.

As the anomalous ageing estimated in the red have shown to be correlated with Sun illumination geometry, a reanalysis of the Ageing sequences has been done on sub-sets of sequences with equal or close illumination conditions. Once sorted by Sun azimuth angles, a set of 3 clusters (Figure 52) provide independent ageing estimates. The estimates quality can be inferred from in-FOV consistency, both inside each camera and between cameras, as the diffuser ageing is independent of the viewing direction. The final estimate is a weighted average of the clusters assessments.

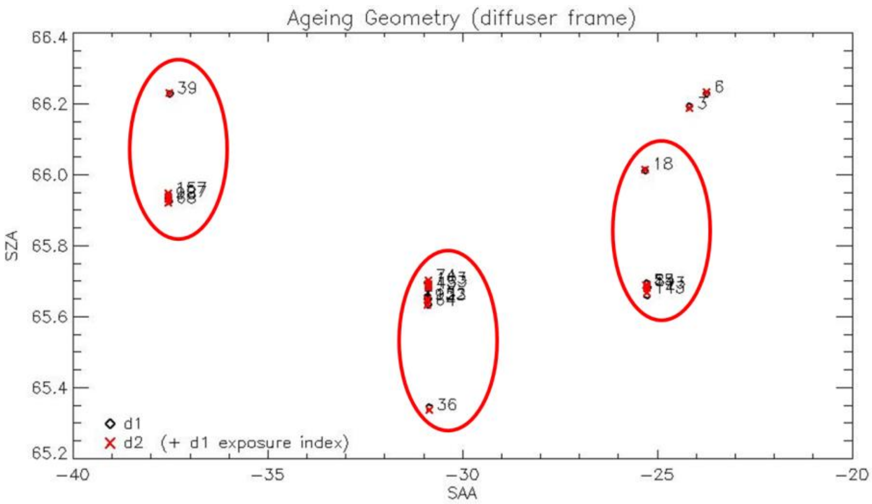

Figure 52: clustered Ageing sequences illumination geometries.

The results are quite satisfactory with good in-FOV consistency, well improved with respect to other methods, and a rather good inter-cluster consistency. The final results, together with those of the two other methods, are shown on Figure 53: the variation between the two Ageing slopes estimates of 20220331, 20221125 and 20230331 are extremely small.

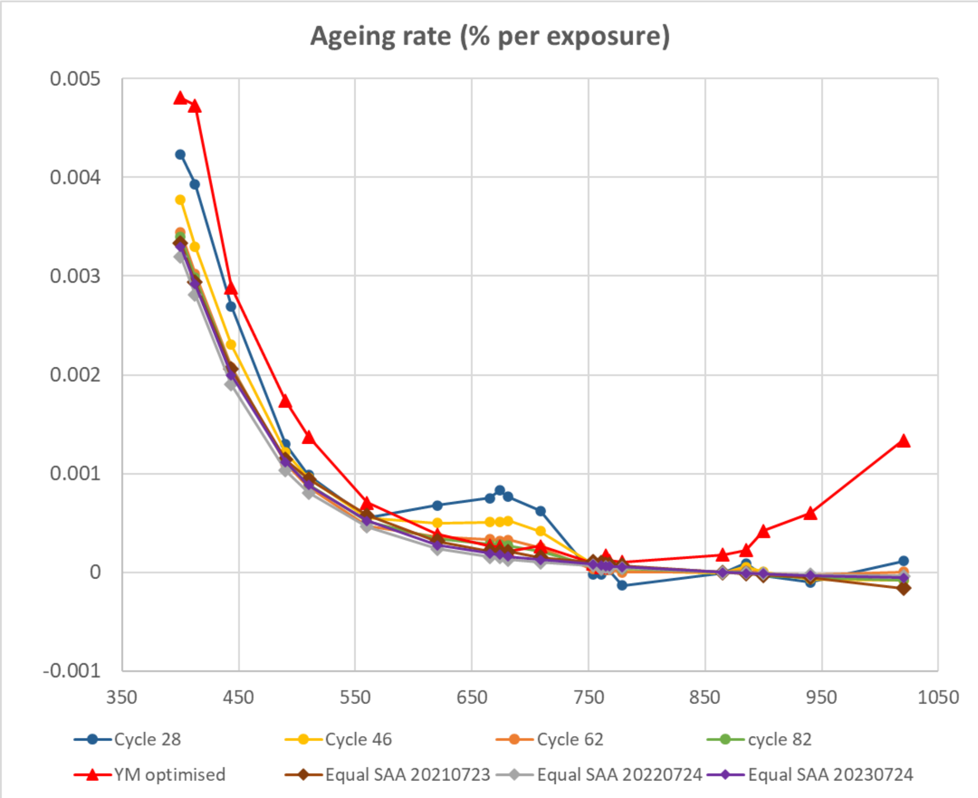

Figure 53: various estimates of the ageing rate, according to nominal method for cycles 28, 46, 62 and 82 according to direct assessment during Yaw manoeuvres, and according to the Equal SAA clustering for data up to 07/2021, 07/2022 and 07/2023.

2.2.5 Updating of calibration ADF [OLCI-L1B-CV-260]

2.2.5.1 OLCI-A

The following OLCI-A CAL_AX ADF, delivered to PDGS during the previous reporting period, has been deployed in the Ground Segment as party of Processing Baseline OL__L1_.003.03.00 (see §1.1):

S3A_OL_1_CAL_AX_20230620T000000_20991231T235959_20230616T120000___________________MPC_O_AL_028.SEN3

It includes revised Radiometric Gain Model and Geometric Calibration.

2.2.5.2 OLCI-B

The following OLCI-B CAL_AX ADF, delivered to PDGS during the previous report period , has been deployed in the Ground Segment as party of Processing Baseline OL__L1_.003.03.00 (see §1.2):

S3B_OL_1_CAL_AX_20230620T000000_20991231T235959_20230616T120000___________________MPC_O_AL_018.SEN3

It includes revised Radiometric Gain Model and Geometric Calibration.

2.3 Spectral Calibration [OLCI-L1B-CV-400]

2.3.1 OLCI-A

There was no S02+S03 nor S09 Spectral Calibration for OLCI-B in the current reporting period.

Consequently, the last spectral calibration results presented in May 2023 DQR stay valid.

2.3.2 OLCI-B

There was no S02+S03 nor S09 Spectral Calibration for OLCI-B in the reporting period:

Consequently, the last spectral calibration results presented in May 2023 DQR stay valid.

2.4 Signal to Noise assessment [OLCI-L1B-CV-620]

2.4.1 SNR from Radiometric calibration data

2.4.1.1 OLCI-A

SNR computed for all calibration data (S01, S04 and S05 sequences) as a function of band number is presented in Figure 54.

SNR computed for all calibration data as a function of orbit number for band Oa01 (the less stable band) is presented in Figure 55.

There is no significant evolution of this parameter during the current reporting period and the ESA requirement is fulfilled for all bands.

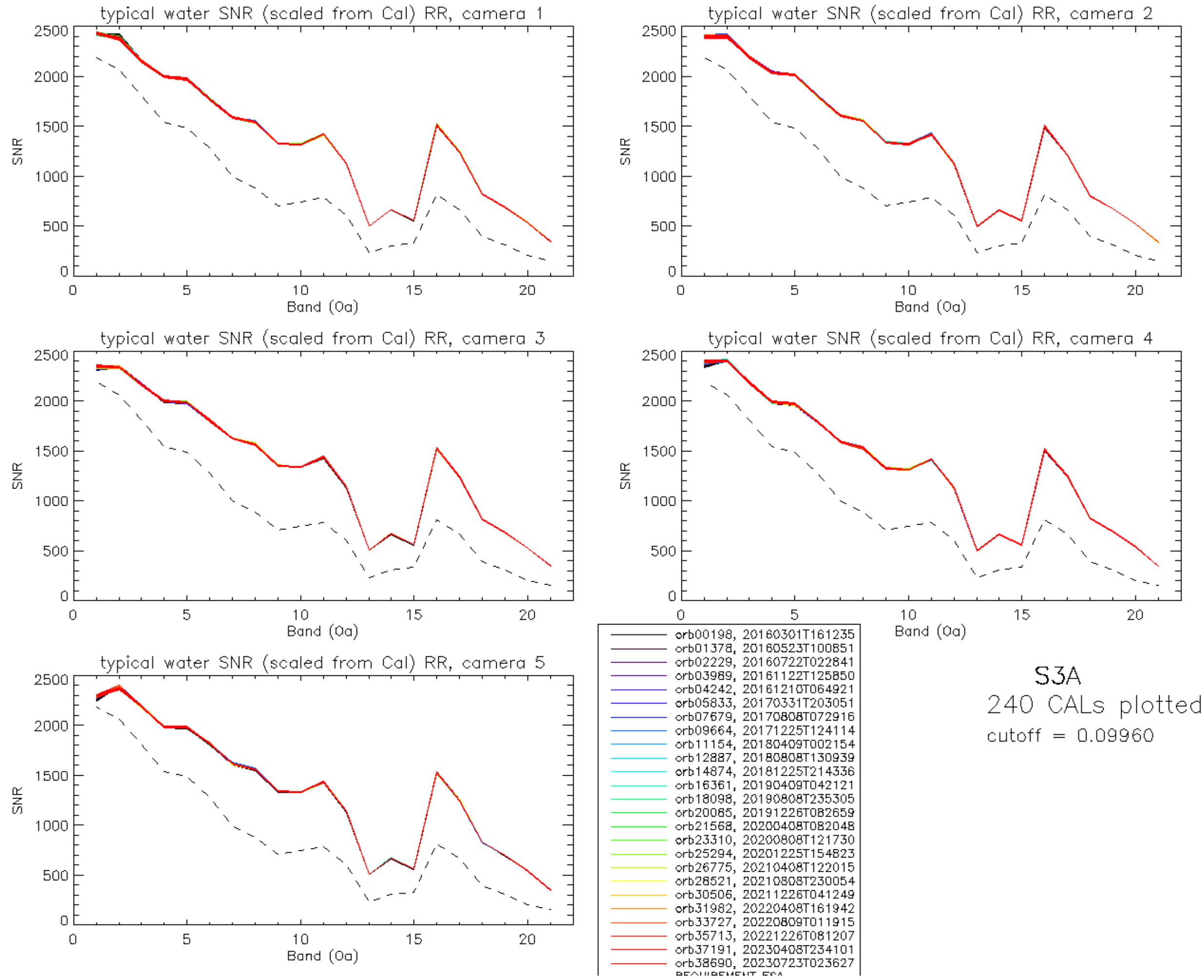

Figure 54: OLCI-A Signal to Noise ratio as a function of the spectral band for the 5 cameras. These results have been computed from radiometric calibration data. All calibrations except first one (orbit 183) are presents with the colours corresponding to the orbit number (see legend). The SNR is very stable with time: the curves for all orbits are almost superimposed. The dashed curve is the ESA requirement.

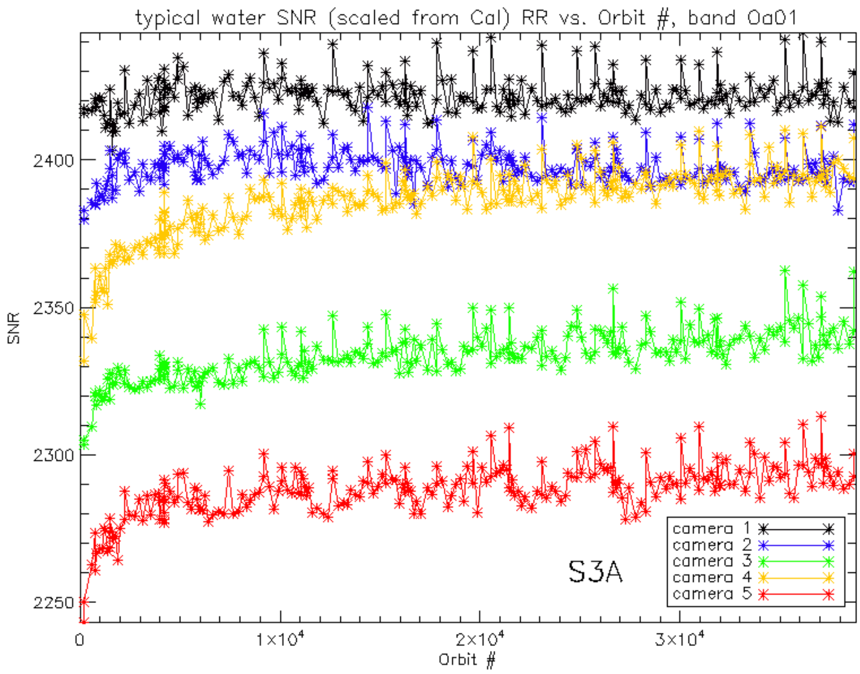

Figure 55: long-term stability of the SNR estimates from Calibration data, example of channel Oa1.

The mission averaged SNR figures are provided in Table 1 below, together with their radiance reference level. According to the OLCI SNR requirements, these figures are valid at these radiance levels and at Reduced Resolution (RR, 1.2 km). They can be scaled to other radiance levels assuming shot noise (CCD sensor noise) is the dominating term, i.e. radiometric noise can be considered Gaussian with its standard deviation varying as the square root of the signal; in other words: $SNR(L) = SNR(L_{ref}) \cdot \sqrt{\frac{L}{L_{ref}}}$. Following the same assumption, values at Full Resolution (300m) can be derived from RR ones as 4 times smaller.

Table 1: OLCI-A SNR figures as derived from Radiometric Calibration data. Figures are given for each camera (time average and standard deviation), and for the whole instrument. The requirement and its reference radiance level are recalled (in $mW.sr^{-1}.m^{-2}.nm^{-1}$).

	L_{ref}	SNR	C1		C2		C3		C4		C5		All	
nm	LU	RQT	avg	*std*	avg	*std*	avg	*std*	avg	*std*	avg	*std*	avg	*std*
400.000	63.0	2188	2421	6.2	2397	6.3	2333	8.5	2385	12.1	2288	9.3	2365	7.1
412.000	74.1	2061	2386	9.6	2402	7.7	2339	5.0	2400	5.1	2379	9.4	2381	6.0
442.000	65.6	1811	2157	6.1	2195	6.2	2163	5.0	2185	4.3	2193	6.0	2179	4.3
490.000	51.2	1541	1999	4.8	2036	4.8	1998	4.3	1984	4.4	1988	4.4	2001	3.2
510.000	44.4	1488	1978	5.4	2014	4.9	1986	4.4	1967	4.3	1985	4.2	1986	3.3
560.000	31.5	1280	1775	4.7	1802	4.1	1803	4.8	1794	3.9	1819	3.3	1799	3.0
620.000	21.1	997	1590	4.1	1608	4.3	1624	3.2	1593	3.3	1615	3.4	1606	2.5
665.000	16.4	883	1545	4.2	1556	4.6	1566	3.9	1533	3.6	1561	3.6	1552	3.0
674.000	15.7	707	1328	3.4	1336	3.8	1350	2.8	1323	3.3	1343	3.3	1336	2.4
681.000	15.1	745	1319	3.7	1325	3.4	1337	2.7	1314	2.5	1334	3.3	1326	2.2
709.000	12.7	785	1420	4.2	1420	4.1	1435	3.4	1414	3.5	1431	3.0	1424	2.7
754.000	10.3	605	1127	3.1	1121	2.8	1136	3.1	1125	2.5	1139	2.6	1130	2.1
761.000	6.1	232	502	1.1	499	1.1	505	1.1	501	1.1	508	1.3	503	0.8
764.000	7.1	305	663	1.5	658	1.5	668	2.0	662	1.5	670	2.0	664	1.2
768.000	7.6	330	558	1.4	554	1.2	563	1.3	557	1.3	564	1.2	559	0.9
779.000	9.2	812	1516	4.6	1498	4.4	1527	5.0	1512	4.8	1527	4.7	1516	4.0
865.000	6.2	666	1243	3.5	1213	3.4	1240	3.8	1247	3.5	1250	2.7	1239	2.7
885.000	6.0	395	823	1.7	801	1.6	814	1.9	824	1.5	831	1.6	819	1.1
900.000	4.7	308	690	1.6	673	1.3	683	1.6	693	1.6	698	1.4	688	1.0
940.000	2.4	203	534	1.2	522	1.2	525	1.0	539	1.1	542	1.3	532	0.7
1020.000	3.9	152	345	0.9	337	0.8	348	0.7	345	0.8	351	0.8	345	0.5

2.4.1.2 OLCI-B

SNR computed for all OLCI-B calibration data (S01, S04 (but not the dark-only S04) and S05 sequences) as a function of band number is presented in Figure 56.

SNR computed for all OLCI-B calibration data as a function of orbit number for band Oa01 (the less stable band) is presented in Figure 57.

As for OLCI-A the SNR is very stable in time. There is no significant evolution of this parameter during the current reporting and the ESA requirement is fulfilled for all bands.

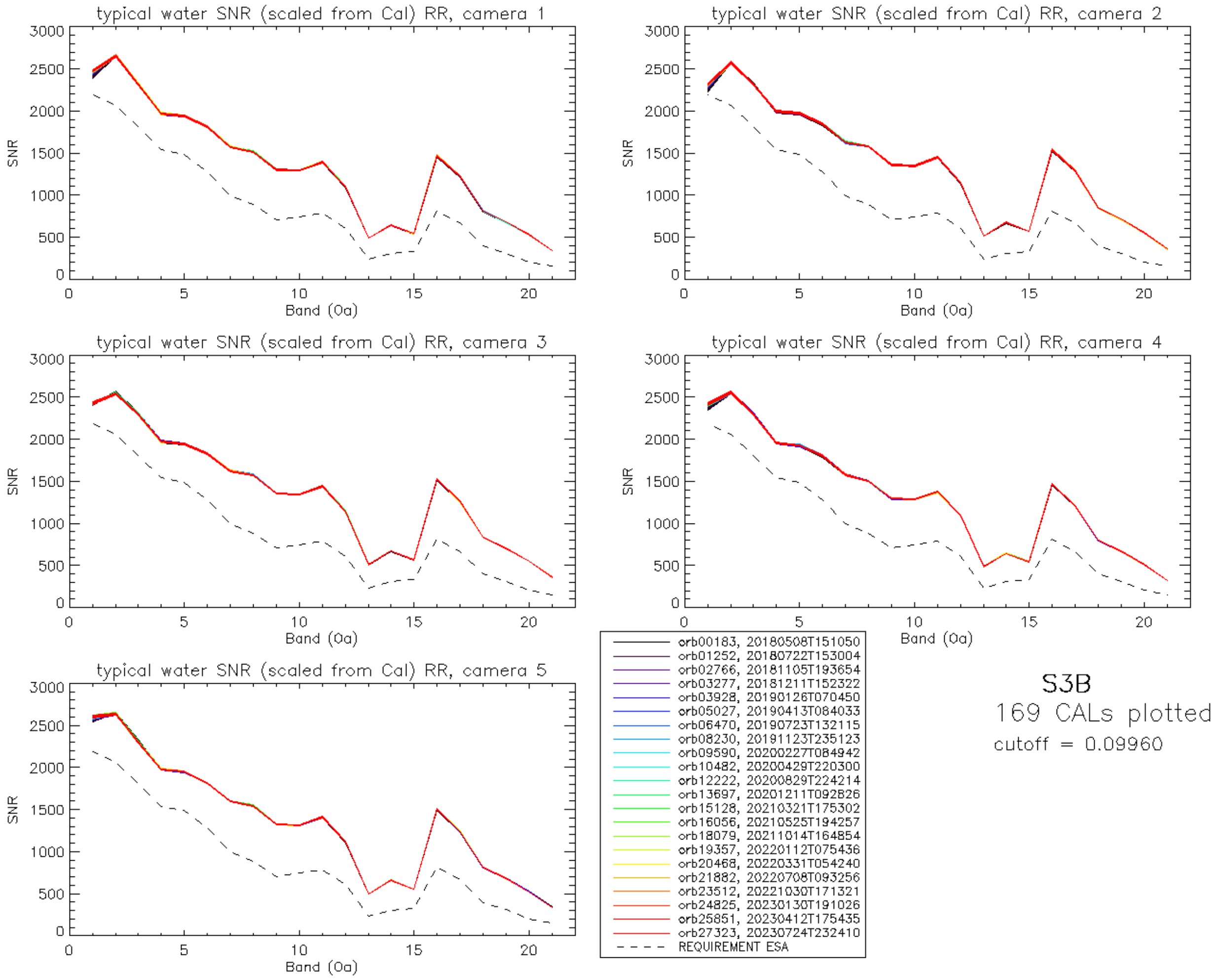

Figure 56: OLCI-B Signal to Noise ratio as a function of the spectral band for the 5 cameras. These results have been computed from radiometric calibration data. All calibrations except first one (orbit 167) are presents with the colours corresponding to the orbit number (see legend). The SNR is very stable with time: the curves for all orbits are almost superimposed. The dashed curve is the ESA requirement.

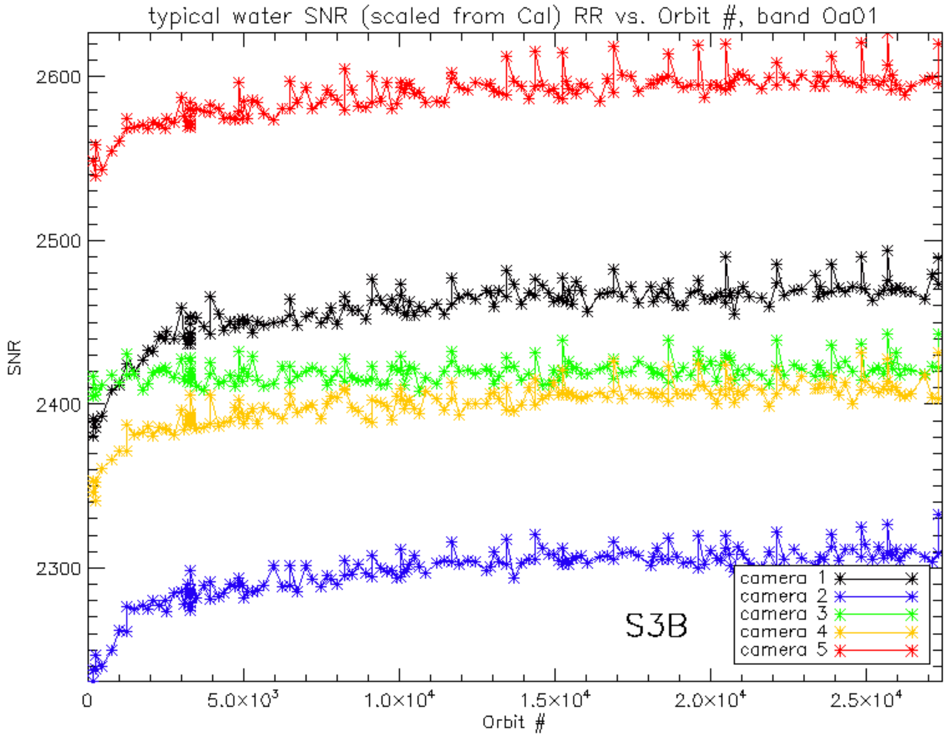

Figure 57: long-term stability of the OLCI-B SNR estimates from Calibration data, example of channel Oa1.

Table 2: OLCI-B SNR figures as derived from Radiometric Calibration data. Figures are given for each camera (time average and standard deviation), and for the whole instrument. The requirement and its reference radiance level are recalled (in mW.sr^{-1}.m^{-2}.nm^{-1}).

	L_{ref}	SNR	C1		C2		C3		C4		C5		All	
nm	LU	RQT	avg	*std*	avg	*std*	avg	*std*	avg	*std*	avg	*std*	avg	*std*
400.000	63.0	2188	2458	18.7	2297	16.5	2420	6.8	2400	14.0	2589	14.2	2433	13.1
412.000	74.1	2061	2654	7.1	2569	6.6	2542	8.9	2550	6.5	2636	7.9	2590	5.9
442.000	65.6	1811	2323	6.8	2315	6.5	2298	7.1	2301	7.1	2307	6.8	2309	5.9
490.000	51.2	1541	1966	4.8	1990	5.6	1971	5.1	1952	4.7	1979	4.5	1972	3.9
510.000	44.4	1488	1939	4.8	1968	6.0	1942	5.0	1925	4.9	1952	4.8	1945	4.1
560.000	31.5	1280	1813	4.7	1848	4.8	1829	4.7	1805	4.7	1817	3.9	1822	3.6
620.000	21.1	997	1572	4.3	1626	4.6	1624	3.9	1576	3.6	1600	3.6	1600	3.0
665.000	16.4	883	1513	4.1	1578	3.8	1573	3.8	1501	3.0	1546	3.7	1542	2.8
674.000	15.7	707	1300	3.9	1358	3.6	1353	3.1	1292	2.7	1328	2.9	1326	2.4
681.000	15.1	745	1293	3.5	1347	3.3	1343	3.0	1285	2.8	1316	2.8	1317	2.2
709.000	12.7	785	1390	4.0	1447	4.0	1443	4.1	1373	2.9	1412	3.7	1413	3.0
754.000	10.3	605	1096	3.5	1143	3.6	1142	3.3	1089	2.8	1116	3.2	1117	2.8
761.000	6.1	232	488	1.2	509	1.2	509	1.3	486	1.2	498	1.3	498	1.0
764.000	7.1	305	643	1.6	673	2.0	672	1.8	641	1.8	658	1.8	657	1.5
768.000	7.6	330	541	1.4	568	1.4	564	1.3	541	1.3	555	1.5	554	1.0
779.000	9.2	812	1467	4.1	1535	4.6	1527	5.1	1468	4.0	1507	4.1	1501	3.7
865.000	6.2	666	1221	3.5	1288	3.7	1258	3.6	1206	3.6	1238	2.8	1242	2.8
885.000	6.0	395	808	2.2	848	1.9	834	2.0	799	1.8	815	2.1	821	1.5
900.000	4.7	308	679	1.5	714	1.9	704	1.7	670	1.5	683	1.5	690	1.2
940.000	2.4	203	527	1.3	549	1.6	551	1.2	510	1.1	522	1.3	532	0.9
1020.000	3.9	152	336	0.8	358	1.2	358	0.8	318	0.7	338	0.9	342	0.6

2.5 Geometric Calibration/Validation

2.5.1 OLCI-A

OLCI-A georeferencing performance is compliant since the introduction of MPC Geometric Calibration, put in production on the 14th of March 2018. It has however significantly improved after its last full revision of GCMs (Geometric Calibration Models, or platform to instrument alignment quaternions) and IPPVMs (Instrument Pixels Pointing Vectors) both derived using the GeoCal Tool and put in production on 30/07/2019.

The following figures (Figure 58 to Figure 63) show time series of the overall RMS performance (requirement criterion) and of the across-track and along-track biases for each camera. New plots (Figure 64 and Figure 65) introduce monitoring of the performance homogeneity within the field of view: georeferencing errors in each direction at camera transitions (difference between last pixel of camera N and first pixel of camera N+1) and within a given camera (maximum bias minus minimum inside each camera). The performance improvement since the 30/07/2019 is significant on most figures: the global RMS value decreases form around 0.35 to about 0.2 (Figure 58), the across-track biases decrease significantly for all cameras (Figure 59 to Figure 63), the along-track bias reduces for at least camera 3 (Figure 61) and the field of view homogeneity improves drastically (Figure 64 and Figure 65, but also reduction of the dispersion – distance between the ± 1 sigma lines – in Figure 59 to Figure 63).

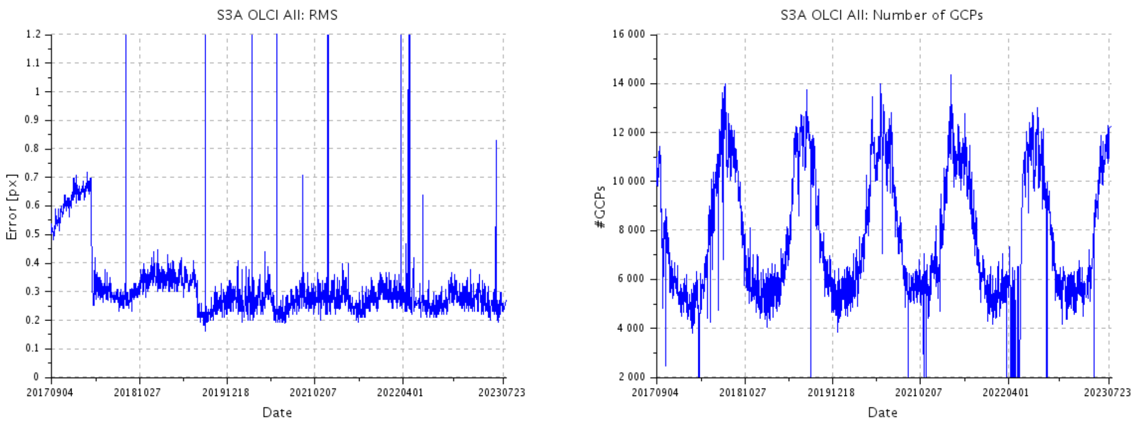

Figure 58: overall OLCI-A georeferencing RMS performance time series (left) and number of validated control points corresponding to the performance time series (right) over the whole monitoring period

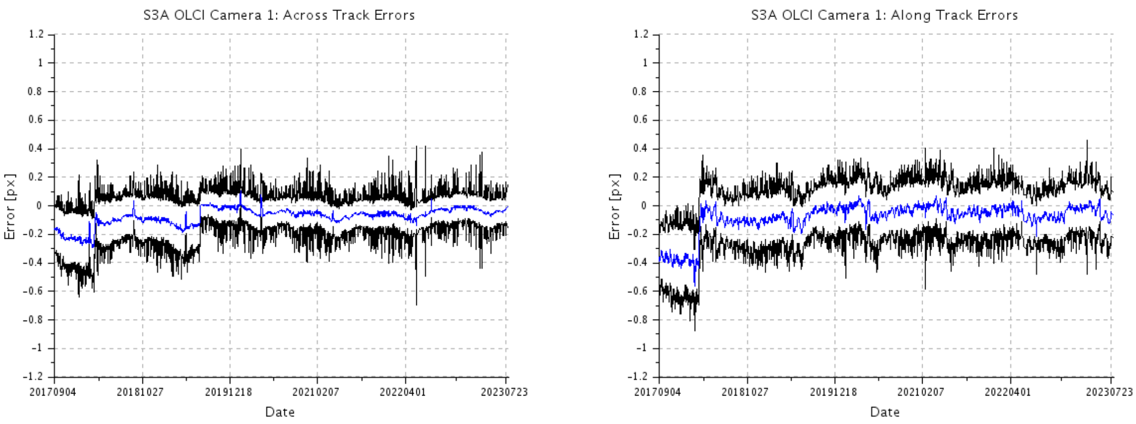

Figure 59: across-track (left) and along-track (right) OLCI-A georeferencing biases time series for Camera 1. Blue line is the average, black lines are average plus and minus 1 sigma.

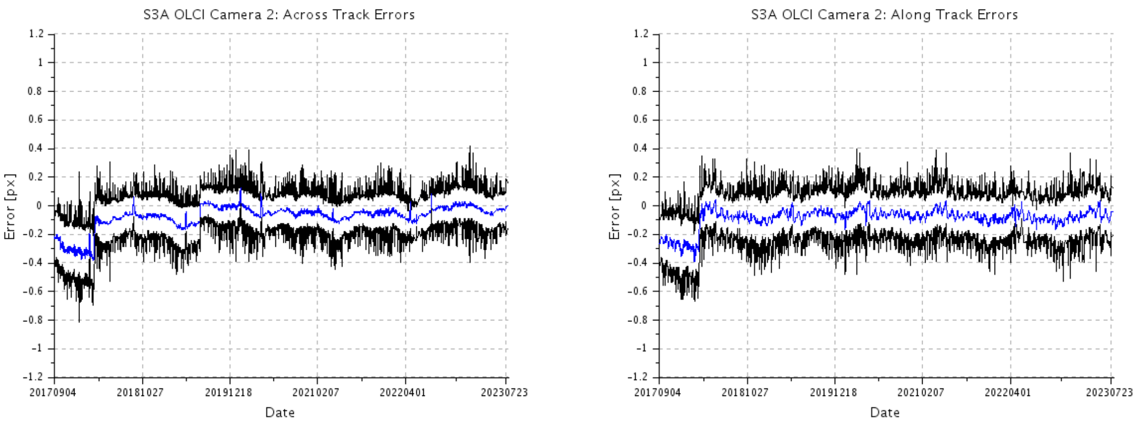

Figure 60: same as Figure 59 for Camera 2.

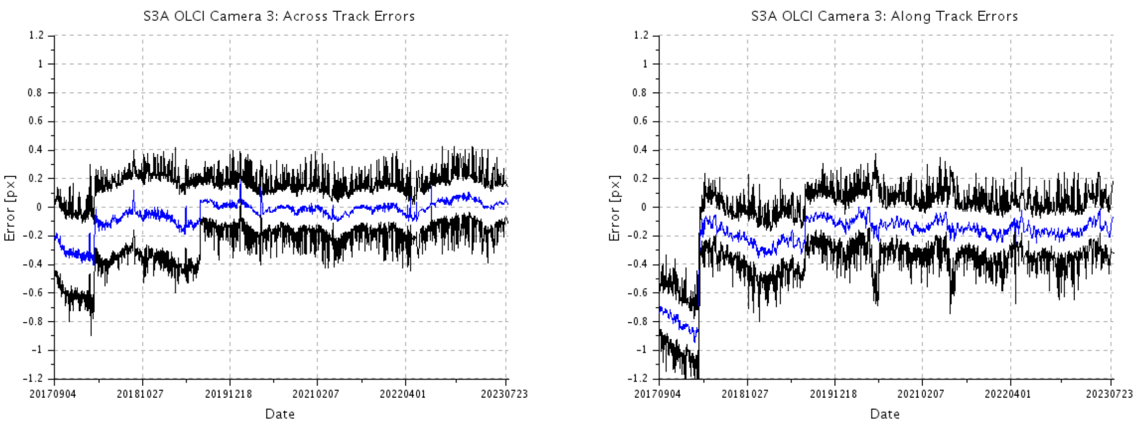

Figure 61: same as Figure 59 for Camera 3.

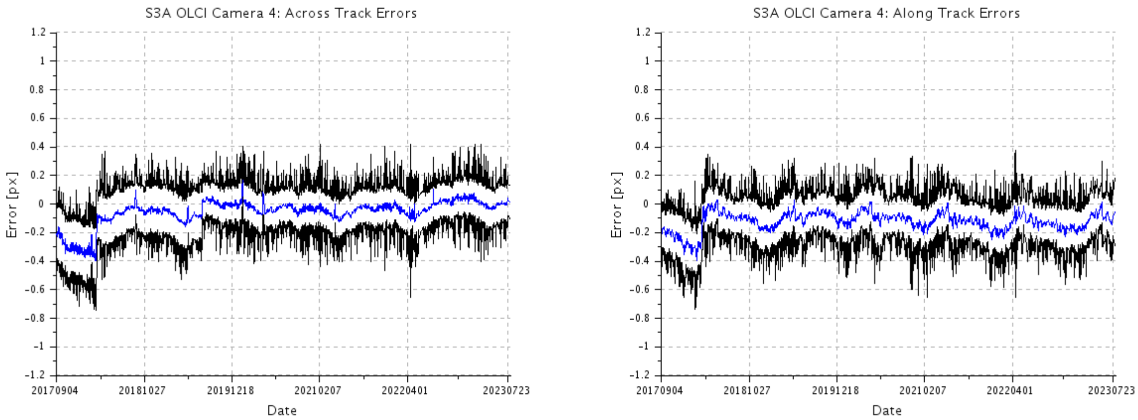

Figure 62: same as Figure 59 for Camera 4.

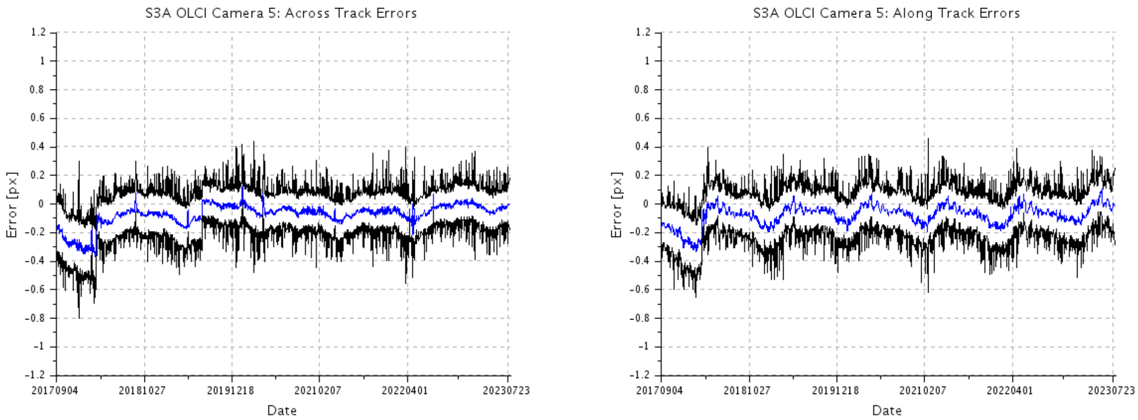

Figure 63: same as Figure 59 for Camera 5.

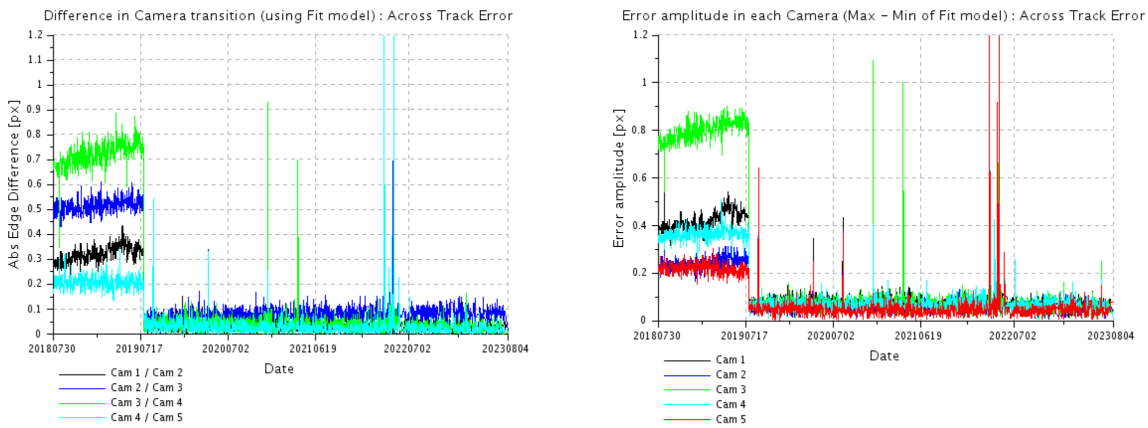

Figure 64: OLCI-A spatial across-track misregistration at each camera transition (left) and maximum amplitude of the across-track error within each camera (left).

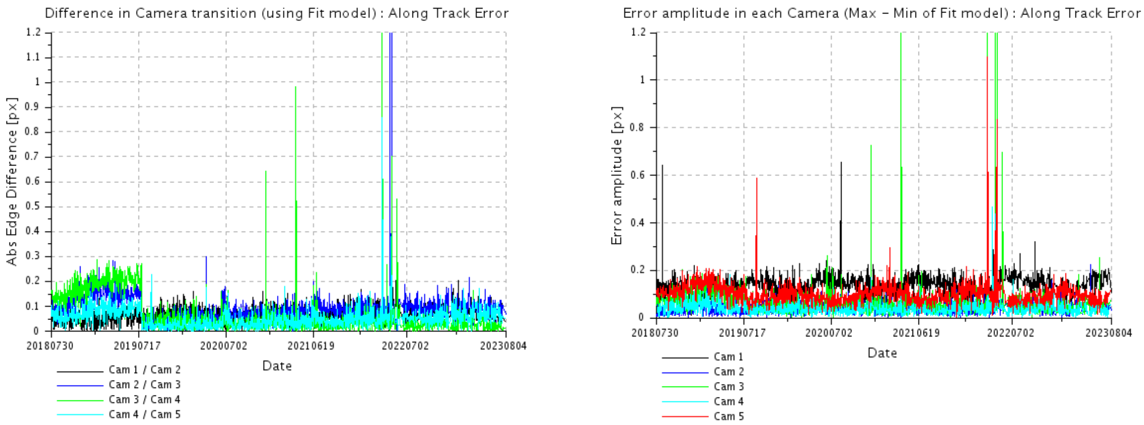

Figure 65: OLCI-A spatial along-track misregistration at each camera transition (left) and maximum amplitude of the along-track error within each camera (left).

2.5.2 OLCI-B

Georeferencing performance of OLCI-B improved significantly with the fourth geometric calibration introduced the 30/07/2019. However, the instrument pointing is still evolving, in particular for camera 2 (Figure 72) and a new geometric calibration has been done and introduced in the processing chain on the 16th of April 2020. Its impact is significant on the along-track biases of all cameras (Figure 67 to Figure 71), but also on the continuity at camera interfaces (Figure 72, left) and on intra-camera homogeneity (Figure 72, right). Since then, further adjustments to the geometric calibration have been introduced, mainly to correct the along-track drifts. The most recent was put in production on 29/07/2021 and its effect can be seen e.g. on left graphs of Figure 68, Figure 69 and Figure 71 (across-track biases of cameras 2, 3 & 5).

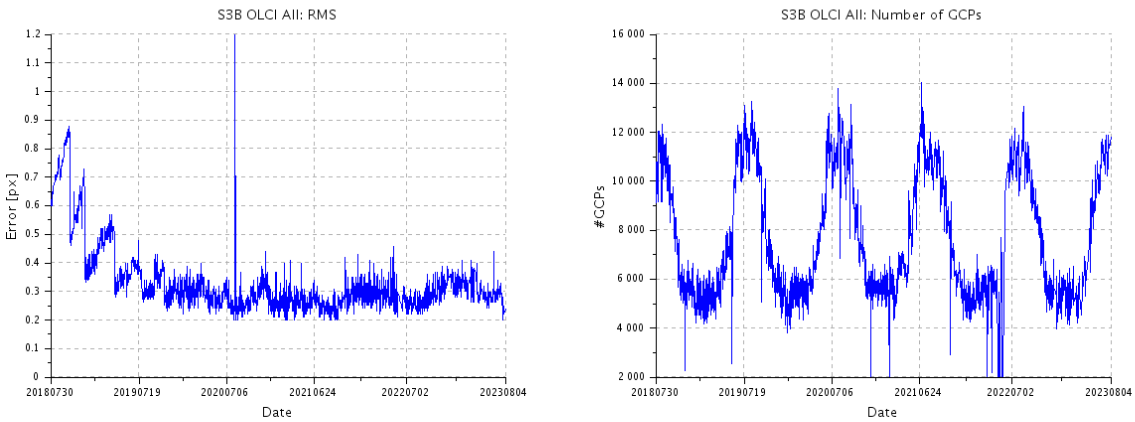

Figure 66: overall OLCI-B georeferencing RMS performance time series over the whole monitoring period (left) and corresponding number of validated control points (right)

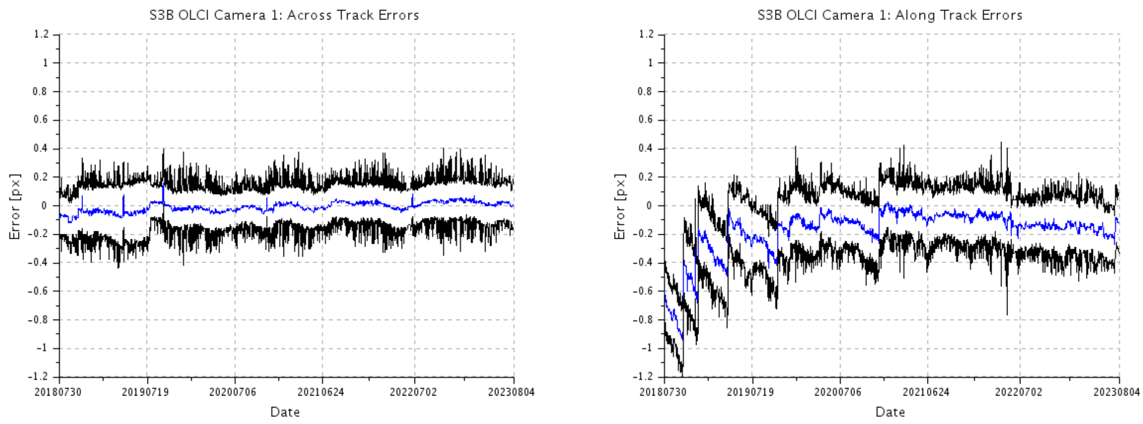

Figure 67: across-track (left) and along-track (right) OLCI-B georeferencing biases time series for Camera 1.

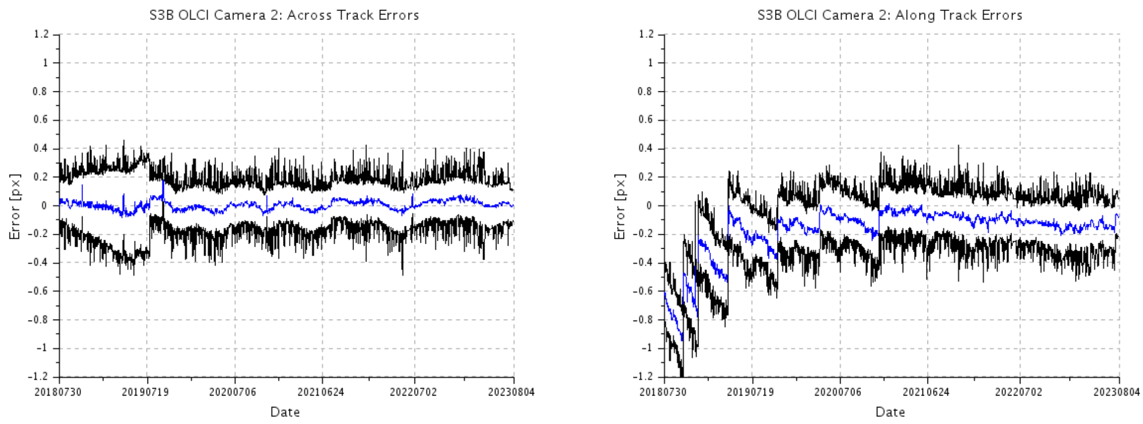

Figure 68: same as Figure 67 for Camera 2.

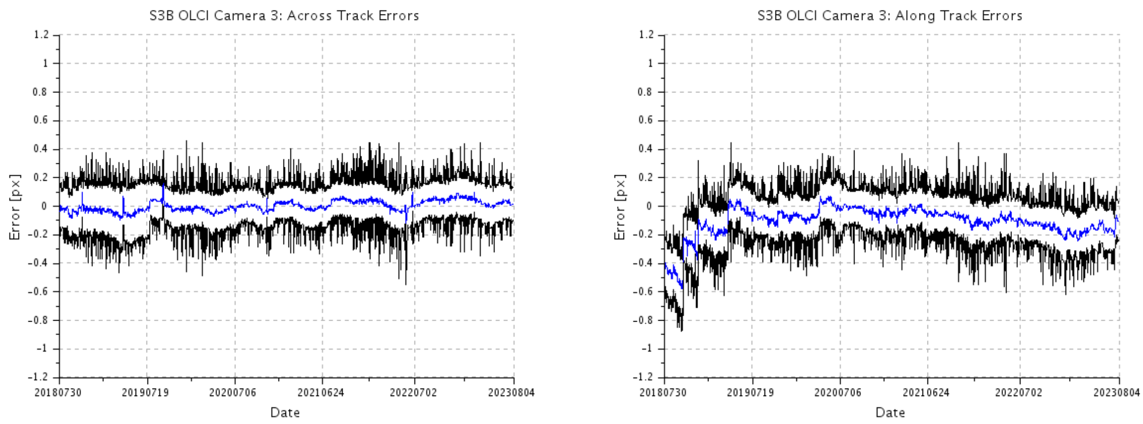

Figure 69: same as Figure 67 for Camera 3.

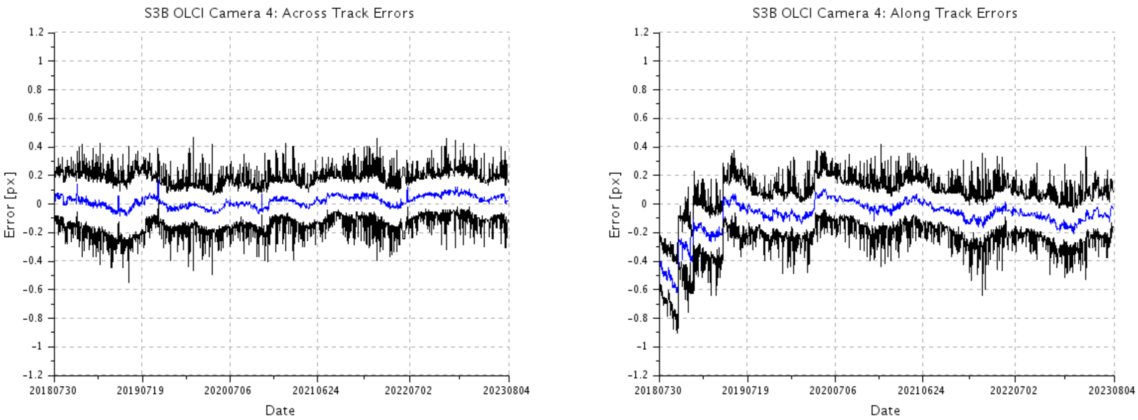

Figure 70: same as Figure 67 for Camera 4.

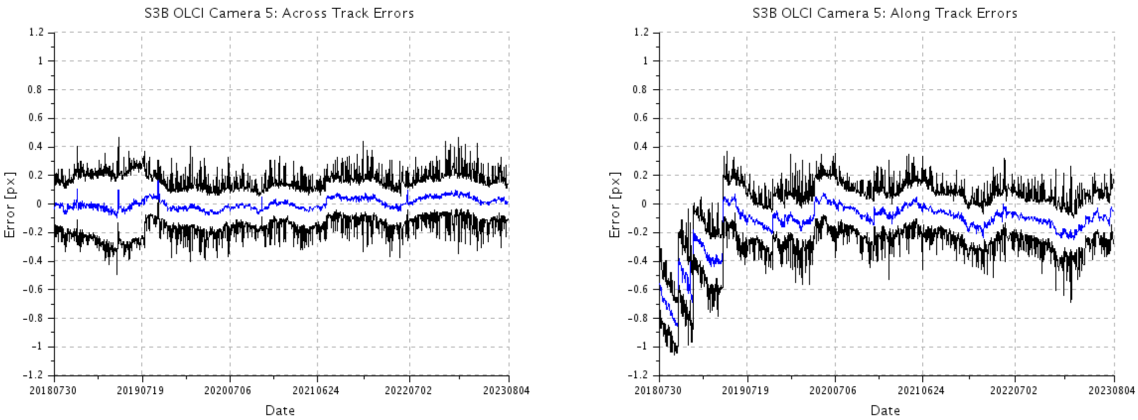

Figure 71: same as Figure 67 for Camera 5.

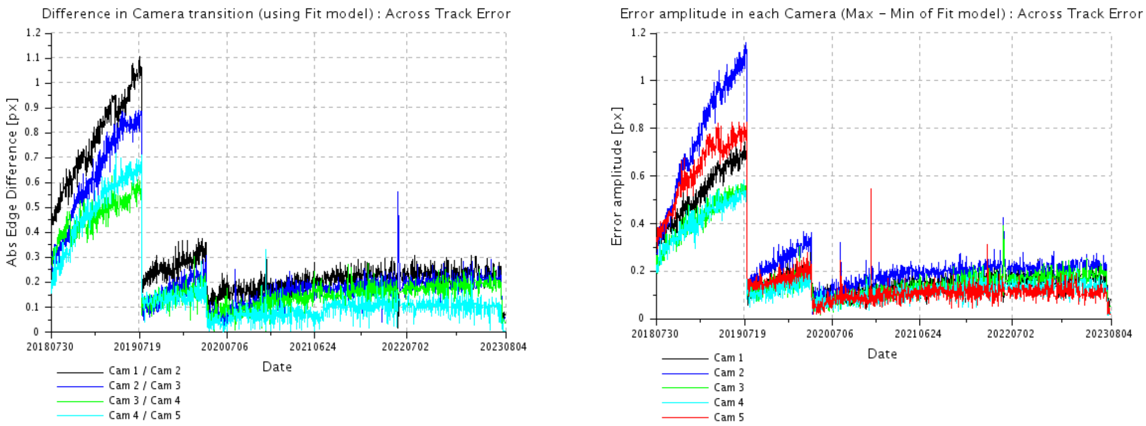

Figure 72: OLCI-B spatial across-track misregistration at each camera transition (left) and maximum amplitude of the across-track error within each camera (left).

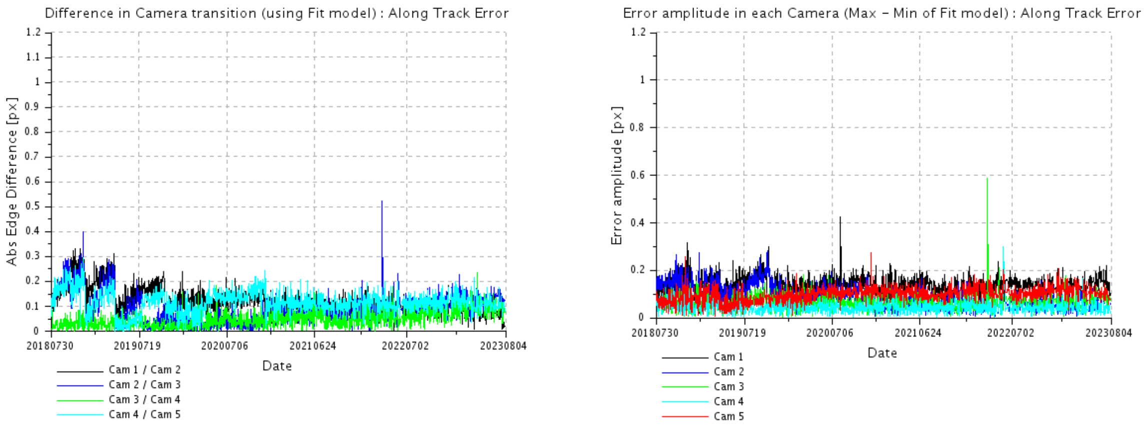

Figure 73: OLCI-B spatial along-track misregistration at each camera transition (left) and maximum amplitude of the along-track error within each camera (left).

3 OLCI Level 1 Product validation

3.1 [OLCI-L1B-CV-300], [OLCI-L1B-CV-310] – Radiometric Validation

3.1.1 S3ETRAC Service

Activities done

The S3ETRAC service extracts OLCI L1 RR and SLSTR L1 RBT data and computes associated statistics over 49 sites corresponding to different surface types (desert, snow, ocean maximizing Rayleigh signal, ocean maximizing sunglint scattering and deep convective clouds). The S3ETRAC products are used for the assessment and monitoring of the L1 radiometry (optical channels) by the ESLs.

All details about the S3ETRAC/OLCI and S3ETRAC/SLSTR statistics are provided on the S3ETRAC website http://s3etrac.acri.fr/index.php?action=generalstatistics.

- Number of OLCI products processed by the S3ETRAC service
- Statistics per type of target (DESERT, SNOW, RAYLEIGH, SUNGLINT and DCC)
- Statistics per sites
- Statistics on the number of records

For illustration, we provide below statistics on the number of S3ETRAC/OLCI records generated per type of targets (DESERT, SNOW, RAYLEIGH, SUNGLINT and DCC) for both OLCI-A (Figure 74) and OLCI-B (Figure 75).

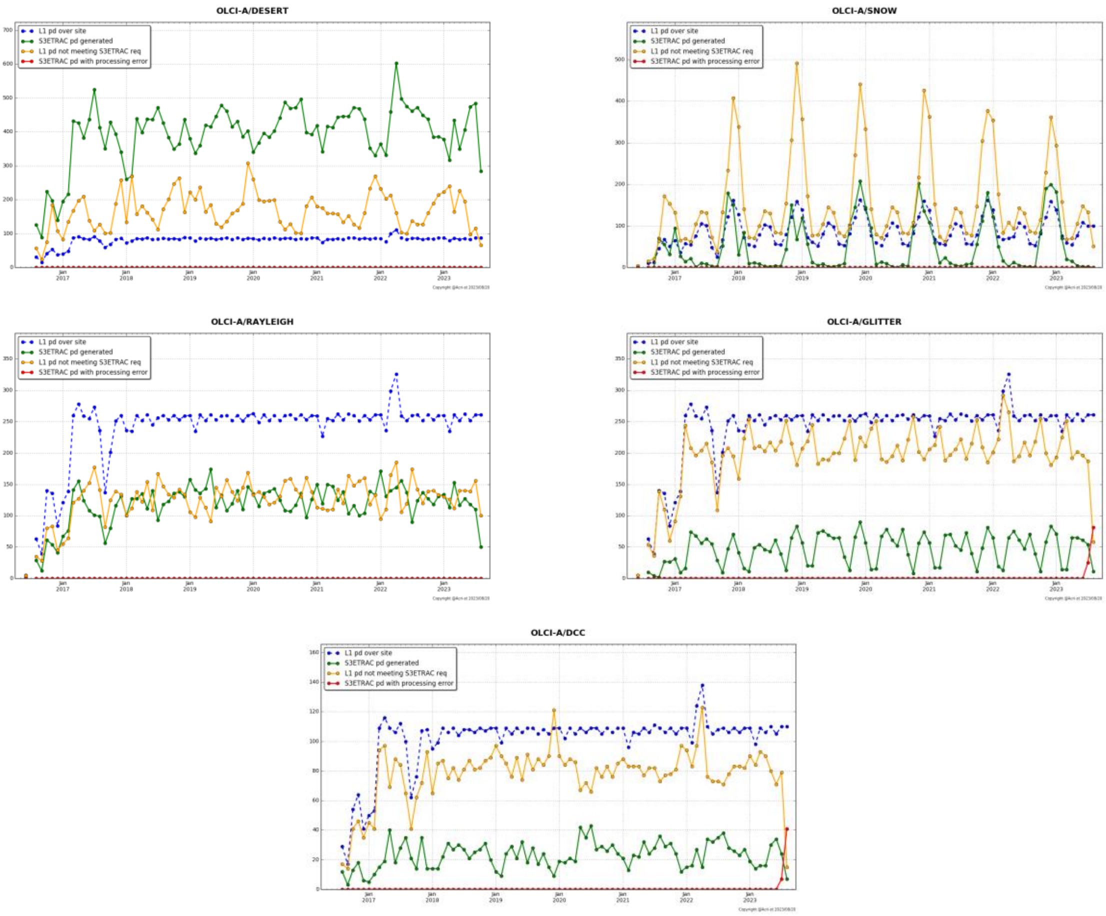

Figure 74: summary of S3ETRAC products generation for OLCI-A
(number of OLCI-A L1 products Ingested, blue – number of S3ETRAC extracted products generated, green – number of S3ETRAC runs without generation of output product (data not meeting selection requirements), yellow – number of runs ending in error, red, one plot per site type).

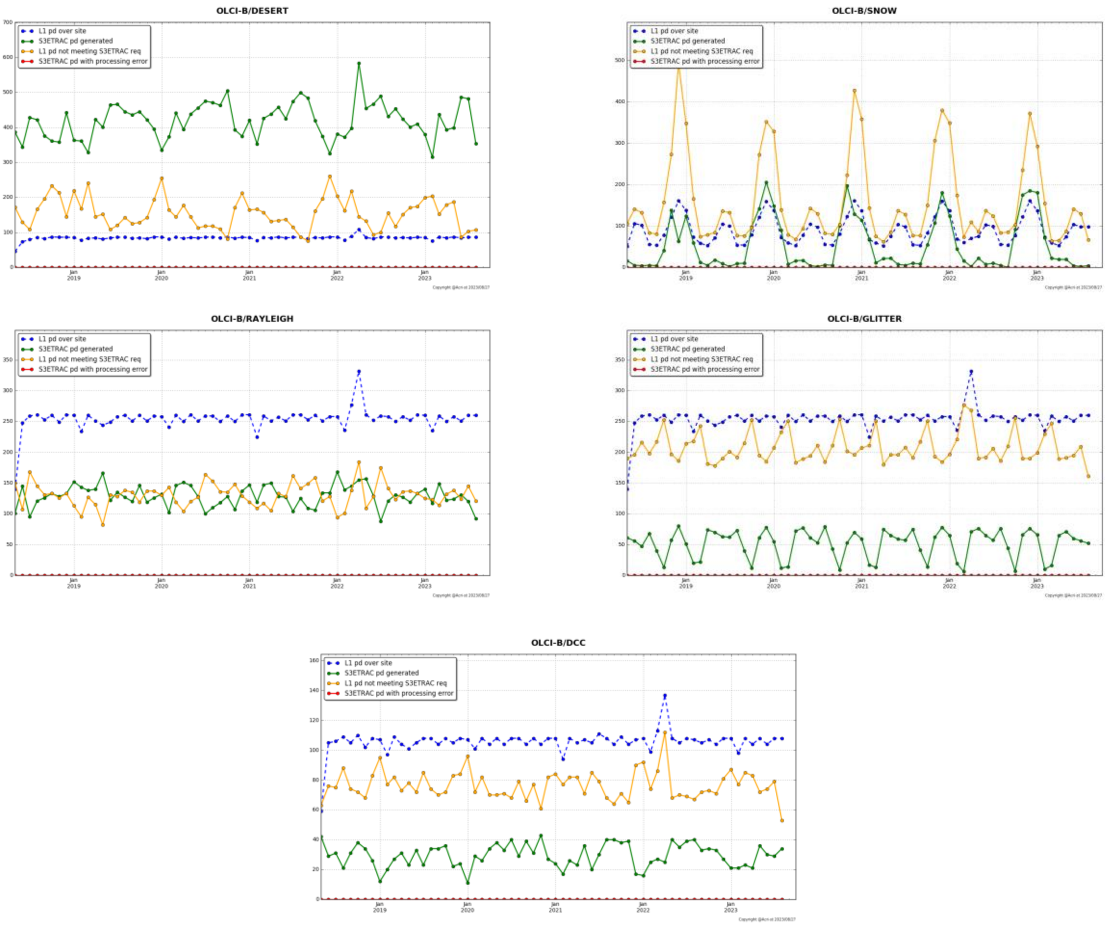

Figure 75: summary of S3ETRAC products generation for OLCI-B
(number of OLCI-B L1 products Ingested, yellow – number of S3ETRAC extracted products generated, blue – number of S3ETRAC runs without generation of output product (data not meeting selection requirements), green – number of runs ending in error, red, one plot per site type).

3.1.2 Radiometric validation with DIMITRI

OLCI-A and OLCI-B L1B radiometry verification has been processed as follow:

- The verification is performed over Ocean-sites and over Desert-sites **until the 30th of July 2023.**
- All results from OLCI-A and OLCI-B over Rayleigh, Glint and PICS are consistent with the previous reporting period over the used CalVal sites.
- Good stability of both sensors OLCI-A and OLCI-B could be observed, nevertheless the time-series average shows higher reflectance from OLCI-A.
- Bands with high gaseous absorption are excluded.

Verification and Validation over PICS

1. The ingestion of all the available L1B-LN1-NT products from OLCI-A and OLCI-B over the 6 desert CalVal-sites (Algeria3 & 5, Libya 1 & 4 and Mauritania 1 & 2) has been performed until the **30th of July 2023**.
2. The results are consistent over all the six used PICS sites (Figure 76 and Figure 77). Both sensors show a good stability over the analysed period.
3. The temporal average over the period **January 2022 - 30th of July 2023** of the elementary ratios (observed reflectance to the simulated one) for **OLCI-A** shows gain values between 2-4% over all the VNIR bands (Figure 78). Unlikely, the temporal average over the same period of the elementary ratios for **OLCI-B** shows gain values within 2% (mission requirements) over the VNIR spectral range (Figure 78). The spectral bands with significant absorption from water vapor and O_2 (Oa11, Oa13, Oa14, Oa15 and Oa20) are excluded.

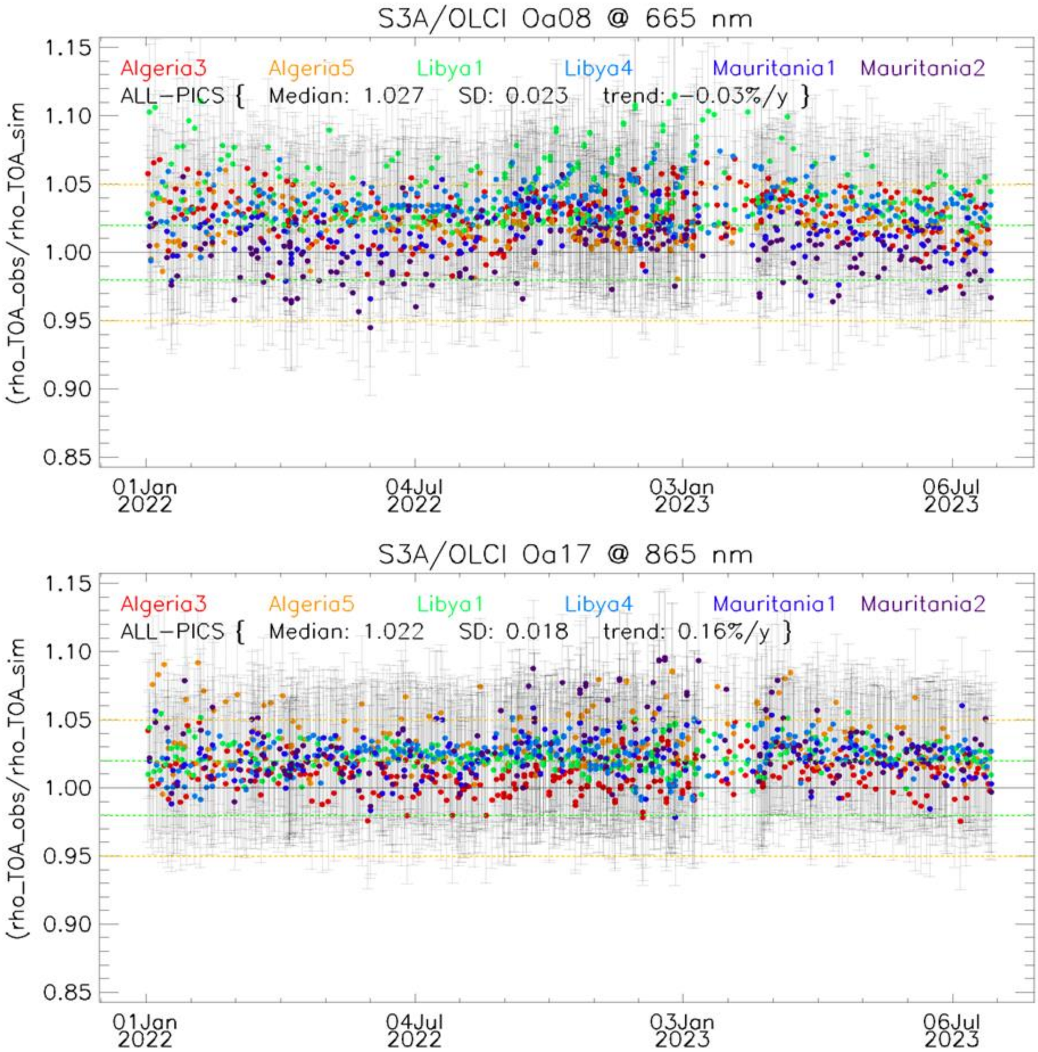

Figure 76: Time-series of the elementary ratios (observed/simulated) signal from OLCI-A for (top to bottom) bands Oa03 and Oa17 respectively over January 2022- June 2023 from the six PICS Cal/Val sites. Dashed-green and orange lines indicate the 2% and 5% respectively. Error bars indicate the desert methodology uncertainty.

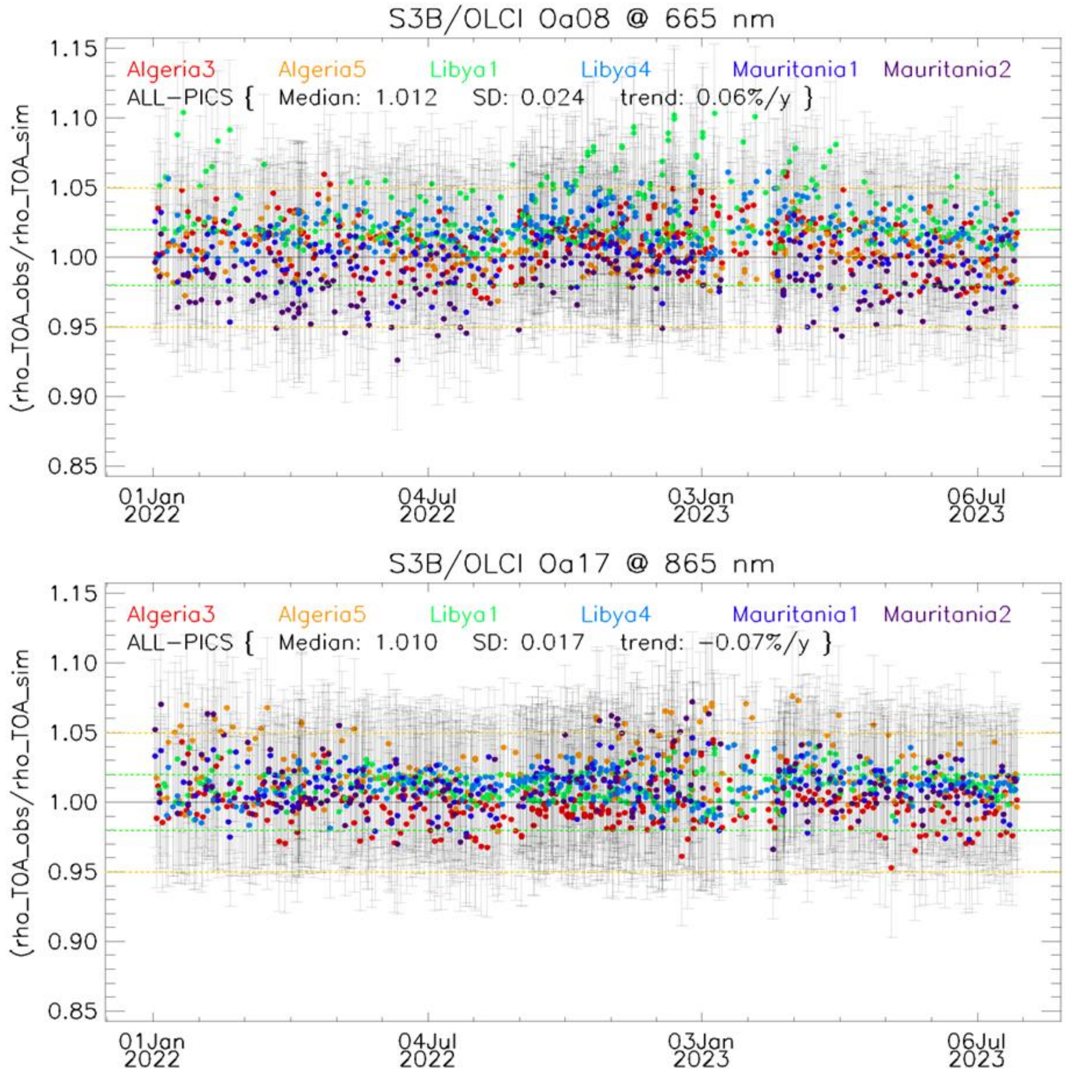

Figure 77: Time-series of the elementary ratios (observed/simulated) signal from OLCI-B for (top to bottom) bands Oa08 and Oa17 respectively over January 2022- June 2023 from the six PICS Cal/Val sites. Dashed-green and orange lines indicate the 2% and 5% respectively. Error bars indicate the desert methodology uncertainty.

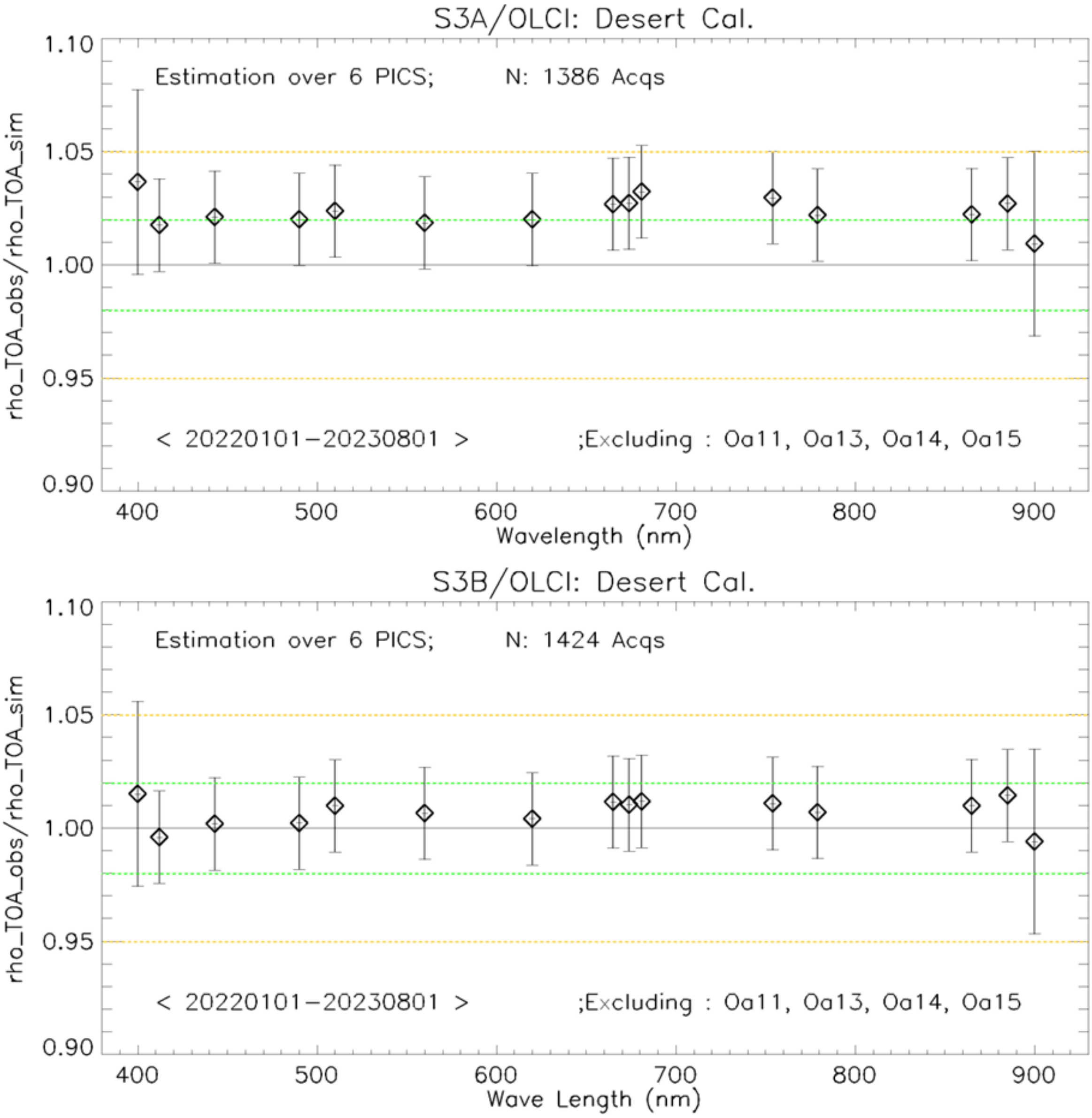

Figure 78: The estimated gain values for OLCI-A and OLCI-B over the 6 PICS sites identified by CEOS over the period January 2022- May 2023 as a function of wavelength. Dashed-green and orange lines indicate the 2% and 5% respectively. Error bars indicate the desert methodology uncertainty.

Validation over Rayleigh

Rayleigh method has been performed from the available mini-files over the period **January 2022- End July 2023** for OLCI-A and OLCI-B. The results were produced with the configuration (ROI-AVERAGE). The gain coefficients of OLCI-A are consistent with the previous results. Bands Oa01-Oa05 display biases values between 3%-5% while bands Oa06-Oa09 exhibit biases about 2%, just within the mission requirement (Figure 79). The gain coefficients of OLCI-B are lower than OLCI-A ones, where bands Oa01-Oa05 display biases values about 2-5%, when bands Oa6-Oa9 exhibit biases within the 2% mission requirement (Figure 79).

Validation over Glint and synthesis

Glint calibration method has been performed over the period **January 2022- end July 2023** for OLCI-A and OLCI-B. The outcome of this analysis shows a good consistency with the desert and Rayleigh outputs over the NIR spectral range Oa06-Oa09 for both sensors. Glint results from OLCI-A show that the NIR bands are within 3% (slightly above the 2% mission requirements), except Oa21 which shows higher biases more than ~5% for both sensors (see Figure 79). Again, the glint gain from OLCI-B looks slightly lower than OLCI-A one with most bands within the 2% mission requirement if ignoring the Rayleigh results in the blue-green region.

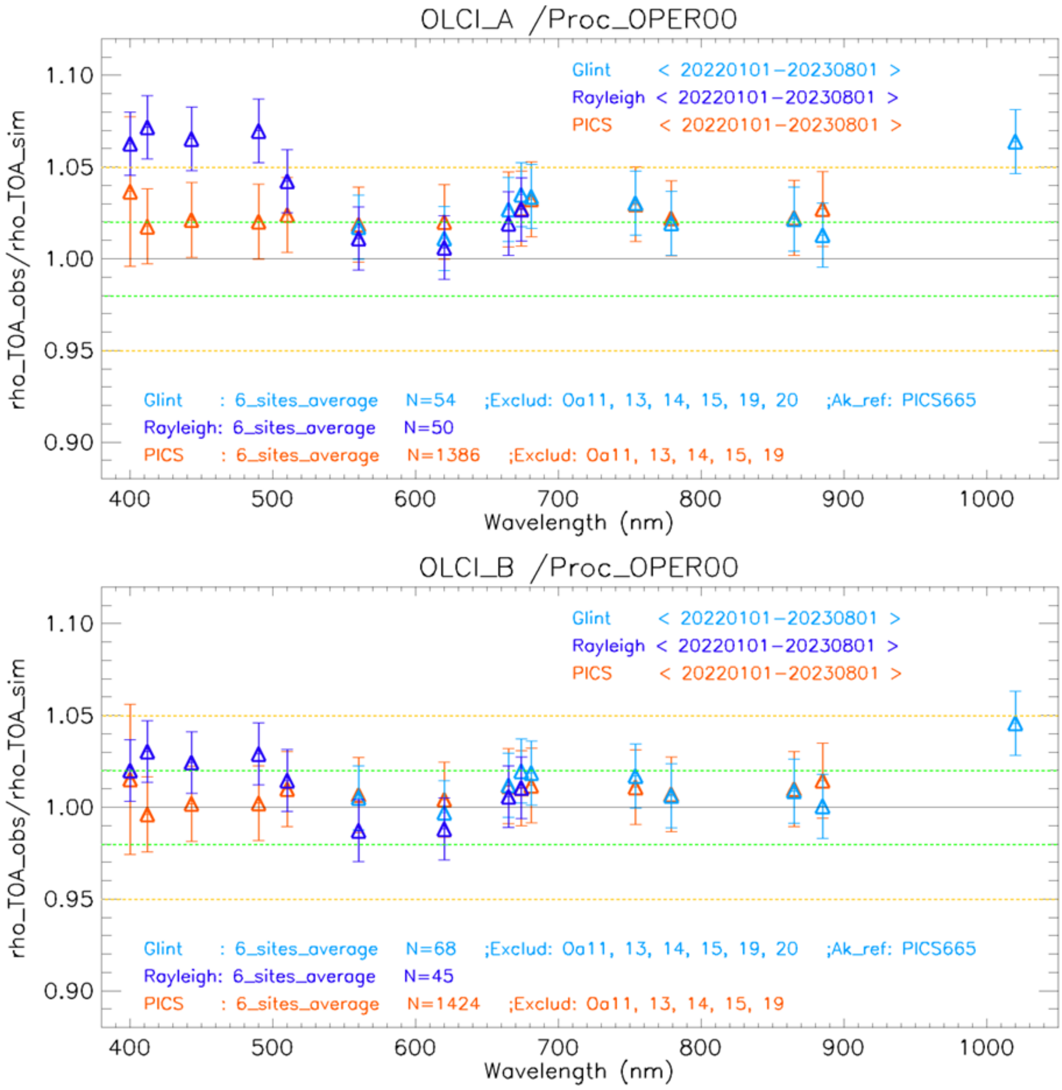

Figure 79: The estimated gain values for OLCI-A and OLCI-B from Glint, Rayleigh and PICS methods over the period January 2022- End June 2023 as a function of wavelength. We use the gain value of Oa8 from PICS-Desert method as reference gain for Glint method. Dashed-green and orange lines indicate the 2% and 5% respectively. Error bars indicate the method uncertainties.

Cross-mission Intercomparison over PICS:

X-mission Intercomparison between MERIS, MSI-A, MSI-B, OLCI-A, OLCI-B, SLSTR-A and SLSTR-B has been performed over the 6 PICS-test-sites.

Figure 80 shows the estimated gain over different time-series for different sensors over PICS. The spectral bands with significant absorption from water vapor and O2 are excluded. OLCI-A seems to have higher gain wrt the other sensors (except SLSTR-A/B), and of about 1-3% higher gain wrt to OLCI-B over VNIR spectral range.

y

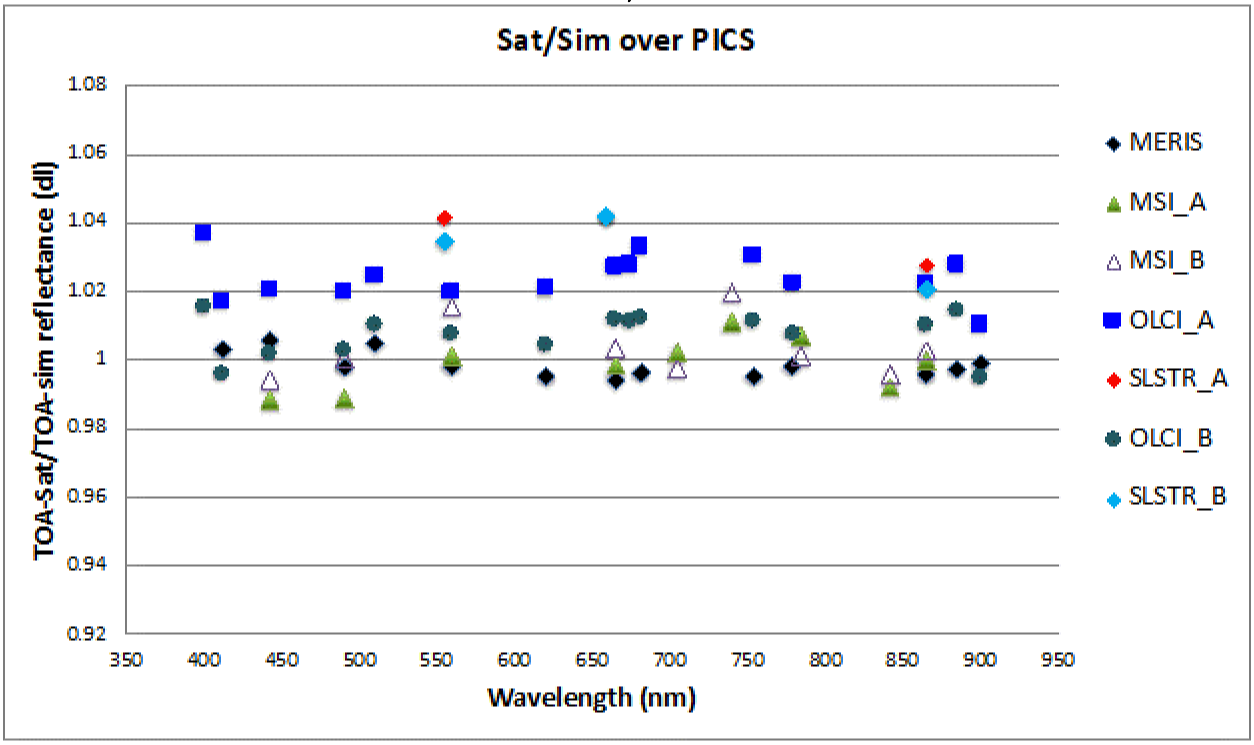

Figure 80: Ratio of observed TOA reflectance to simulated one for (black) MERIS, (pale-green) S2A/MSI, (white) S2B/MSI, (blue) S3A/OLCI, (green) S3B/OLCI, (red) S3A/SLSTR-NADIR, and (cyan) S3B/SLSTR-NADIR averaged over the six PICS test sites over different periods as a function of wavelength.

3.1.3 Radiometric validation with OSCAR

OSCAR Rayleigh results

The OSCAR Rayleigh have been applied to the S3A and S3B S3ETRAC data from the 6 oceanic calibration sites (Table 3) using a new chlorophyll climatology which has been derived from the CMEMS OLCI monthly CHL products from considering the years 2017, 2018 and 2019.

Table 3: S3ETRAC Rayleigh Calibration sites

Site Name	Ocean	North Latitude	South Latitude	East Longitude	West Longitude
PacSE	South-East of Pacific	-20.7	-44.9	-89	-130.2
PacNW	North-West of Pacific	22.7	10	165.6	139.5
PacN	North of Pacific	23.5	15	200.6	179.4
AtlN	North of Atlantic	27	17	-44.2	-62.5
AtlS	South of Atlantic	-9.9	-19.9	-11	-32.3
IndS	South of Indian	-21.2	-29.9	100.1	89.5

In Figure 81 the average OSCAR OLCI-A and OLCI-B Rayleigh results are given for July 2023. In Figure 82 and Table 4, the same results are given for all acquisitions of 2023.

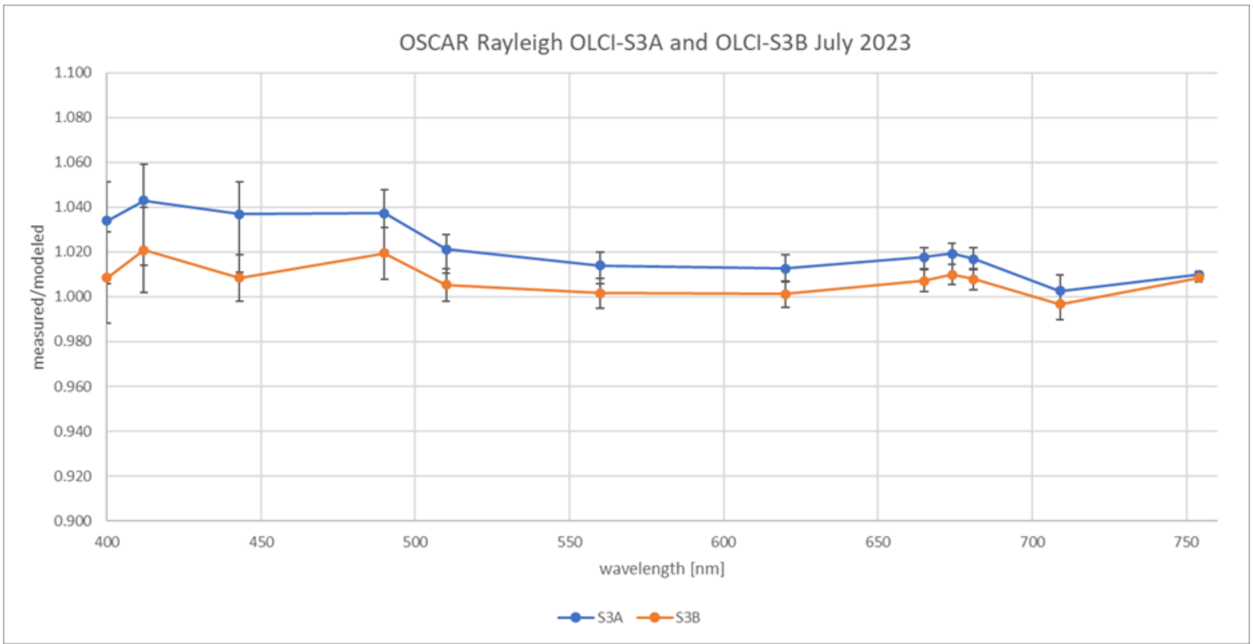

Figure 81: OSCAR Rayleigh S3A and S3B Calibration results as a function of wavelength for June 2023. The results are obtained with a new climatology derived from CMEMS OLCI monthly CHL products.

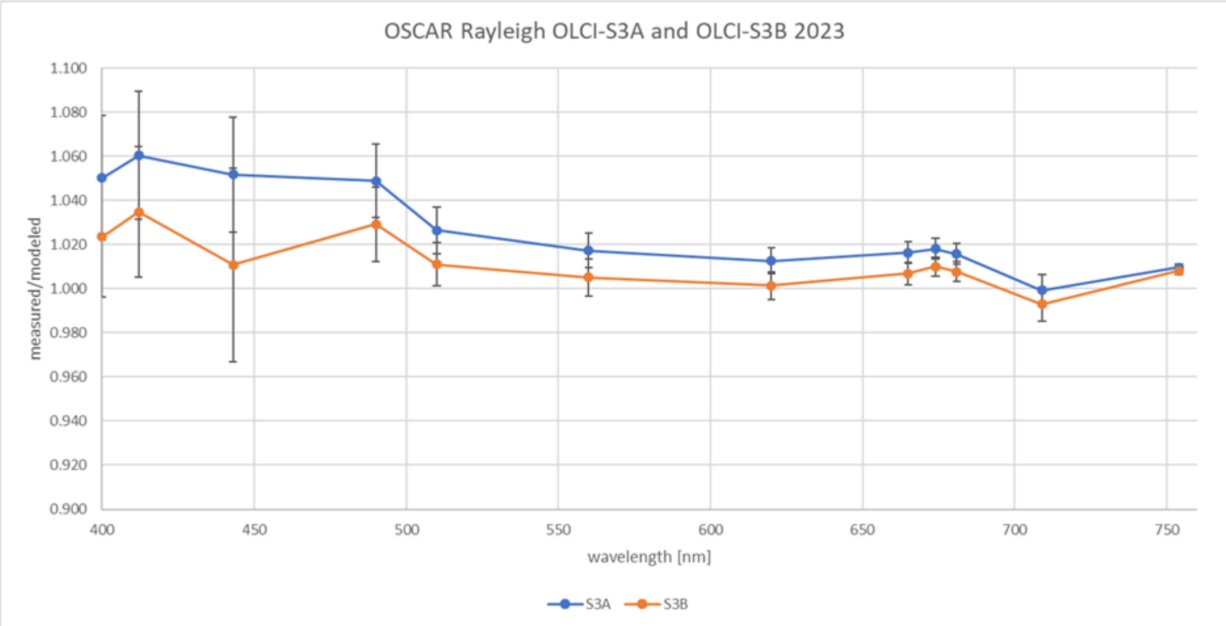

Figure 82: OSCAR Rayleigh OLCI-A and OLCI-B Calibration results as a function of wavelength for all acquisitions of 2023. The results are obtained with a new climatology derived from CMEMS OLCI monthly CHL products.

Table 4. OSCAR Rayleigh calibration results for S3A and S3B (average and standard deviation over all 2023 acquisitions) over all scenes currently (re)processed with the new climatology and observed difference (in %) between OLCIA and OLCIB

OLCI band	Wavelength	Oscar Rayleigh OLCIA		Oscar Rayleigh OLCIB		% difference OLCIA and OLCIB
	(nm)	avg	stdev	avg	stdev	
Oa01	400	1.050	0.028	1.024	0.027	2.54%
Oa02	412	1.060	0.029	1.035	0.030	2.41%
Oa03	443	1.052	0.026	1.011	0.044	3.89%
Oa04	490	1.049	0.017	1.029	0.017	1.88%
Oa05	510	1.026	0.011	1.011	0.010	1.51%
Oa06	560	1.017	0.008	1.005	0.008	1.20%
Oa07	620	1.013	0.006	1.001	0.006	1.10%
Oa08	665	1.016	0.005	1.007	0.005	0.93%
Oa09	674	1.018	0.005	1.010	0.004	0.80%
Oa10	681	1.016	0.005	1.008	0.004	0.79%
Oa11	709	0.999	0.007	0.993	0.008	0.62%
Oa12	754	1.010	0.001	1.008	0.002	0.16%

OSCAR Glitter results

The OSCAR Glitter have been applied to all S3ETRAC glitter data for June 2023. Both OLCI-A and OLCI-B data was processed. The plots in Figure 83 are the glitter results for OLCI-A and OLCI-B for the period of

July 2023 and on Figure 84 for all results of 2023 (also provided in Table 5). The values are in absolute terms, since all bands are referenced to the Rayleigh result of band Oa8. The glitter method is a relative inter-band calibration method, since the Oa8 band is used to estimate windspeed. By multiplying all band results with the Rayleigh calibration factor for the same period, the results are referenced to the results of this method.

For all results of 2023, the difference between OLCI-A and OLCI-B (Table 5, in %) is below 1% for all bands, except for bands Oa04 and Oa05. It also indicates a brighter OLCI-A compared to OLCI-B.

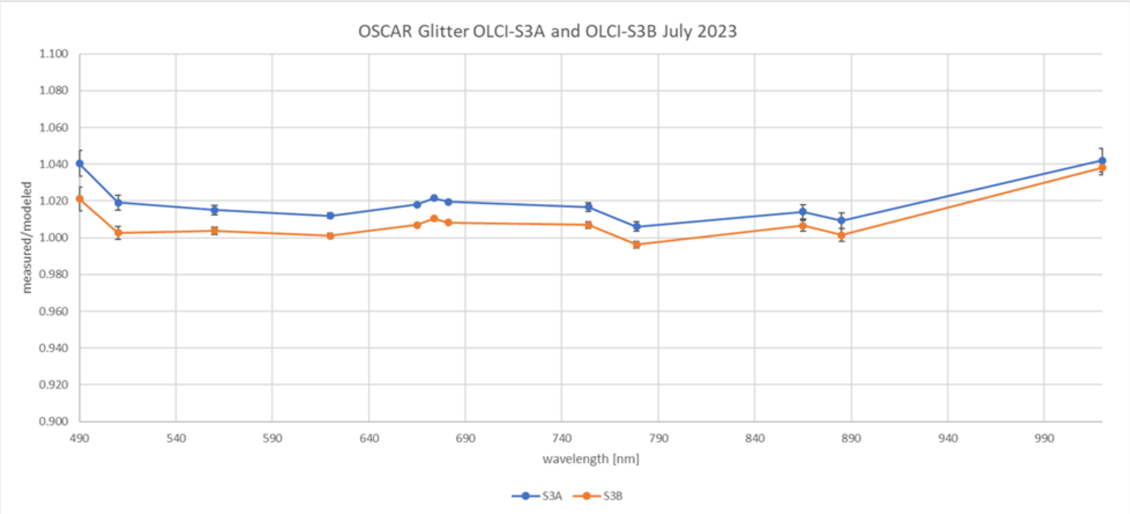

Figure 83: OSCAR Glitter OLCI-A & OLCI-B Calibration results as a function of wavelength for June 2023. The results are obtained with a new climatology derived from CMEMS OLCI monthly CHL products.

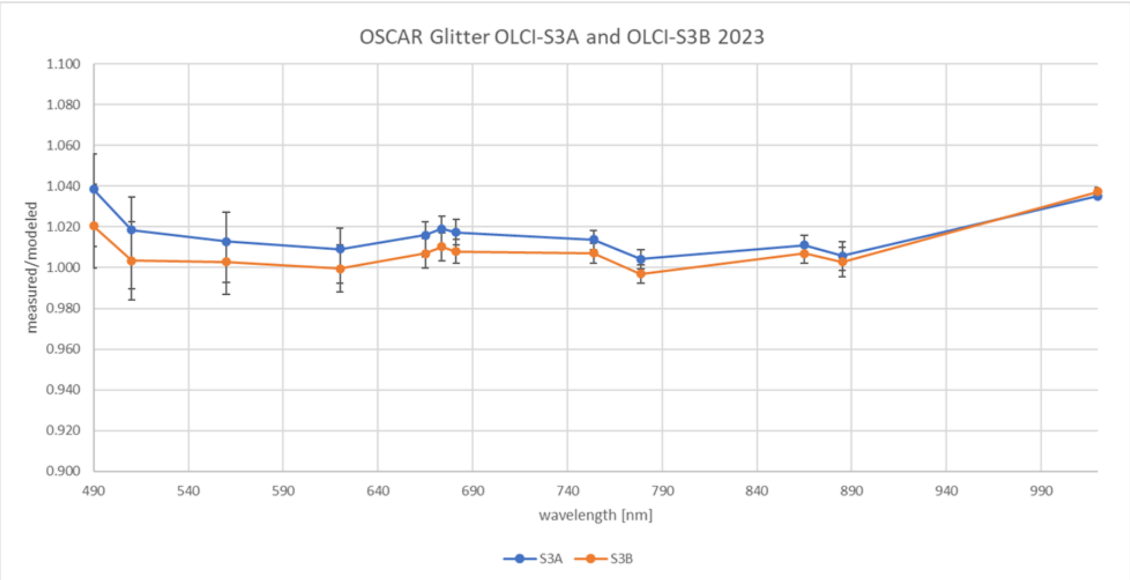

Figure 84: OSCAR Glitter OLCI-A & OLCI-B Calibration results as a function of wavelength for all acquisitions of 2023. The results are obtained with a new climatology derived from CMEMS OLCI monthly CHL products.

Table 5: OSCAR Glitter calibration results for OLCI-A and OLCI-B (average and standard deviation over all acquisitions of 2023) currently processed with the new climatology and observed difference (in %)

OLCI band	Wavelength (nm)	Oscar Glitter OLCIA avg	Oscar Glitter OLCIA stdev	Oscar Glitter OLCIB avg	Oscar Glitter OLCIB stdev	% difference OLCIA and OLCIB
Oa04	490	1.039	0.007	1.020	0.006	1.74%
Oa05	510	1.018	0.005	1.003	0.004	1.49%
Oa06	560	1.013	0.003	1.003	0.003	0.99%
Oa07	620	1.009	0.002	1.000	0.002	0.94%
Oa08	665	1.016	0.000	1.007	0.000	0.89%
Oa09	673.75	1.019	0.001	1.010	0.001	0.88%
Oa10	681.25	1.017	0.001	1.008	0.001	0.91%
Oa12	753.75	1.014	0.005	1.007	0.003	0.66%
Oa16	778.75	1.039	0.007	1.020	0.006	1.74%
Oa17	865	1.018	0.005	1.003	0.004	1.49%
Oa18	885	1.013	0.003	1.003	0.003	0.99%
Oa21	1020	1.009	0.002	1.000	0.002	0.94%

3.1.4 Radiometric validation with Moon observations: LIME results

There has been no new result during the reporting period. The last figures (reported in OLCI Data Quality Report covering June 2023) are considered valid.

4 Level 2 Land products validation

4.1 [OLCI-L2LRF-CV-300]

4.1.1 Routine extractions

- The focus for this time period has been on the rolling archive Non Time Critical (NT) data until the 31st of July 2023. More data available for statistical analysis as a concatenation procedure for all available data in the MERMAID processing has been implemented.
- Concatenated time series of OLCI Global Vegetation Index and OLCI Terrestrial Chlorophyll Index have been regenerated on the current rolling archive availability including previous extractions since June 2016 and April 2018 for S3A and S3B respectively.

4.1.1.1 OLCI-A

Figure 85 to Figure 94 below present the Core Land Sites OLCI-A time series over the current period.

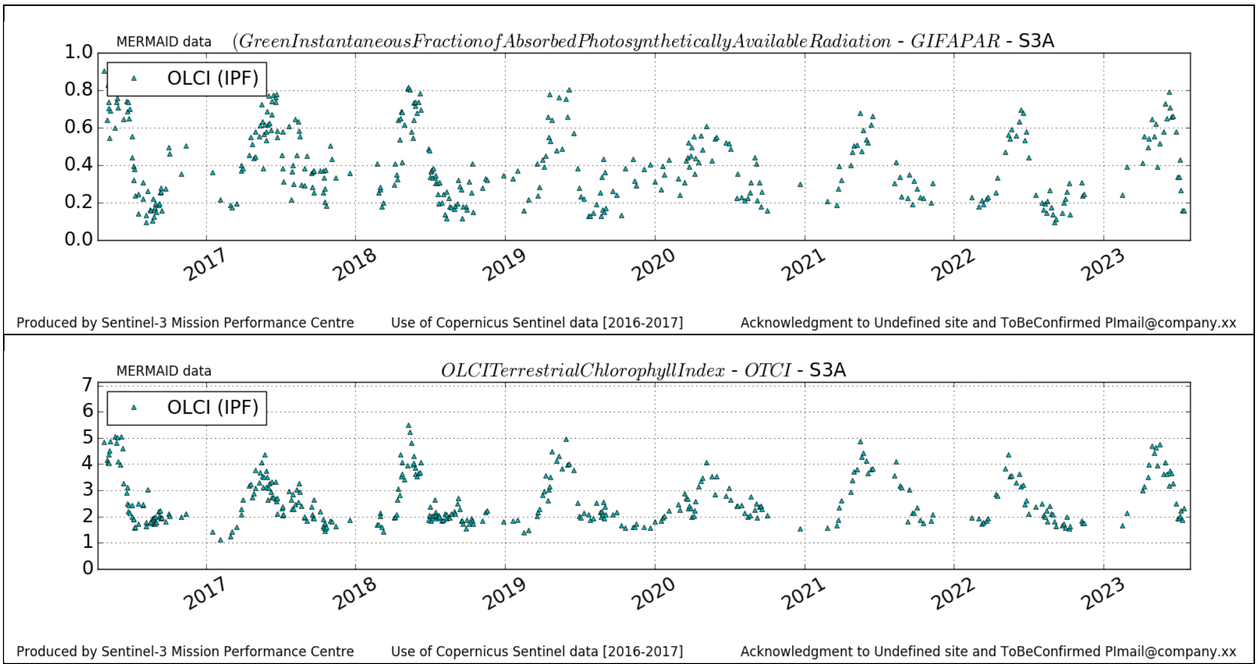

Figure 85: DeGeb time series over current report period

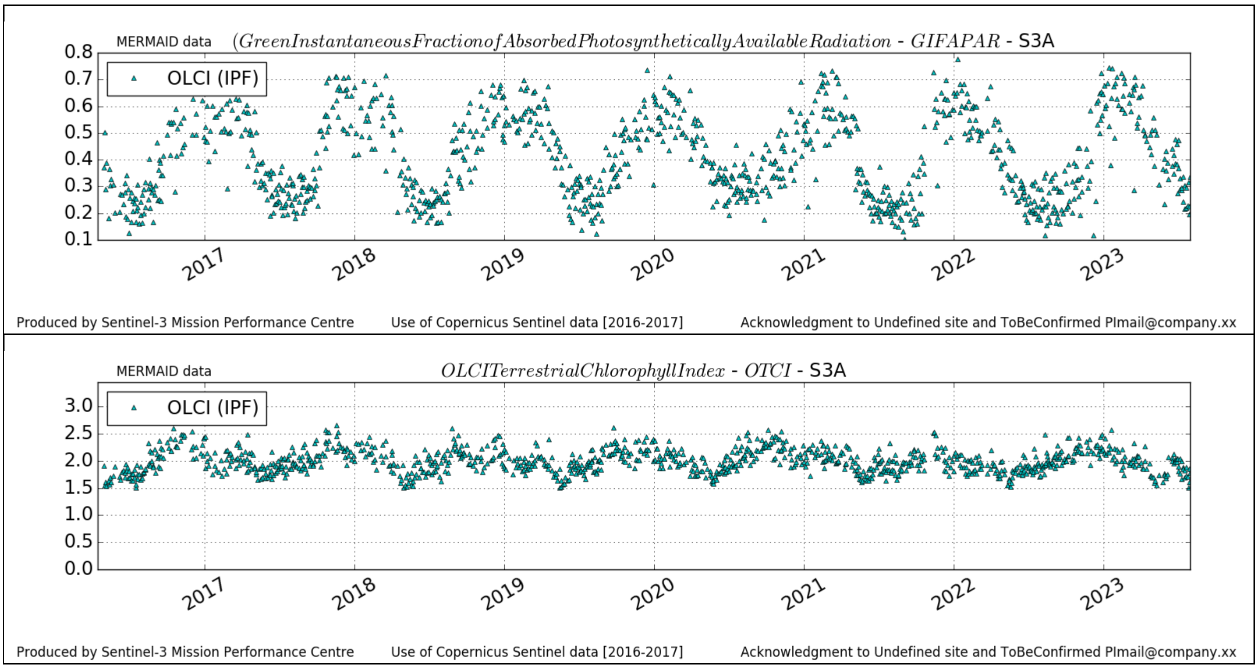

Figure 86: ITCat time series over current report period

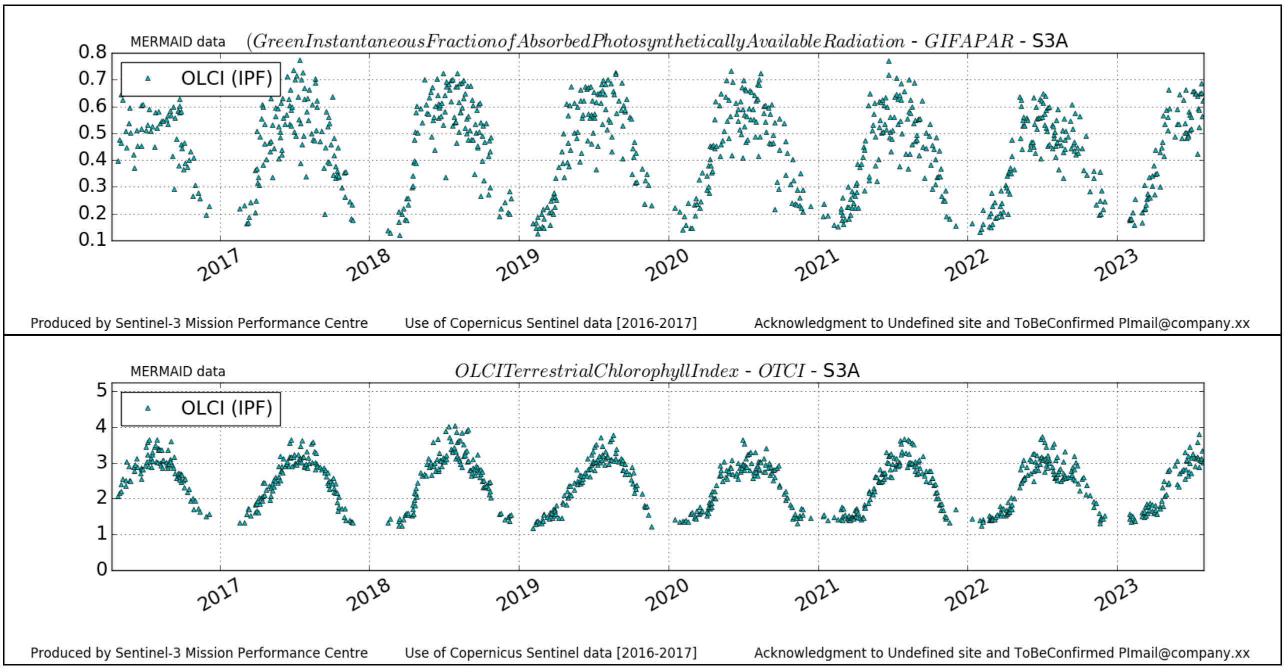

Figure 87: ITIsp time series over current report period

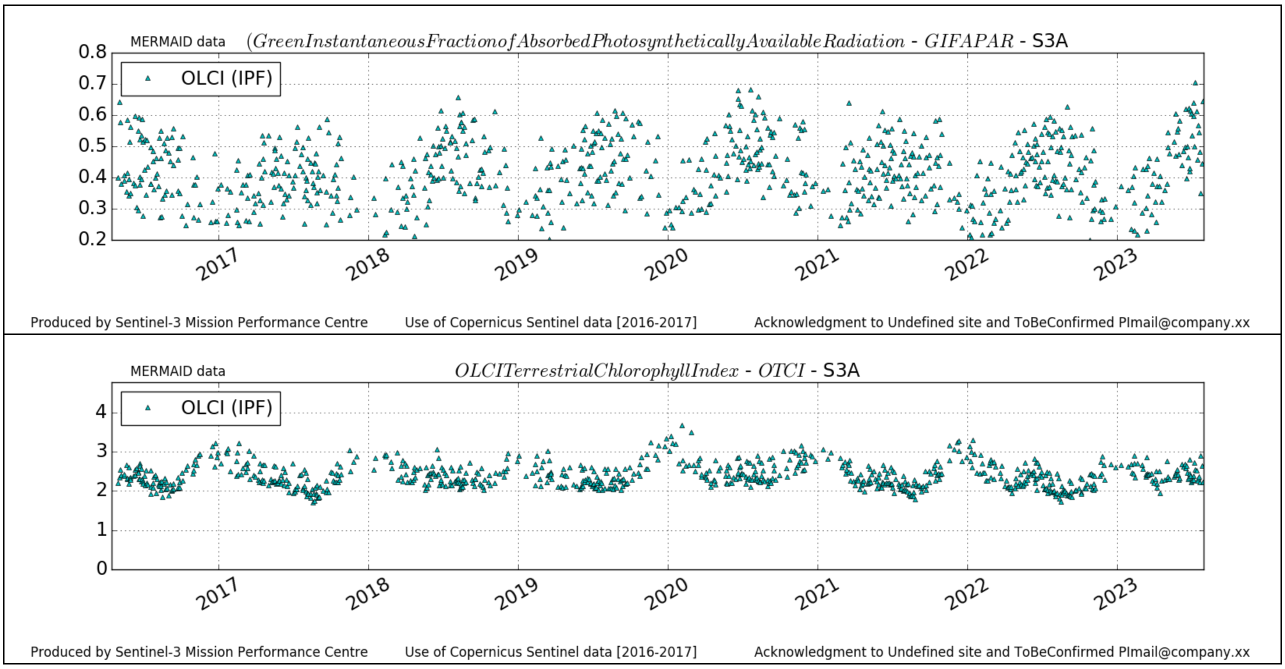

Figure 88: ITSro time series over current report period

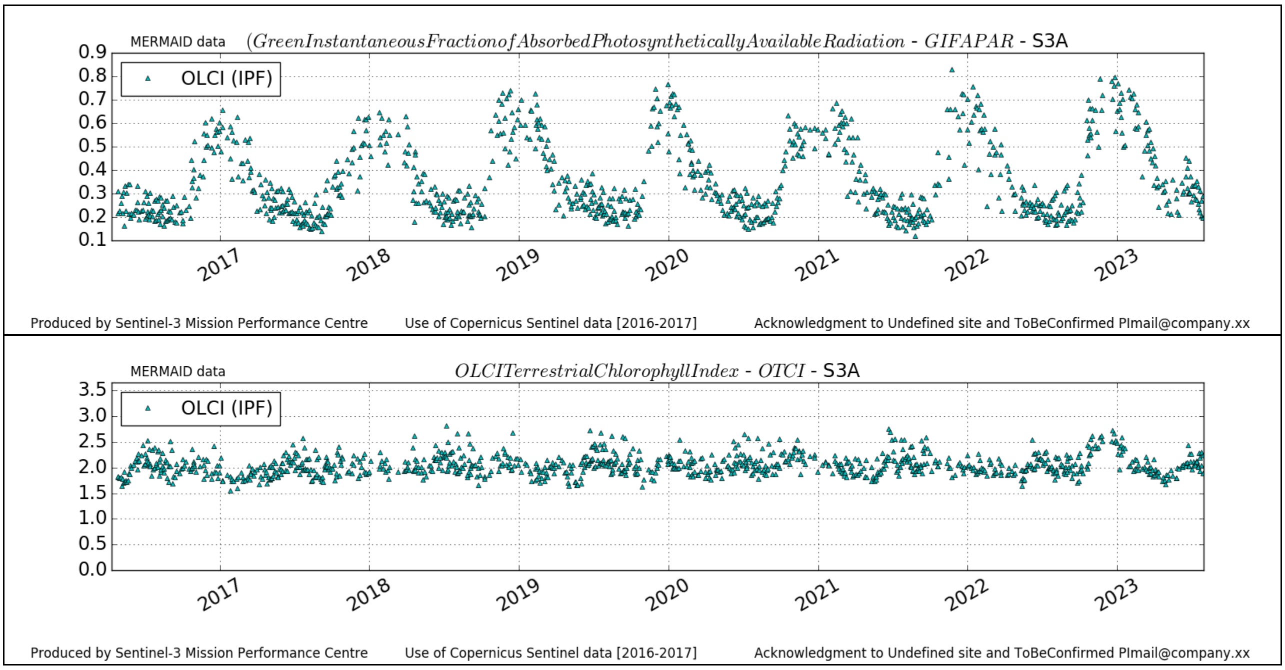

Figure 89: ITTra time series over current report period

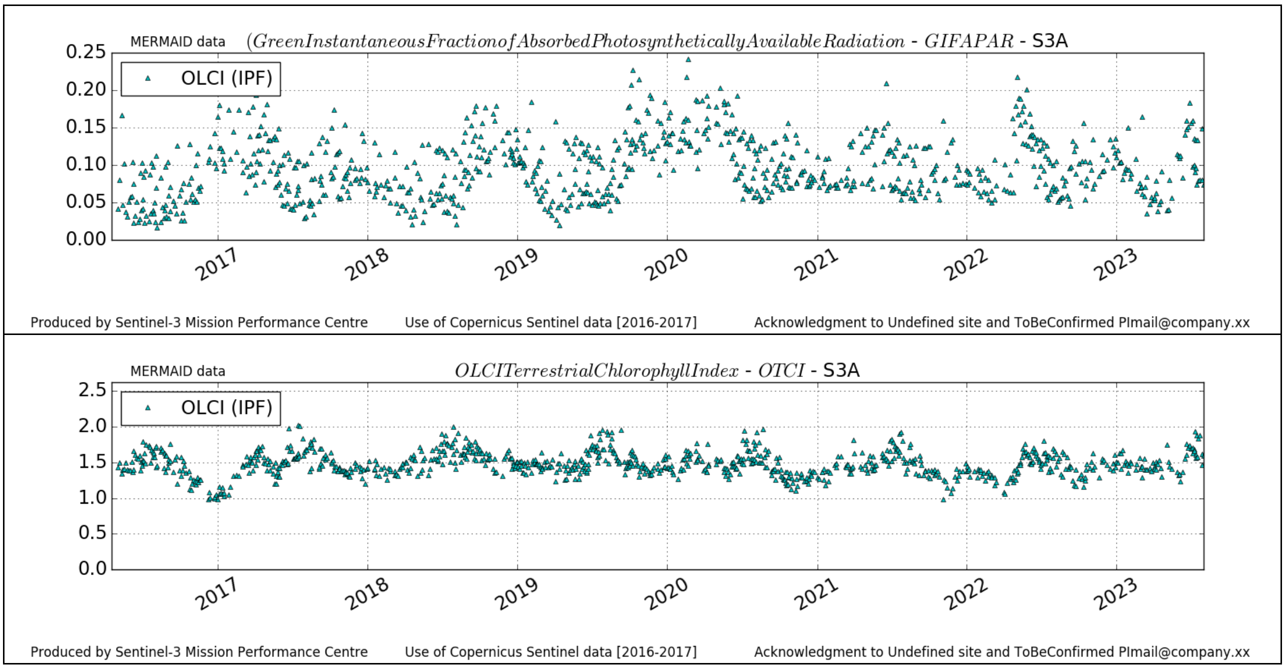

Figure 90: SPAli time series over current report period

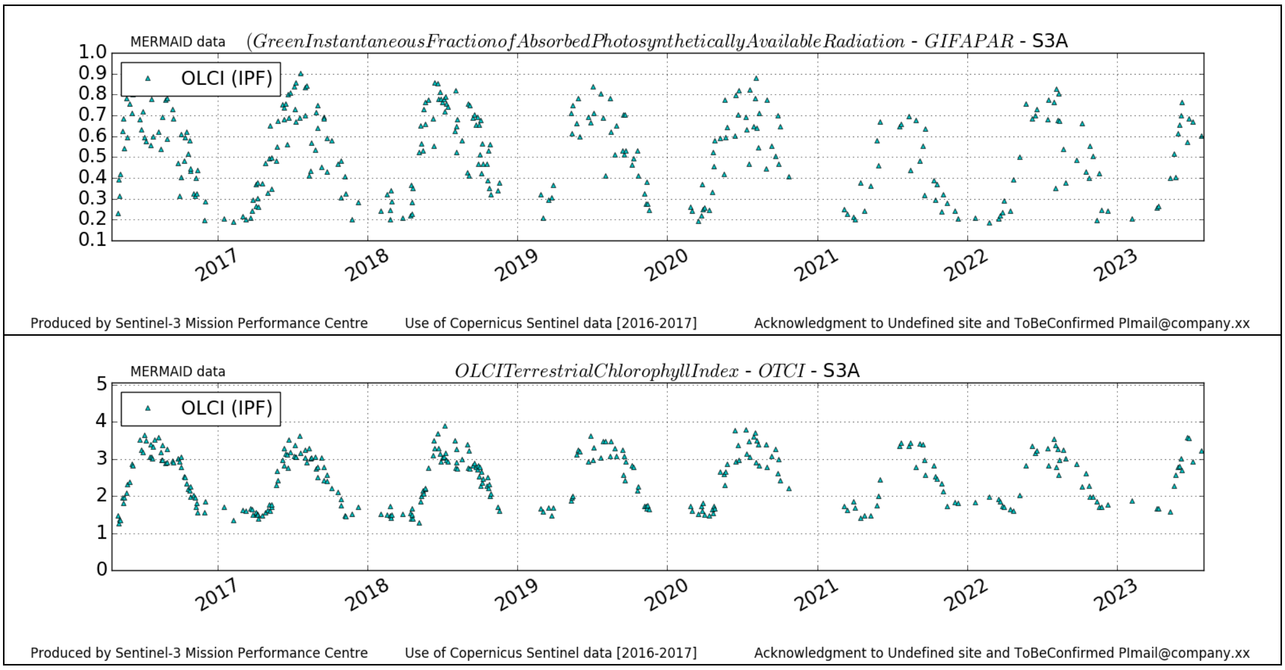

Figure 91: UKNFo time series over current report period

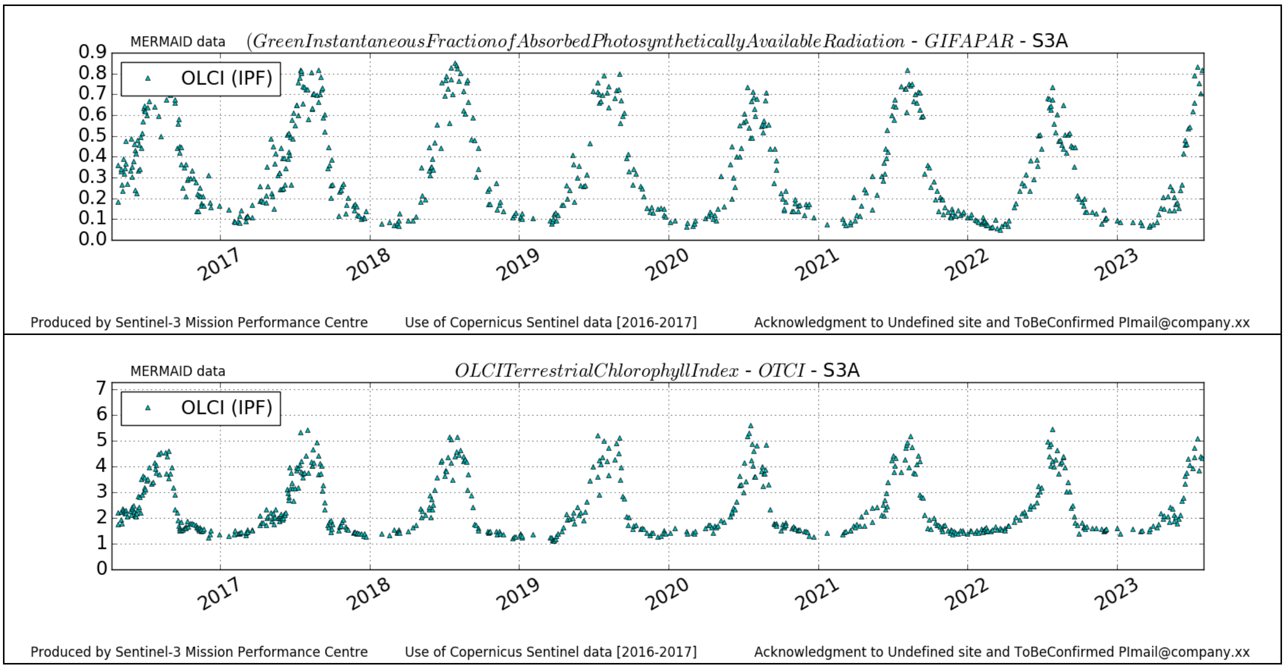

Figure 92: USNe1 time series over current report period

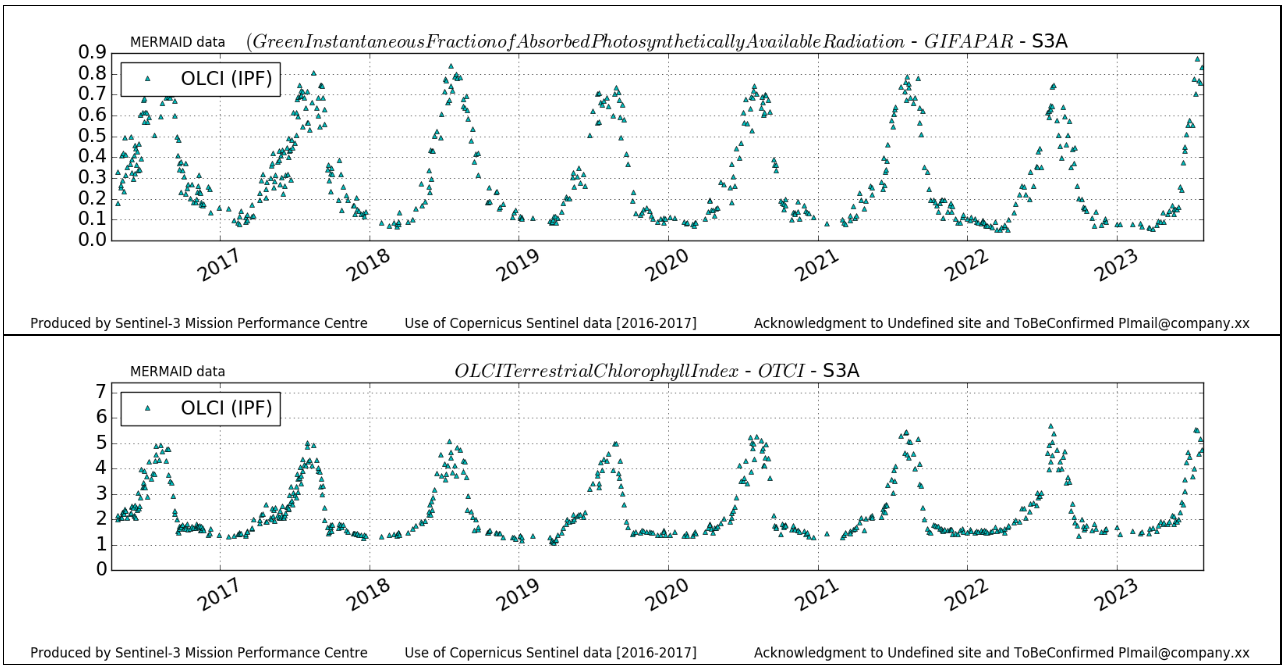

Figure 93: USNe2 time series over current report period

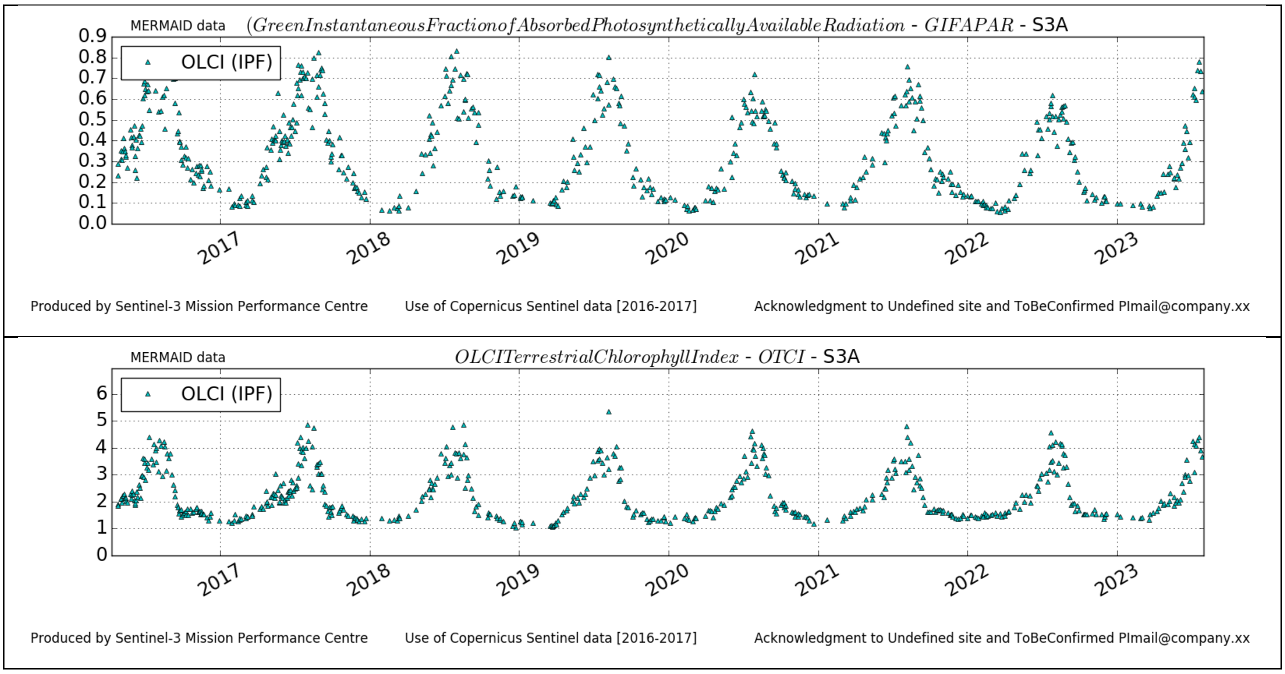

Figure 94: USNe3 time series over current report period

4.1.1.2 OLCI-B

Figure 95 to Figure 104 below present the Core Land Sites OLCI-B time series over the current period.

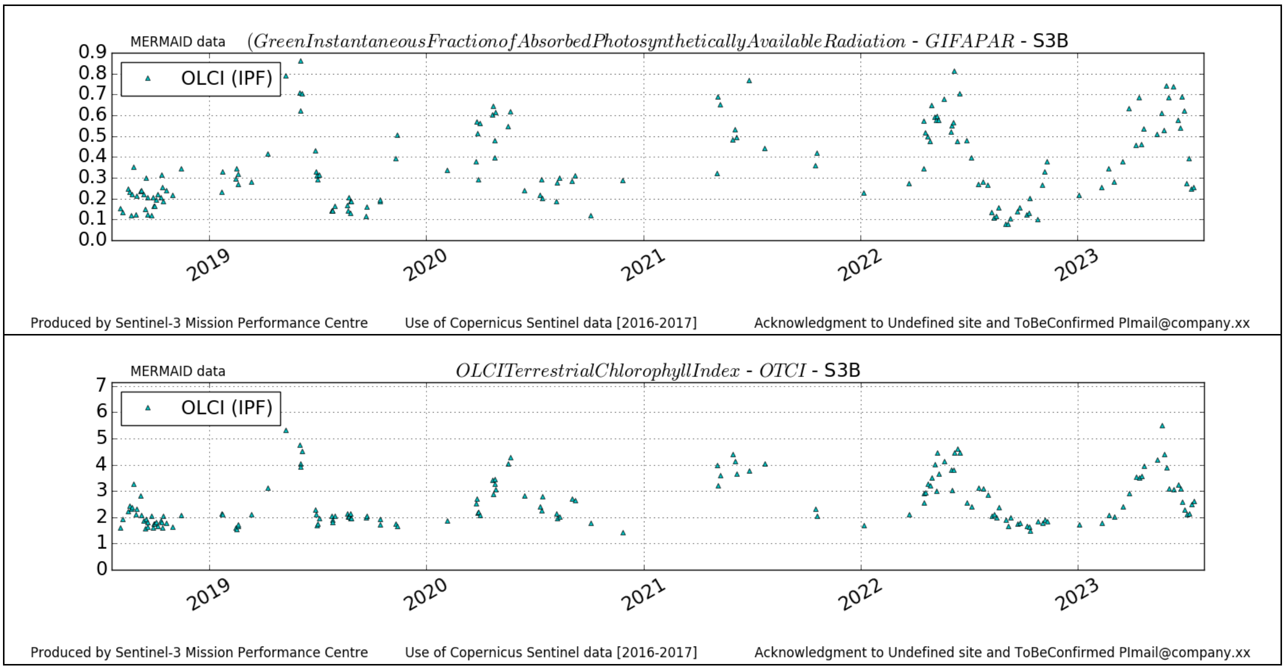

Figure 95: DeGeb time series over current report period

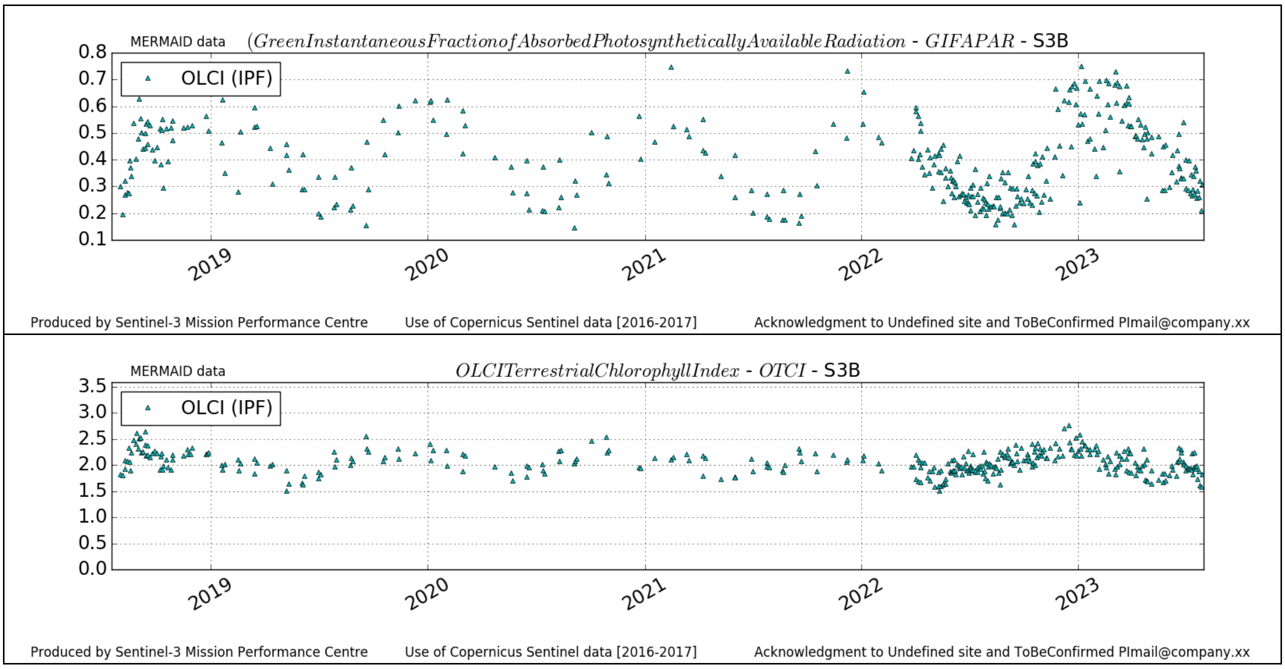

Figure 96: ITCat time series over current report period

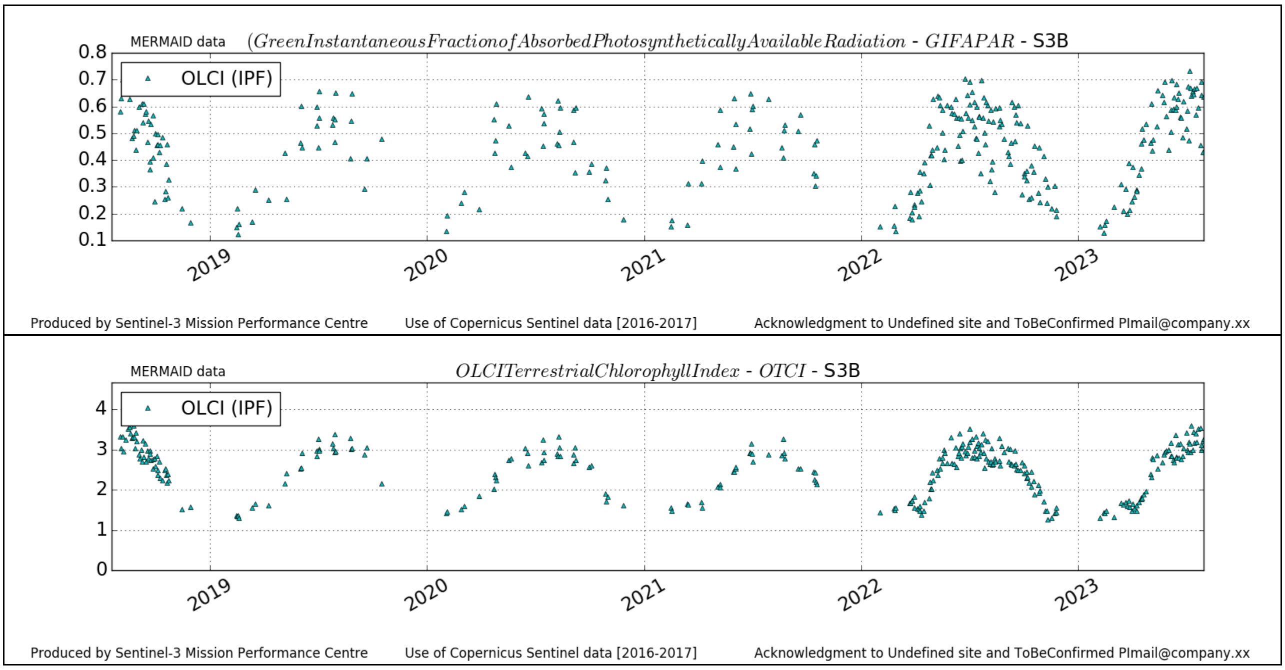

Figure 97: ITIsp time series over current report period

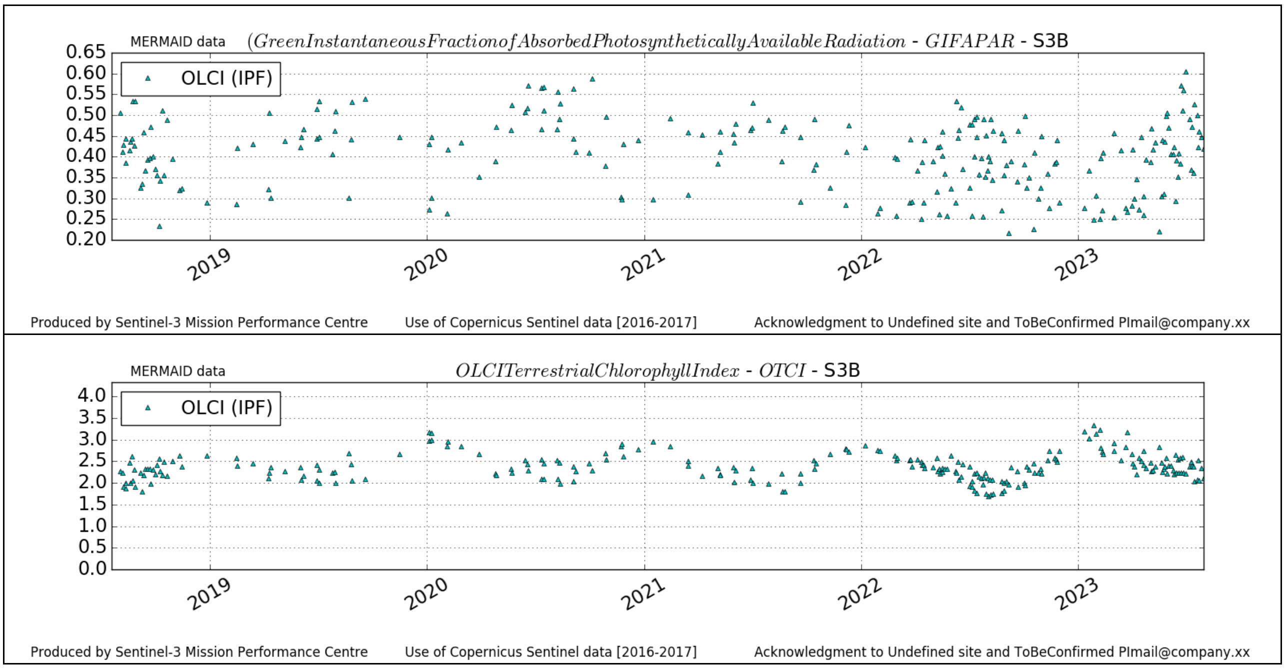

Figure 98: ITSro time series over current report period

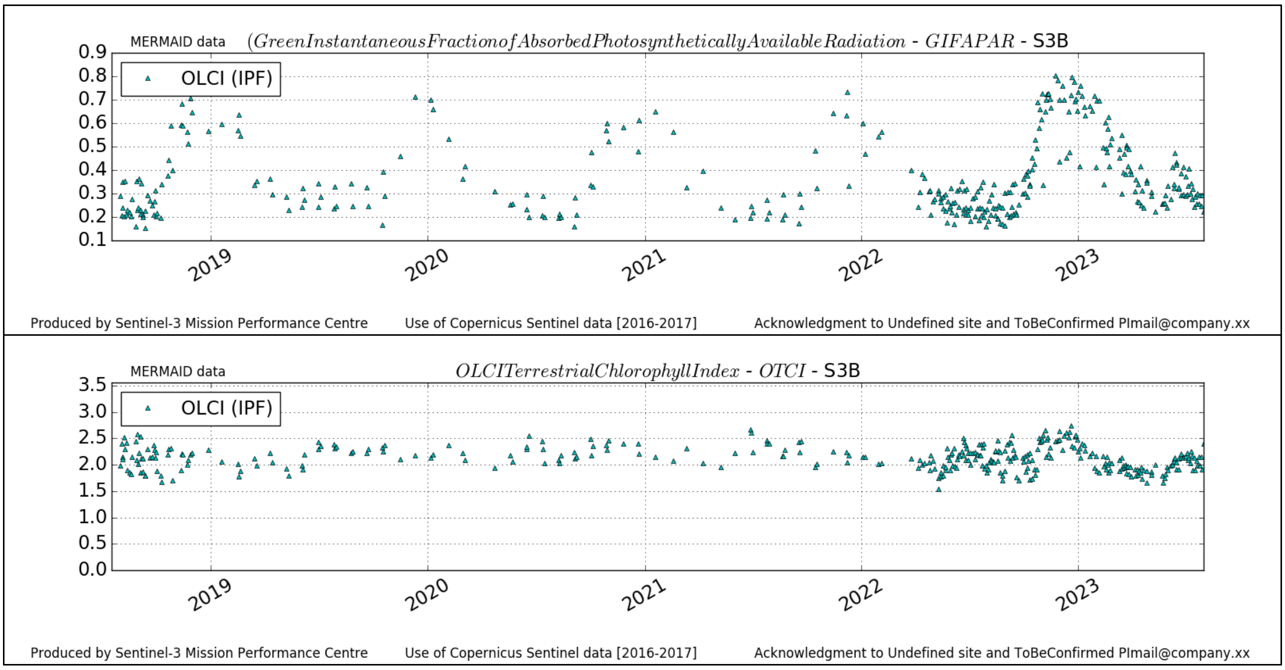

Figure 99: ITTra time series over current report period

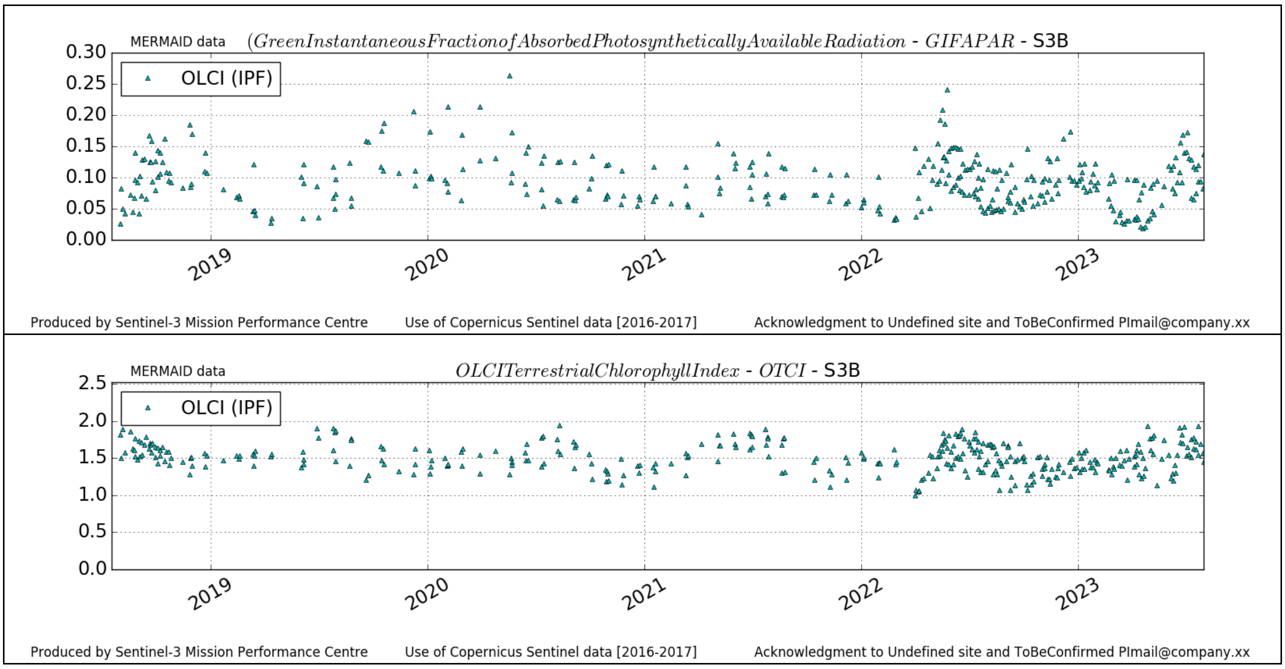

Figure 100: SPAli time series over current report period

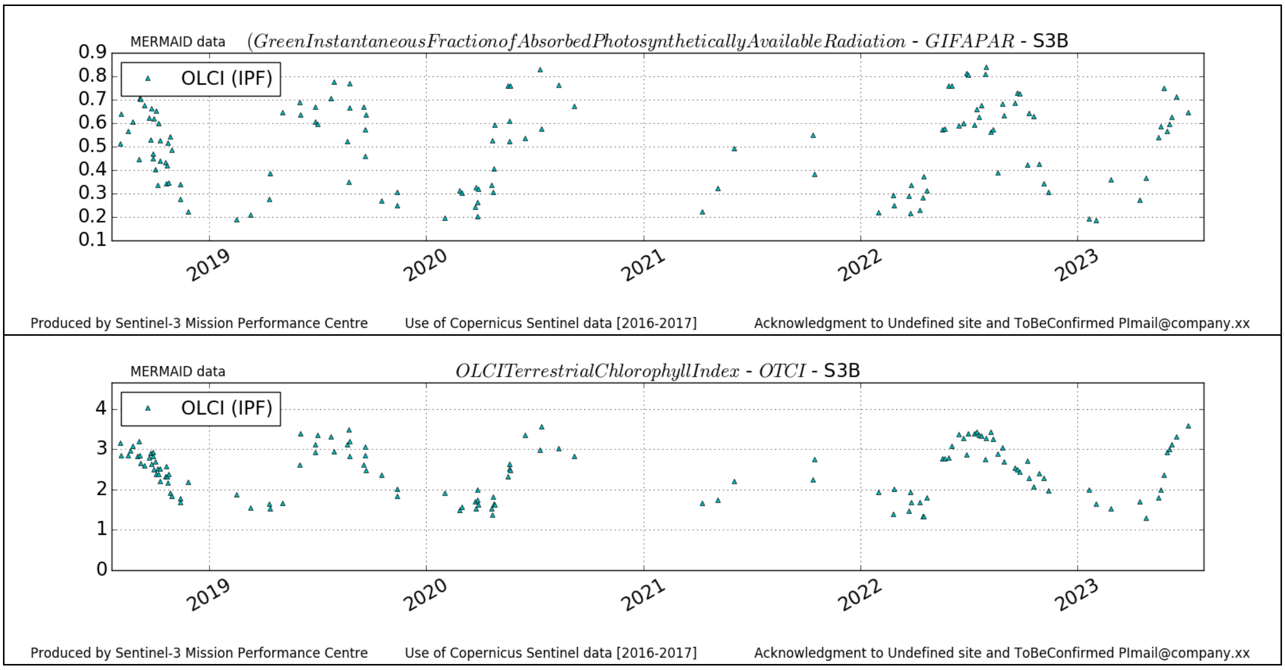

Figure 101: UKNFo time series over current report period

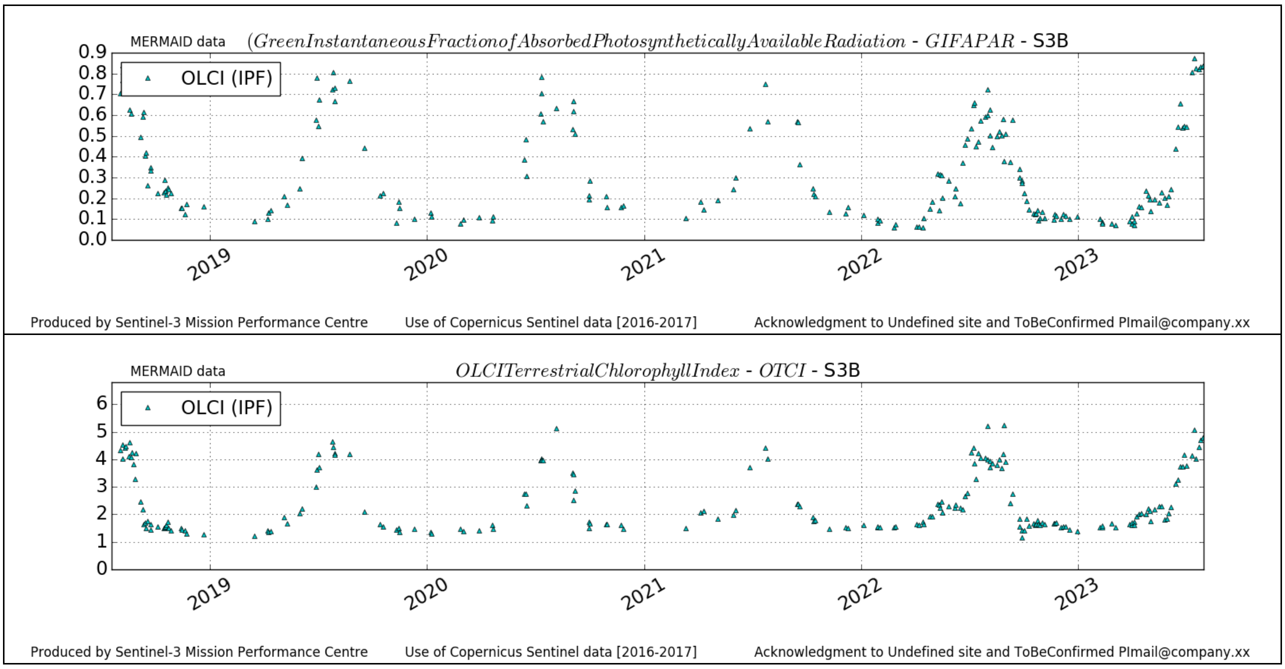

Figure 102: USNe1 time series over current report period

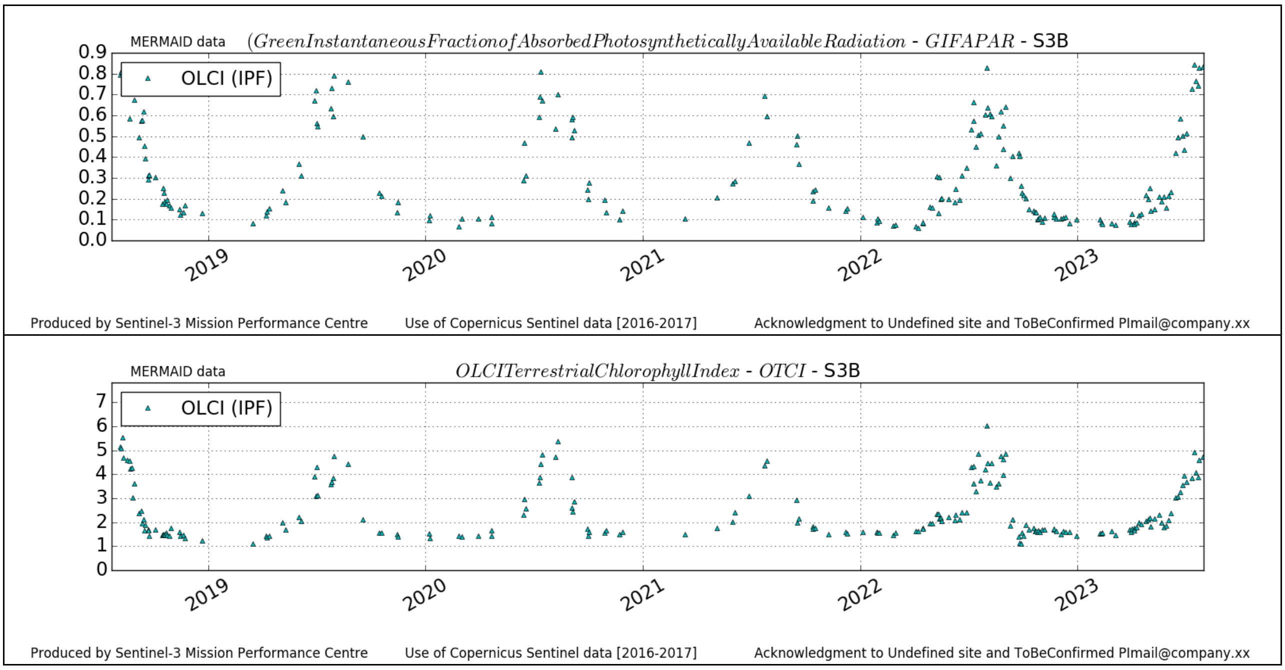

Figure 103: USNe2 time series over current report period

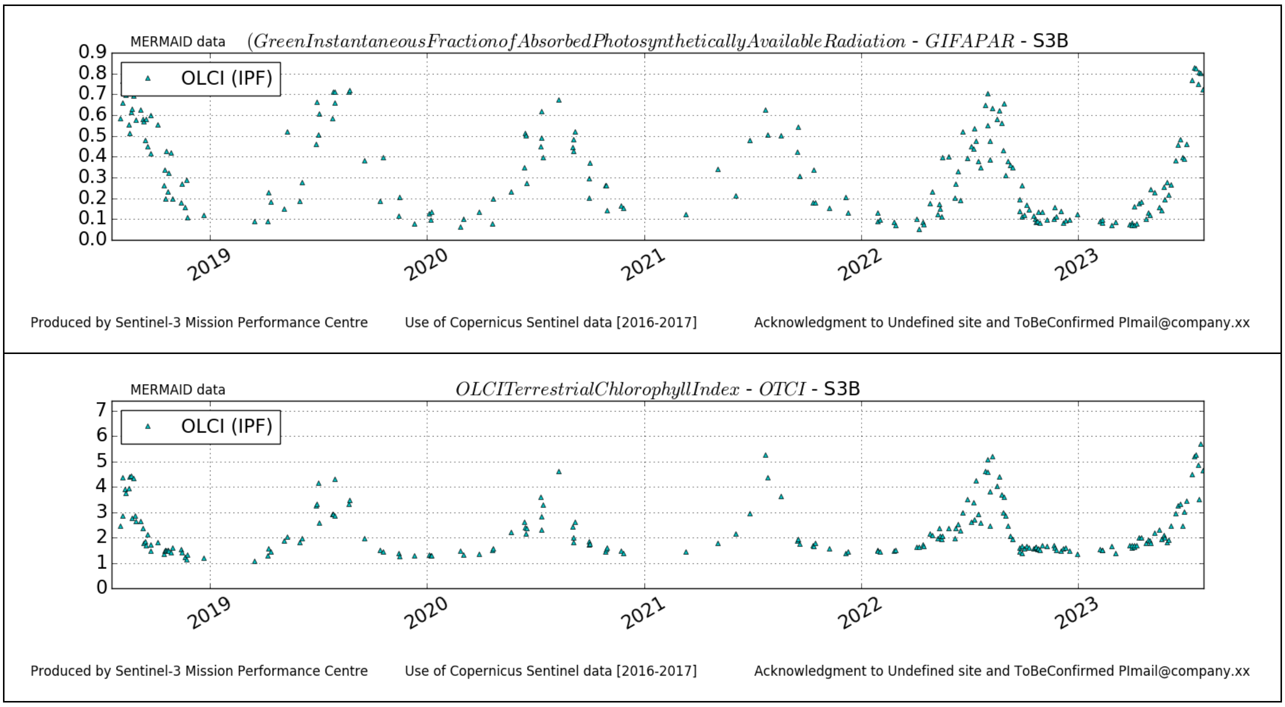

Figure 104: USNe3 time series over current report period

4.1.2 Comparisons with MERIS MGVI and MTCI climatology

This section presents the main results of comparing the Sentinel-3 OLCI Terrestrial Chlorophyll Index (OTCI) and the Envisat MERIS Terrestrial Chlorophyll Index (MTCI). The validation covers from 1st January 2022 to 31st July 2023 over a selection of sites from the S3VT (*Sentinel-3 Validation Team*), CEOS (*Committee for Earth Observation Satellites*) and GBOV (*Ground-Based Observations for Validation*) sites. The sites are distributed across different latitudes and encompass various representative land cover types (Table 6). The analysis relies on monthly L3 Envisat MTCI composites at 1 km spatial resolution, sourced from the UK Centre for Environmental Data Analysis (CEDA).

Figure 105 exhibits the seasonal trends and scatterplots depicting the monthly averages for the period 2002-2012 (MTCI), 2022 (blue), and 2023 (red) at selected sites for S3A. OTCI has consistently demonstrated a close alignment with the monthly MERIS climatology, indicating its ability to maintain continuity in the 10-year MERIS archive and providing confidence in its performance.

The statistical analysis of the comparison between OTCI S3A and MTCI measures reveals R^2 values >0.47 for nearly all the sites, NRMSD <0.2 and biases around 0. A similar strong agreement between the two products is observed for OTCI from S3B, with R^2 >0.31, NRMSD<0.2, and biases around 0 (Figure 106). Additionally, the temporal profiles illustrate similar seasonal trajectories, values and amplitudes.

Table 6: S3VT and CEOS validation sites analysed.

Name	Country	LAT	LON	IGBP
Sp-Ali	Spain	38.45	−1.06	Semi-arid Mediterranean
AUS-Alice Mulga	Australia	-22.28	133.25	Evergreen Needleleaf
FR-Aurade	France	43.54	1.10	Croplands
US-Bartlett	United States	44.06	-71.287	Mixed Forest
US-Blandy	United States	39.06	-78.07	Deciduous Broadleaf
CZ-Bily Kriz forest	Czechia	49.50	18.53	Evergreen Needleleaf
BE-Brasschaat	Belgium	51.30	4.51	Evergreen Needleleaf
AUS-Calperum Malle	Australia	-34.00	140.58	Shrubland
AUS-Cape Tribulation	Australia	-16.10	145.37	Evergreen Needleleaf
It-Castelporziano	Italy	41.70	12.35	Mixed Forest
It-Cat	Italy	37.27	14.88	Croplands (Orange)
US-Central Plains	United States	40.815	-104.74	Grasslands
IT-Collelongo	Italy	41.84	13.58	Deciduous broadleaved, deciduous, closed
AUS-Cumberland Plain	Australia	-33.61	150.72	Evergreen Broadleaf
US-Dead Lake	United States	32.54172	-87.8039	Mixed Forest
US-Disney	United States	28.12504	-81.4363	Shrublands
FR-Estrees	France	49.87	3.02	Croplands
De-Geb	Deutschland	51.10	10.91	Croplands
US-Guanica	United States	17.96	-66.868	Mixed Forest
AUS-Great Western	Australia	-30.19	120.65	Shrublands
GE-Hainich	Germany	51.07	10.45	Mixed Forest
US-Harvard	United States	42.53	-72.17	Mixed Forest
FR-Hesse	France	48.67	7.06	Deciduous Broadleaf
DE-Hones Holtz	Deutschland	52.08	11.22	Deciduous Broadleaf
It-Isp	Italy	45.81	8.63	Mixed Forest
US-Jones	United States	31.19	-84.46	Evergreen Needleleaf
US-Jornada	United States	32.59	-106.84	Open shrubland
US-Konza	United States	39.11	-96.61	Croplands
US-Lajas	United States	18.02	-67.07	Grasslands
IT-Lison	Italy	45.74	12.75	Croplands
AUS-Litchfield	Australia	-13.18	130.79	Evergreen Broadleaf
NE-Loobos	Netherlands	52.16	5.74	Evergreen Needleleaf
US-Moab	United States	38.24	-109.38	Shrublands
FR-Montiers	France	48.53	5.31	Deciduous Broadleaf
US-Mountain Lake	United States	37.37	-80.52	Deciduous Broadleaf
US-Niwot	United States	40.05	-105.58	Evergreen Needleleaf
US-Oak	United States	35.96	-84.28	Mixed Forest
US-Onaqui	United States	40.17	-112.45	Shrublands
US-Ordway	United States	29.68	-81.9934	Evergreen Needleleaf
FR-Puechabon	France	43.74	3.59	Evergreen Needleleaf
AUS-Robson Creek	Australia	-17.11	145.63	Mixed Forest
AUS-Rushworth	Australia	-36.75	144.96	Deciduous Broadleaf
DE-Selhausen	Deutschland	50.86	6.44	Cropland
US-Smithsonian Conservation Biology (SCBI)	United States	38.89	-78.13	*Mixed Forest*
US-Smithsonian Environmental (SERC)	United States	38.89	-76.56	*Croplands*
US-Steigerwaldt	United States	45.50	-89.58	*Deciduous Broadleaf*
It-Sro	Italy	43.72	10.28	*Pinus Pinea*
US-Talladega	United States	32.95	-87.39	Evergreen Needleleaf
DE-Tharandt	Deutschland	50.96	13.56	Evergreen Needleleaf
It-Tra	Italy	37.64	12.85	Croplands (Vineyards and olive trees)
AUS-Tumbarumba	Australia	-35.65	148.15	Evergreen Broadleaf
USNe1	United States	41.165	-96.47	Croplands
USNe2	United States	41.16	-96.47	Croplands
USNe3	United States	41.17	-96.43	Croplands

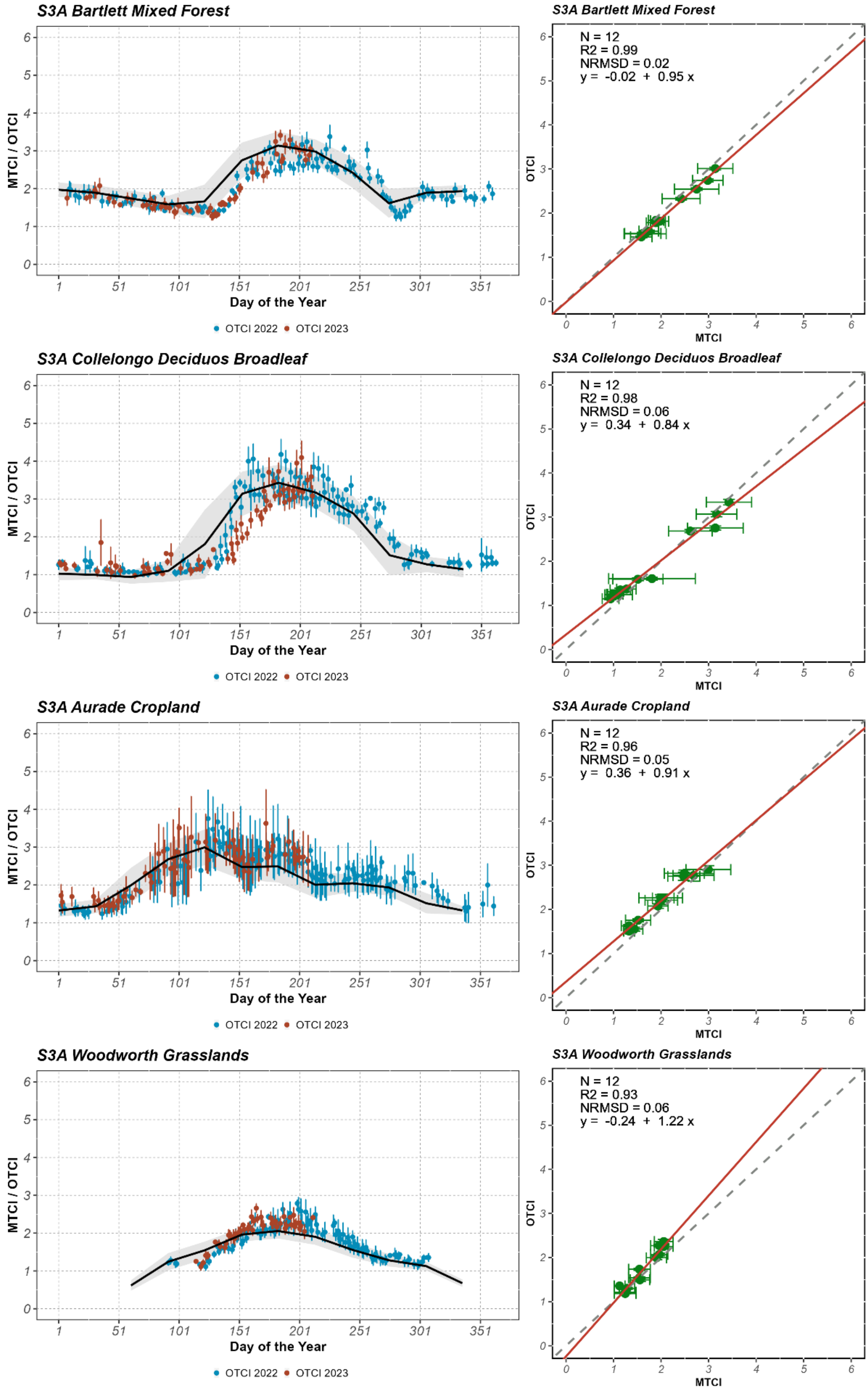

Figure 105: Time series (left) of the OTCI and S3A and a corresponding scatterplot (right) of the monthly mean for sites Bartlett, Collelongo, Aurade and Woodworth

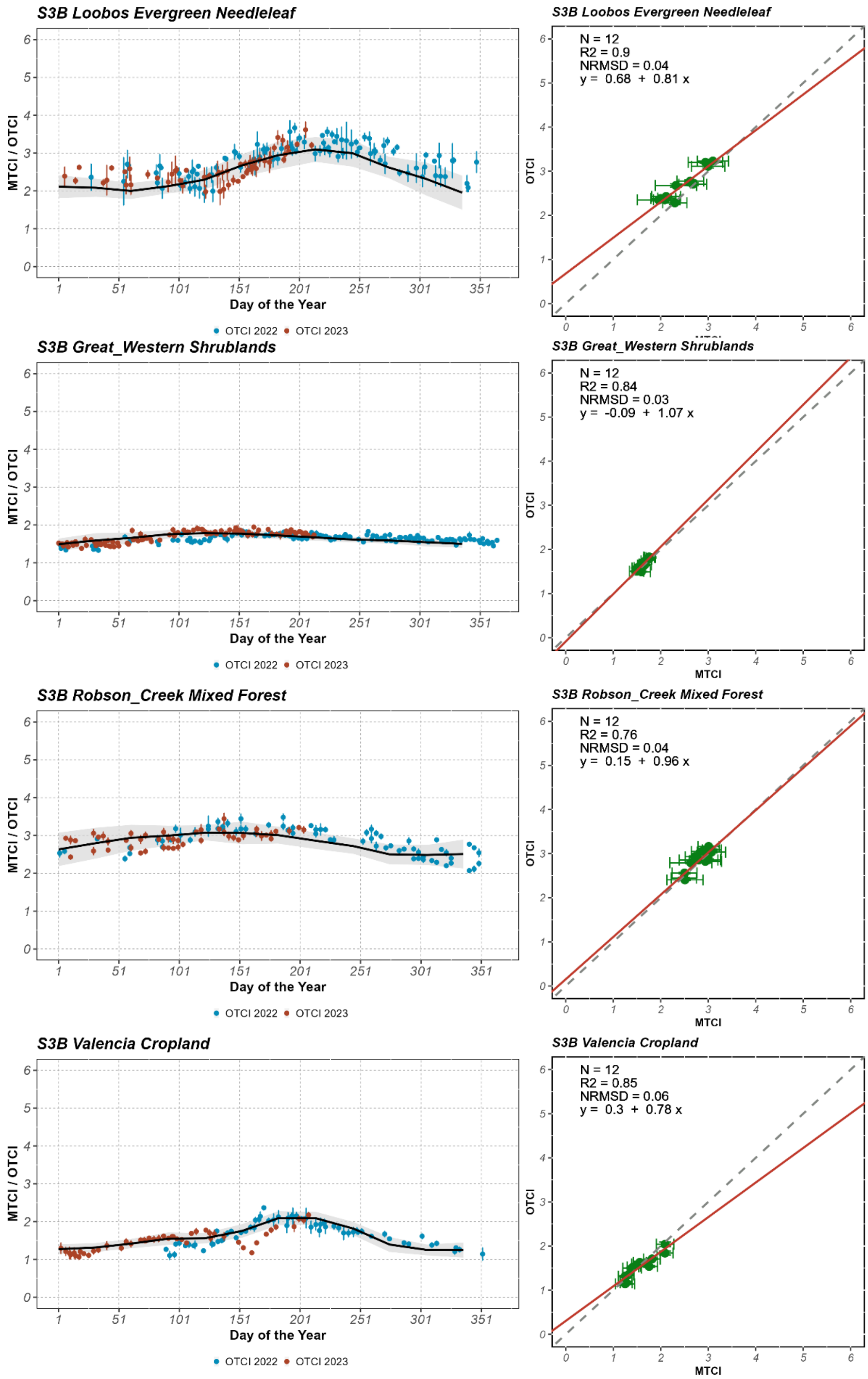

Figure 106: Time series (left) of the OTCI and S3B and a corresponding scatterplot (right) of the monthly mean for the sites Loobos, Great Western, Robson Creek and Valencia

4.1.3 Comparisons with GBOV (Ground-Based Observations for Validation) data v3

There has been no new result during the reporting period. The last figures (reported in OLCI Data Quality Report covering January 2023) are considered valid.

4.1.4 Sentinel-3A and 3B biophysical variables inter-annual variability results

Monthly mean GIFAPAR and OTCI were computed from S3A and S3B MERMAID extractions for all years where data were available over the core CEOS, S3VT and GBOV sites (Table 6). Annual temporal profiles have been created to assess GIFAPAR and OTCI variability between years and compare the agreement between S3A and S3B.

Monthly mean GIFAPAR and OTCI were computed from S3A and S3B MERMAID extractions for all years where data were available over the core CEOS, S3VT and GBOV sites (Table 6). Annual temporal profiles have been created to assess GIFAPAR and OTCI variability between years and compare the agreement between S3A and S3B.

The interannual variability of GIFAPAR and OTCI differs among the selected sites. Several locations, such as Smithsonian SCB, display a relatively steady pattern in values, seasonal patterns, and the timing of peak occurrences (Figure 107). Contrarily, several sites like Zigzag Creek exhibit more significant variability between years, with fluctuating peaks and valleys throughout the year (Figure 108). S3A and S3B exhibit similarities, with similar seasonal trends observed for GIFAPAR and OTCI and similar ranges of values.

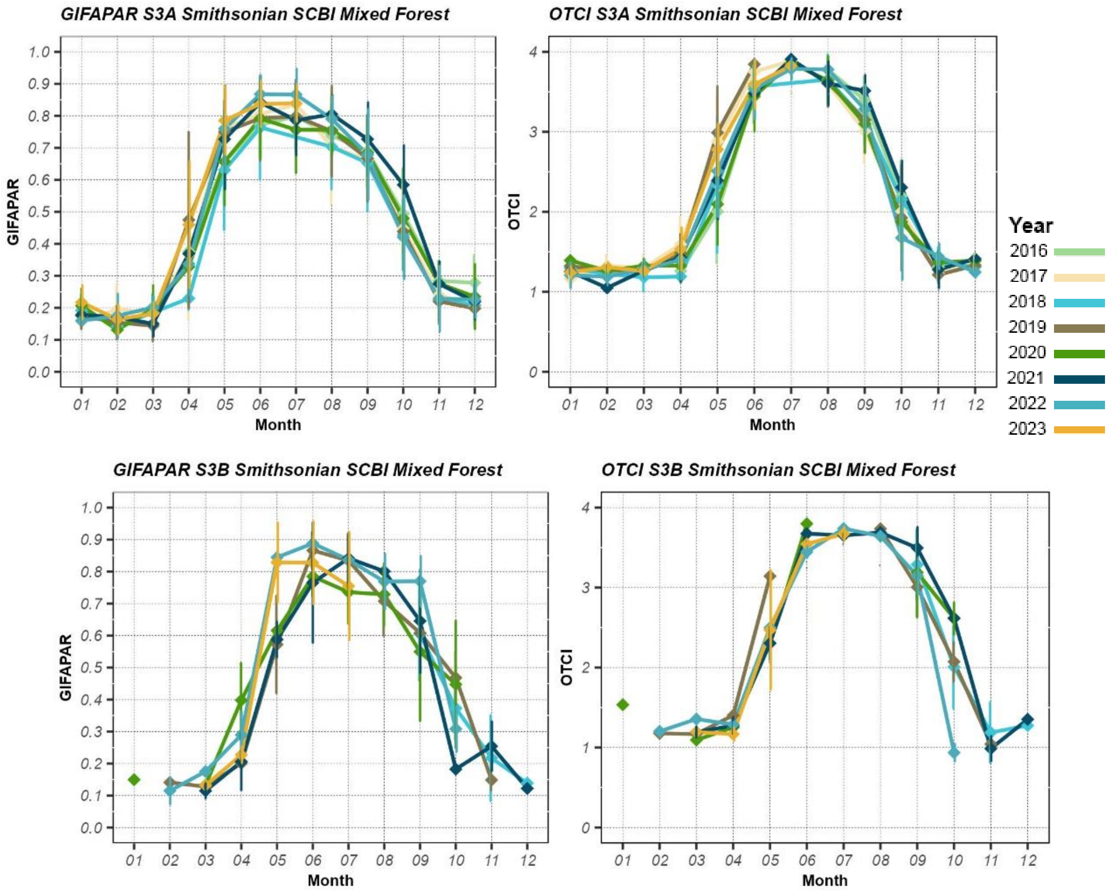

Figure 107: Time series of monthly mean GIFAPAR (left) and OTCI (right) for S3A (top) and S3B (bottom) for Smithsonian SCBI.

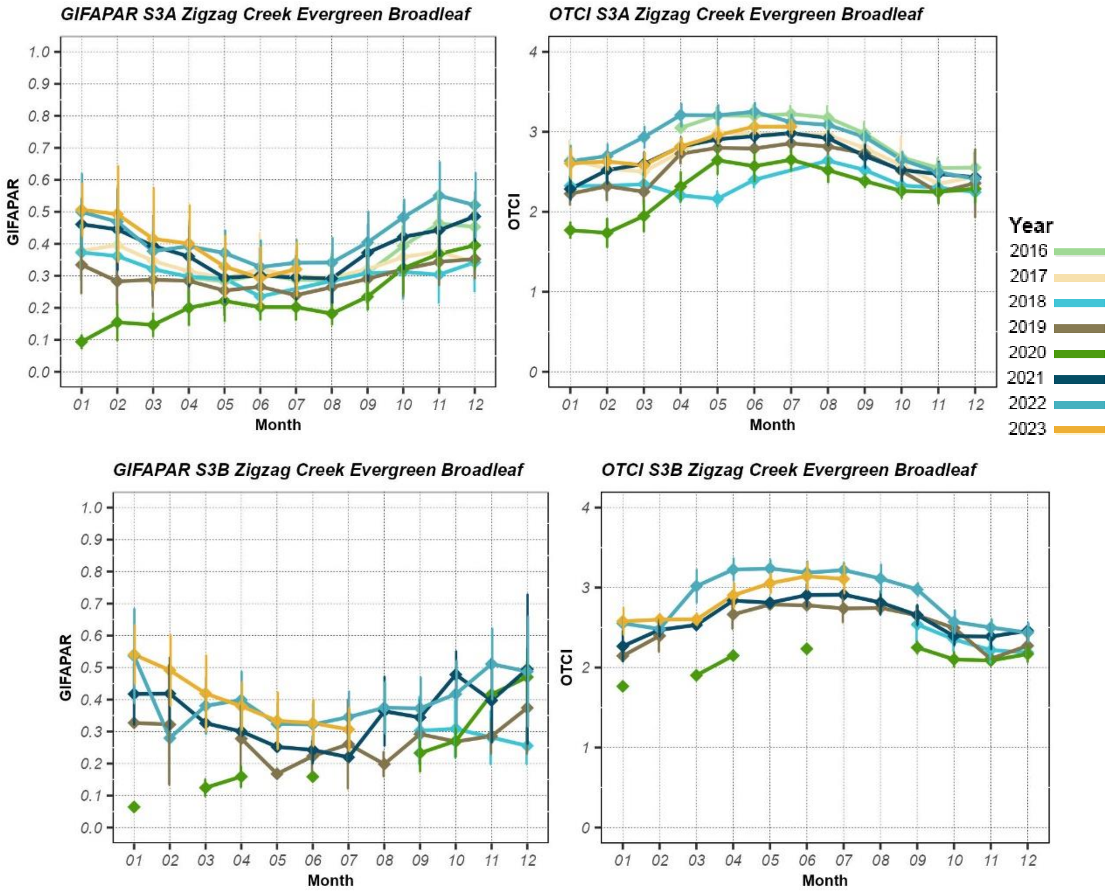

Figure 108: Time series of monthly mean GIFAPAR (left) and OTCI (right) for S3A (top) and S3B (bottom) for Zigzag Creek.

4.2 [OLCI-L2LRF-CV-410 & OLCI-L2LRF-CV-420] – Cloud Masking & Surface Classification for Land Products

For the July 2023 reporting the prototype validation results for OLCI cloud mask using sky cameras (SC) are based on two sites, currently validated independently. The two sites are located at La Sapienza University in Rome, Italy and at the University of Valencia in Spain.

For the Rome site the validation was switched to SC 2, due to some instabilities in azimuth location of SC1. Meaning, the camera rotated horizontally over time.

The coordinates of SC 2 at La Sapienza University are:

- Lat: 41.90148
- Lon: 12.51575

The coordinates of the location of SC 1 at University of Valencia are:

- Lat: 39.50832
- Lon: -0.42084

The sun being close to nadir in the SC image still leads to some overestimation of clouds in the SC data. A method to hopefully reduce this effect is currently still under development.

4.2.1 Sky Camera based validation – prototype results July 2023

4.2.1.1 Rome

Figure 113 and Figure 114 show the prototype validation results for the Rome site in July 2023. The weather in July around Rome is completely dry, with occasional occurrence of cloudy days (see Figure 109 and Figure 110).

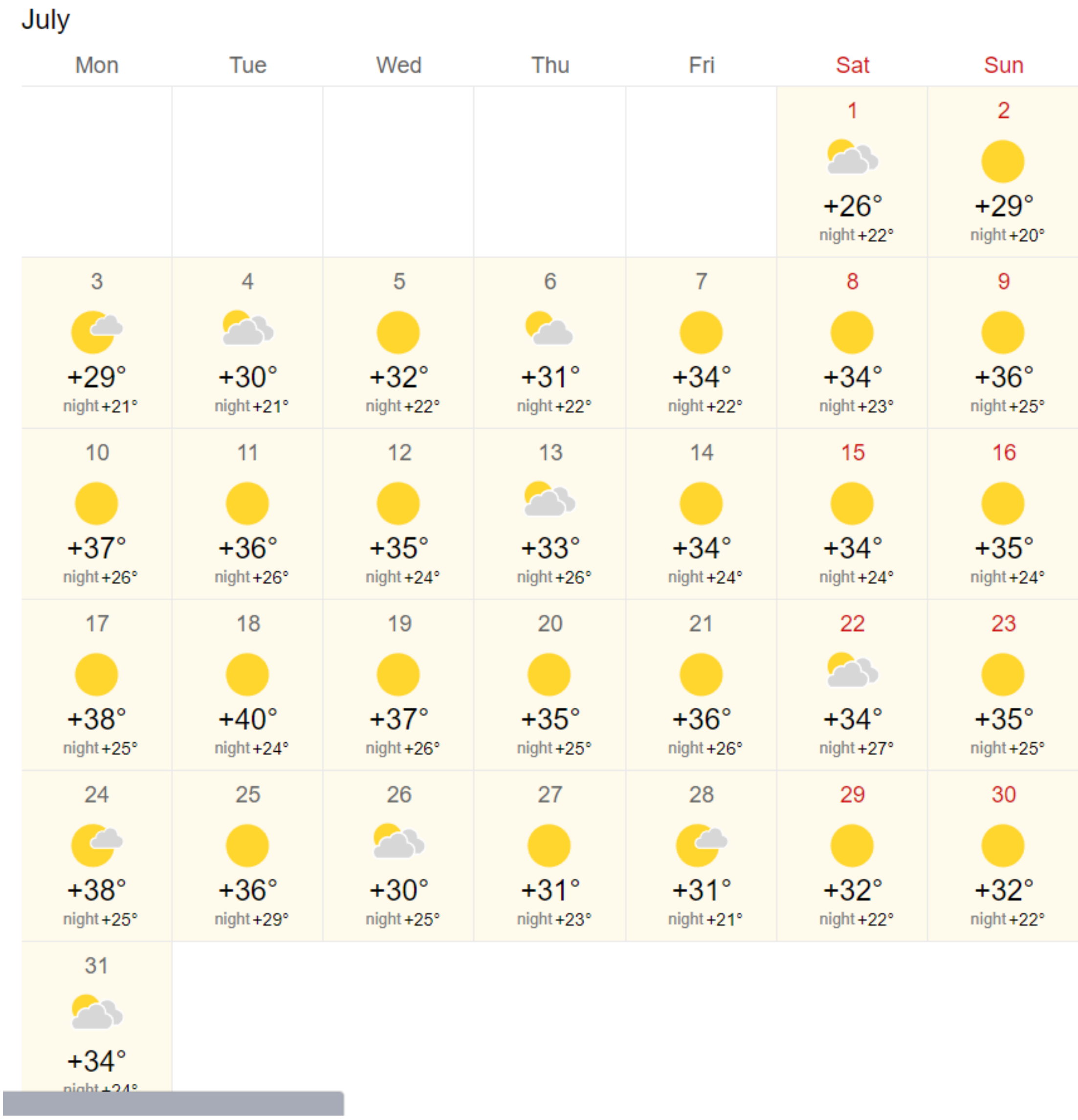

Figure 109: Temperature and cloud cover Rome, July 2023 (source: https://world-weather.info/forecast/italy/rome/July-2023/)

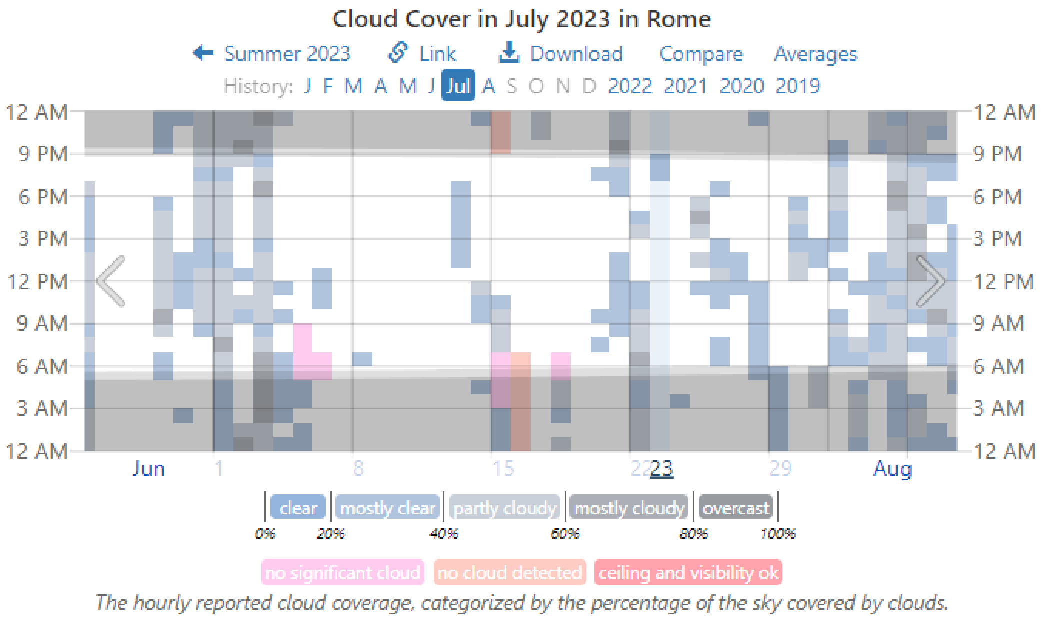

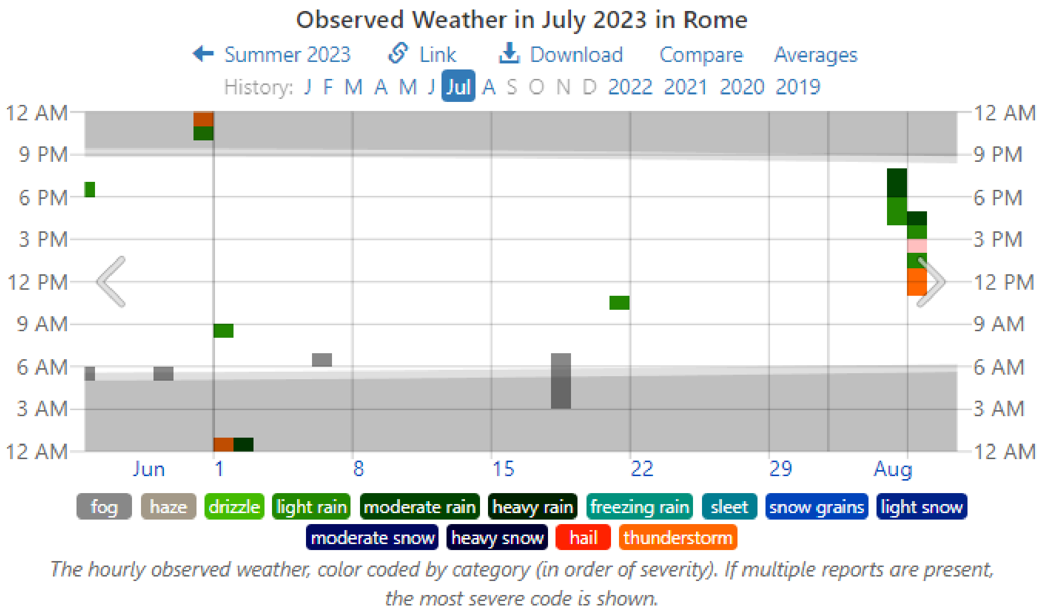

Figure 110: Cloud observations and precipitation Rome, July 2023 (source: https://weatherspark.com/h/m/71779/2023/6/Historical-Weather-in-July-2023-in-Rome-Italy)

Since March 2023 a new method was introduced to automatically remove all matchups between the SC images and the OLCI observation with OZA above 30°.

In July, there have been 15 acquisitions below 30 degree OZA. As shown in the previous months, the high sun elevations in combination with no physical shading device on the sky cameras leads to high sun interference. Nevertheless, the July reference does not show a cloud bias, maybe a little bit of clear bias.

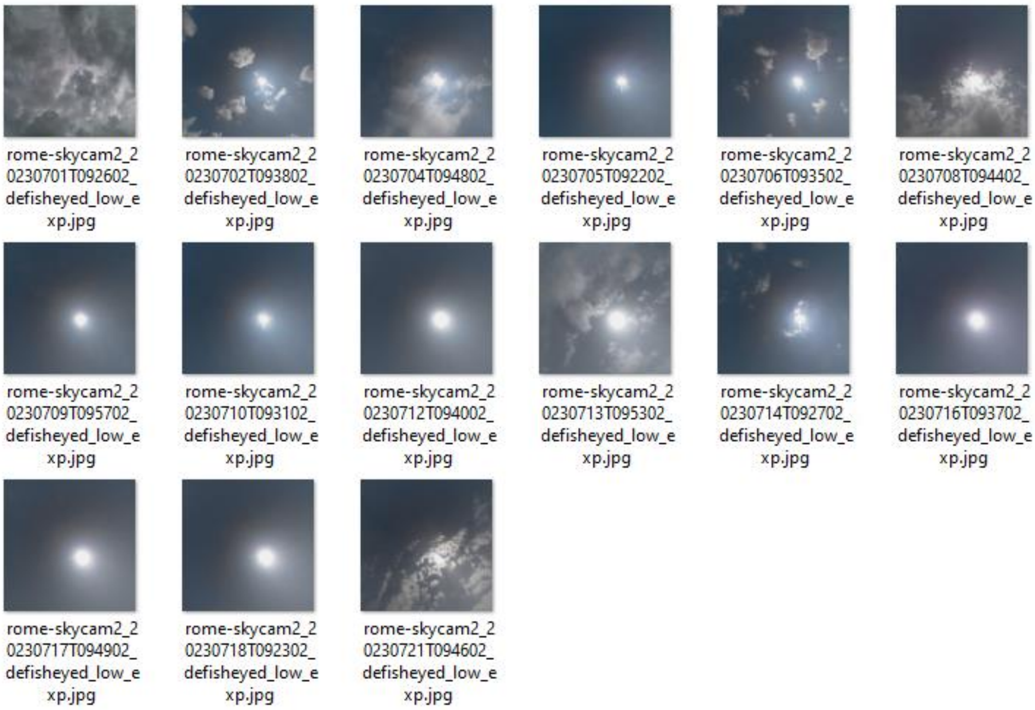

Figure 111: Sky camera acquisitions over Rome during Sentinel-3 OLCI overpass

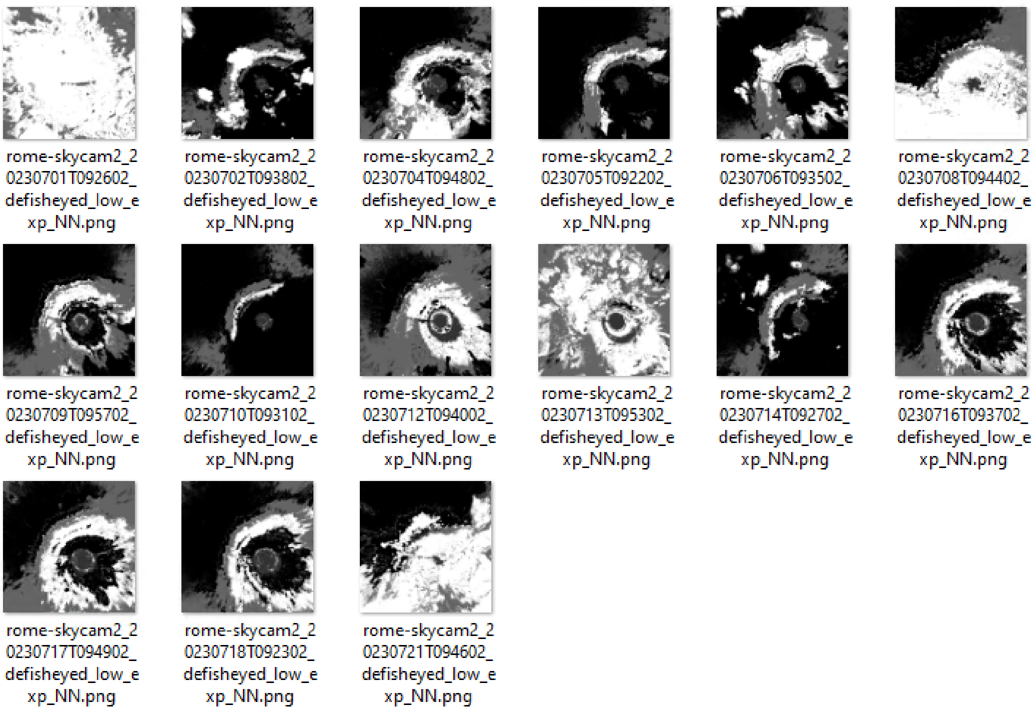

Figure 112: Classified sky camera acquisitions over Rome during Sentinel-3 OLCI overpass

The confusion matrices in Figure 113 shows the validation results for the OLCI cloud flags including the margin. Only OLCI observations with a OZA below 30 have been considered to lower the influence of parallax between the OLCI observation and the SC observation.

When neglecting the margin (see Figure 114) the performance is nearly the same.

Rome SC 2 autom. classif. vs. OLCI L2 LFR Cloud & Ambiguous & Margin
July 2023
Sky Camera 1

OLCI L2 LFR

Class	Clear	Cloud	Sum	U A	E
CLEAR	8	3	11	72.7	27.3
CLOUD	2	2	4	50.0	50.0
Sum	10	5	15		
P A	80.0	40.0		OA:	66.67
E	20.0	60.0		BOA:	60.0

Scotts Pi: 0.206
Krippendorfs alpha: 0.232
Cohens kappa: 0.21

Figure 113: Confusion matrix showing validation results for OLCI L2 cloud screening including margin against SC2 automated classification.

Rome SC 2 autom. classif. vs. OLCI L2 LFR Cloud & Ambiguous
July 2023
Sky Camera 1

OLCI L2 LFR

Class	Clear	Cloud	Sum	U A	E
CLEAR	9	4	13	69.2	30.8
CLOUD	1	1	2	50.0	50.0
Sum	10	5	15		
P A	90.0	20.0		OA:	66.67
E	10.0	80.0		BOA:	55.0

Scotts Pi: 0.068
Krippendorfs alpha: 0.099
Cohens kappa: 0.117

Figure 114: Confusion matrix showing validation results for OLCI L2 cloud screening excluding margin against SC1 automated classification.

4.2.1.2 Valencia

Figure 119 and Figure 120 show the prototype validation results for the Valencia site in July 2023. The weather in July around Valencia is very arid, with occasional cloud covered days (see Figure 115 & Figure 116).

July

Mon	Tue	Wed	Thu	Fri	Sat	Sun
					1 +29° night +23°	2 +30° night +24°
3 +30° night +25°	4 +30° night +24°	5 +28° night +24°	6 +28° night +25°	7 +28° night +25°	8 +30° night +24°	9 +31° night +26°
10 +30° night +26°	11 +32° night +26°	12 +31° night +26°	13 +29° night +26°	14 +31° night +27°	15 +32° night +27°	16 +29° night +27°
17 +30° night +27°	18 +33° night +26°	19 +32° night +26°	20 +31° night +27°	21 +30° night +26°	22 +30° night +27°	23 +32° night +28°
24 +36° night +27°	25 +30° night +27°	26 +29° night +27°	27 +31° night +26°	28 +31° night +27°	29 +33° night +27°	30 +30° night +26°
31 +31° night +28°						

Figure 115: Temperature and cloud cover Valencia, July 2023 (source: https://world-weather.info/forecast/spain/valencia/July-2023/)

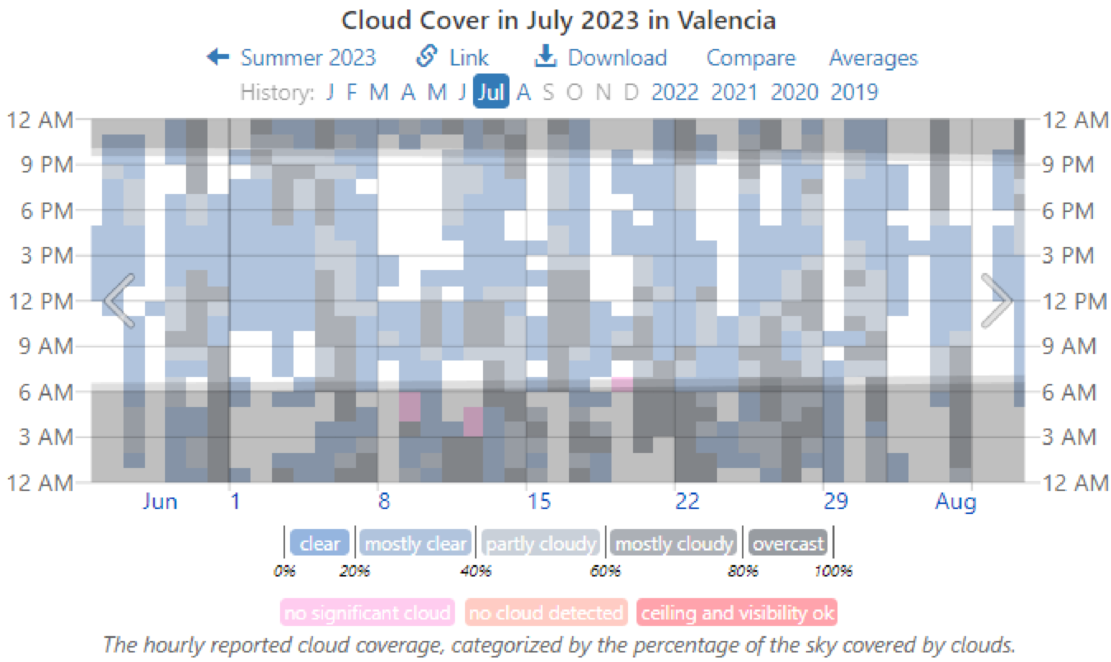

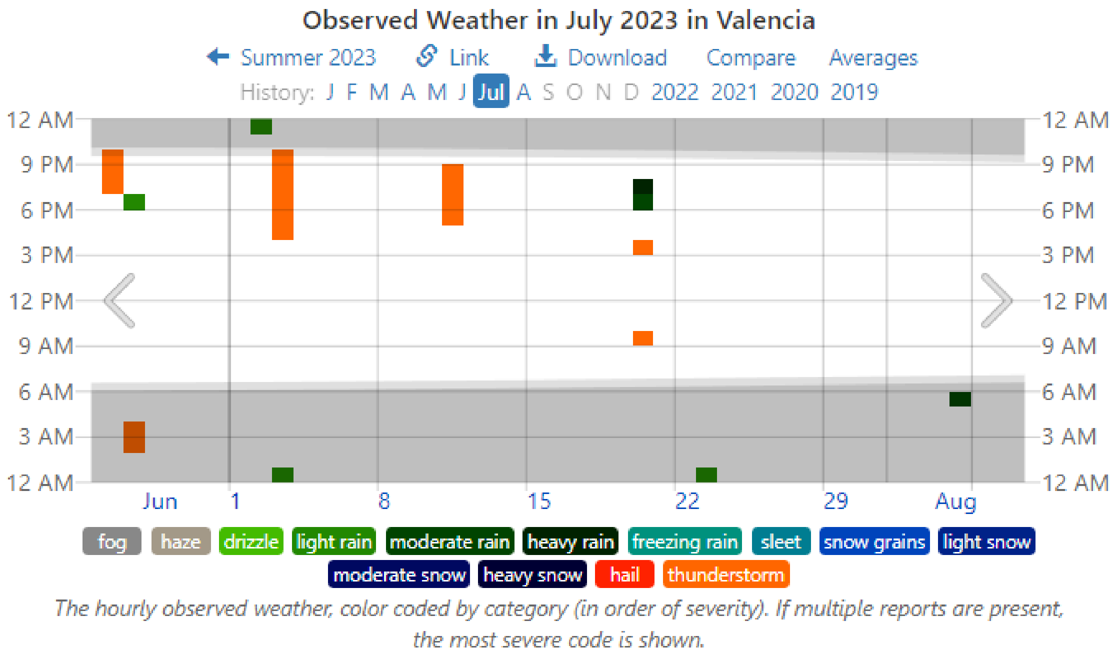

Figure 116: Cloud observations and precipitation Valencia, July 2023 (source: https://weatherspark.com/h/m/42614/2023/6/Historical-Weather-in-July-2023-in-Valencia-Spain#Figures-CloudCover)

Only 5 of the SC observation show clear sky conditions (see Figure 117). Since the sun is close to the centre of all acquisitions, the SC classification (see Figure 118) show a bit of cloud bias. When the majority of the reference window, used for the classification, is classified as sun, those observations are not used for the comparison. Leading to only 11 out of 15 comparable matches.

Figure 117: Sky camera acquisitions over Valencia during Sentinel-3 OLCI overpass

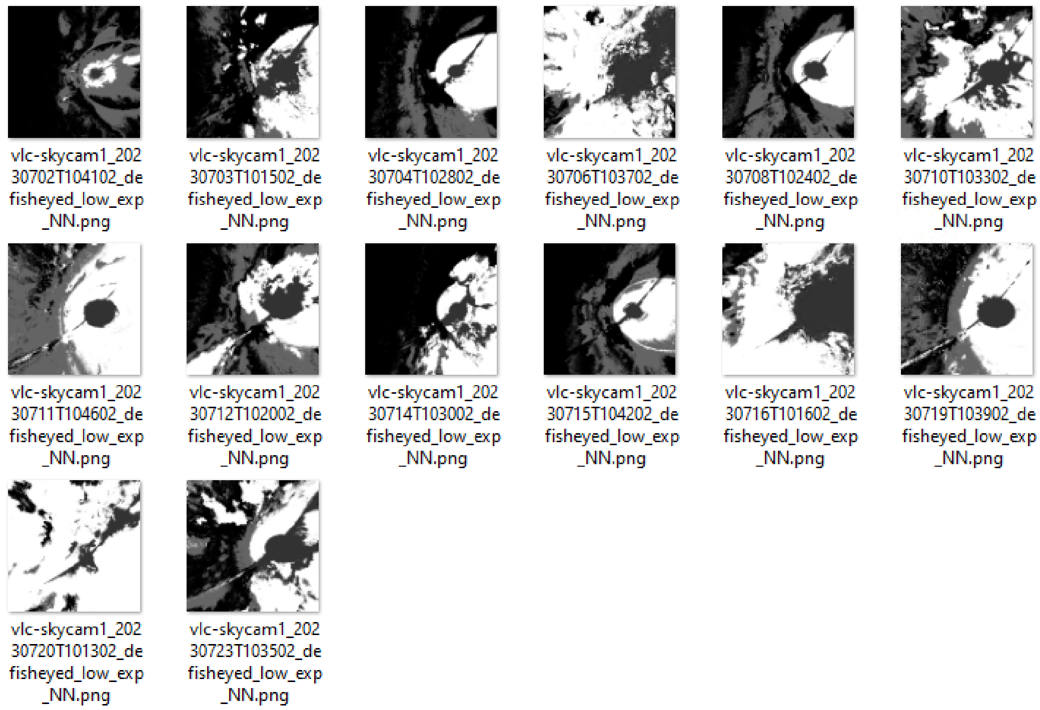

Figure 118: Classified sky camera acquisitions over Valencia during Sentinel-3 OLCI overpass

Figure 119 shows the validation results for the OLCI cloud flags including the margin. Only OLCI observations with a OZA below 30 have been considered to lower the influence of parallax between the OLCI observation and the SC observation. When including the margin, the OLCI and SC classifications match only 54% (OA)

When neglecting the margin (see Figure 120) the results stay comparable.

The high sun elevation seems to cause issues for the validation method.

Valencia SC 1 autom. classif. vs. OLCI L2 LFR Cloud & Ambiguous & Margin
July 2023
Sky Camera 1

OLCI L2 LFR

Class	Clear	Cloud	Sum	U A	E
CLEAR	2	4	6	33.3	66.7
CLOUD	1	4	5	80.0	20.0
Sum	3	8	11		
P A	66.7	50.0		OA:	54.55
E	33.3	50.0		BOA:	58.35

Scotts Pi: 0.059
Krippendorfs alpha: 0.102
Cohens kappa: 0.126

Figure 119: Confusion matrix showing validation results for OLCI L2 cloud screening including margin against SC1 automated classification.

Valencia SC 1 autom. classif. vs. OLCI L2 LFR Cloud & Ambiguous
July 2023
Sky Camera 1

OLCI L2 LFR

Class	Clear	Cloud	Sum	U A	E
CLEAR	3	5	8	37.5	62.5
CLOUD	0	3	3	100.0	0.0
Sum	3	8	11		
P A	100.0	37.5		OA:	54.55
E	0.0	62.5		BOA:	68.75

Scotts Pi: 0.09
Krippendorfs alpha: 0.132
Cohens kappa: 0.246

Figure 120: Confusion matrix showing validation results for OLCI L2 cloud screening excluding margin against SC1 automated classification.

5 Validation of Integrated Water Vapour over Land & Water

We continuously investigate the temporal evolution of quality measures of integrated water vapour, when comparing SUOMI NET (Ware et al. 2000) with reduced resolution data of OLCI L2 non-time-critical. All data until March 2022 has been acquired from EUMETSAT CODA, all data from Apr 2022 on has been downloaded from EUMETSAT's datastore (collection id: EO:EUM:DAT:0410).

731.600 (OLCI-A) and 420.400 (OLCI-B) potential matchups within the period of June 2016 (OLCI-A) January 2019 (OLCI-B) to end of July 2023 have been analysed. The global service of SUOMI-NET has been reduced at the end of 2018; thus OLCI-B colocations are less frequent outside North America.

For the cloud detection, the standard L2 cloud-mask has been applied (including the cloud ambiguous and cloud margin flags). The comparison of OLCI and GNSS shows a very high agreement (Figure 121).

The correlation between both quantities is around 0.98. The root-mean-squared-difference is 1.9 -2.1 kg/m^2. The systematic overestimation by OLCI is 11%-12%. The bias corrected *rmsd* is around 1.3 kg/m^2.

The temporal evolution of several quality measures (Figure 122) , indicates small seasonal variations, which are certainly related to retrieval assumptions.

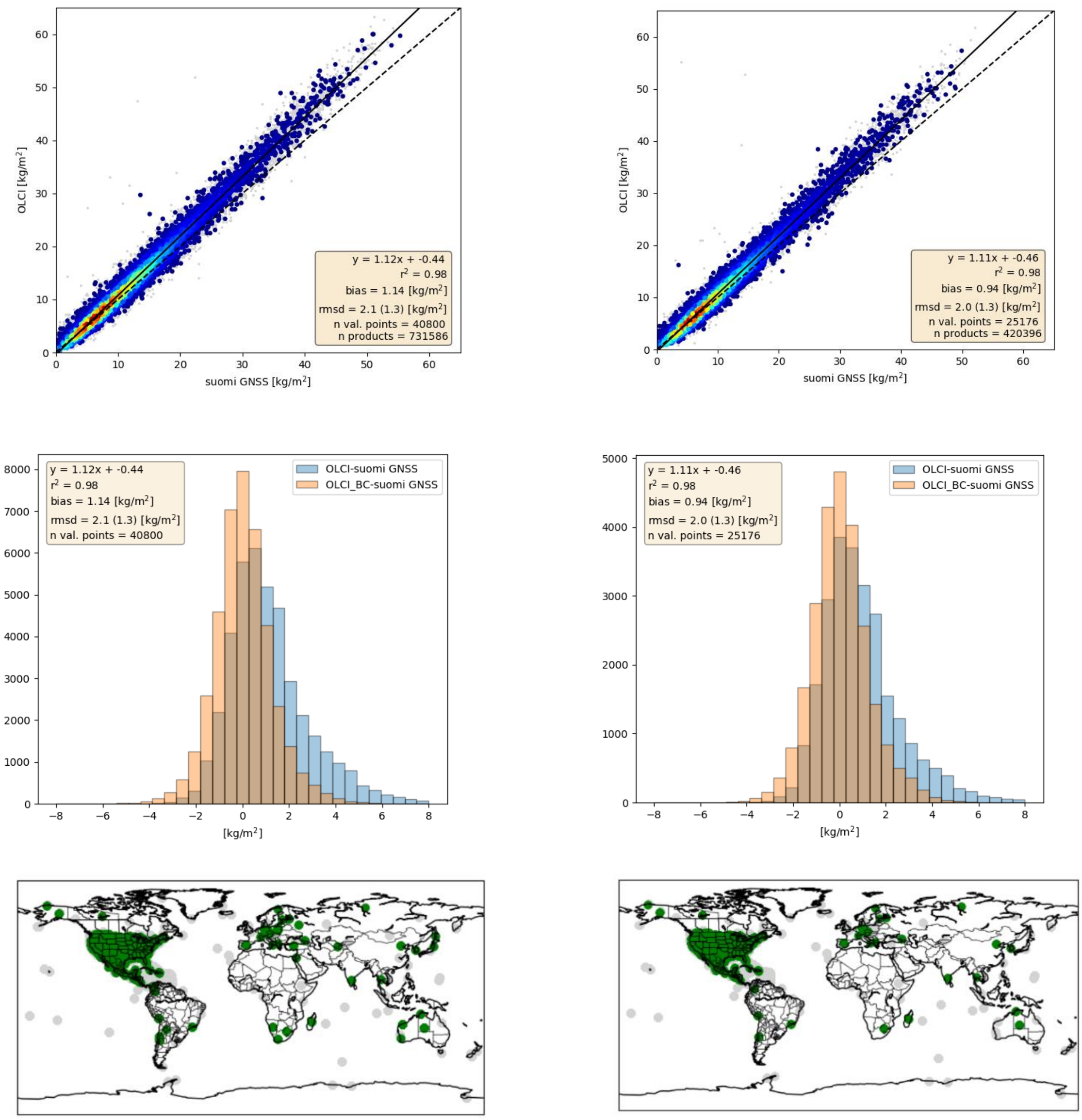

Figure 121: Upper: Scatter plot of the IWV products, derived from OLCI (A left, B right) above land and from SUOMI NET GNSS measurements. Middle: Histogram of the difference between OLCI (A: left, B: right) and GNSS (blue: original OLCI, orange: bias corrected OLCI). Lower: Positions of the GNSS (A: left, B: right).

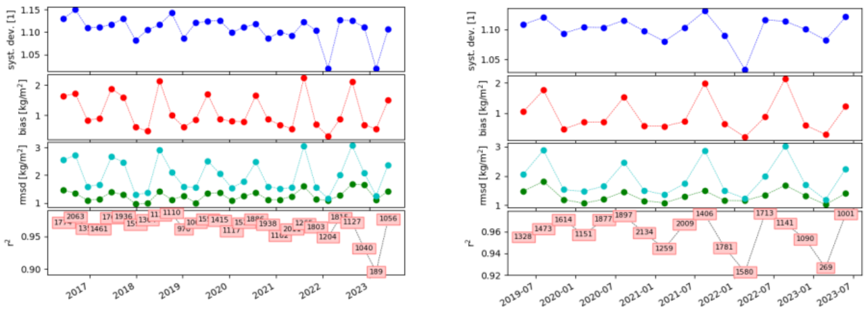

Figure 122: Temporal evolution of different quality measures for OLCI A (left) and OLCI B (right) with respect to SUOMI Net. From top to bottom: systematic deviation factor, bias, root mean squared difference (with and without bias correction), explained variance (number in boxes are the numbers of matchups)

6 Level 2 SYN products validation

6.1 SYN L2 SDR products

There has been no new result during the reporting period. The last figures (reported in OLCI Data Quality Report covering June 2023) are considered valid.

6.2 SY_2_VGP, SY_2_VG1 and SY_2_V10 products

The similarity of SYN VGT like products with the PROBA-V archive is evaluated through intercomparison of 10-daily composites extractions over LANDVAL [1] sites. Since there is no overlap with the PROBA-V nominal operational phase and no PROBA-V Collection 2 climatology is available yet, direct comparison is done by comparing the SY_2_V10 NTC products starting January/2021 with those of PROBA-V S10-TOC since January/2017.

The temporal evolution of statistics results below are based on intercomparison over the entire periods up to July/2023. The scatterplots are based on intercomparison between SY_2_V10 products of July/2023 with PROBA-V Collection 2 S10-TOC products of July/2019.

Products availability

Availability of SY_2_VG1 and SY_2_V10 products is checked through an automated query and download via the Copernicus Data Space Ecosystem feeding the products database Belgian Collaborative Ground Segment (Terrascope, www.terrascope.be). For the month July/2023, there are missing data or empty files for:

- S3A_SY_2_VG1____20230706T000000_20230706T235959_*
- S3A_SY_2_VG1____20230707T000000_20230707T235959_*
- S3A_SY_2_VG1____20230729T000000_20230729T235959_*.

Statistical consistency

The scatter density plots with geometric mean regression equation, coefficient of determination (R^2) and APU statistics based on intercomparison between SY_2_V10 products of July/2023 with PROBA-V Collection 2 products of July/2019 are shown in Figure 123. The APU statistics are defined as: Accuracy (A) or average bias, Precision (P) or the standard deviation of the bias, and Uncertainty (U) or the Root Mean Squared Distance. Accuracy is best for BLUE (< 1%), less good for RED and NIR (around 2%) and worse for SWIR (up to -6%). The relatively large values for Precision (large scatter, low R^2) are caused by the fact that products of two different years are compared. The disagreement for the RED, NIR and SWIR bands is related to a bug in the spectral resampling. In addition, disagreement for SWIR is influenced by the SLSTR calibration offset (in bands S5 and S6). From 18/07/2023 (for S3B) and 25/07/2023 (for S3A) an updated processing baseline is in operations, including application of SLSTR calibration factors, and aligning the spectral resampling to PROBA-V. As a result, the SWIR scatterplots show large variation.

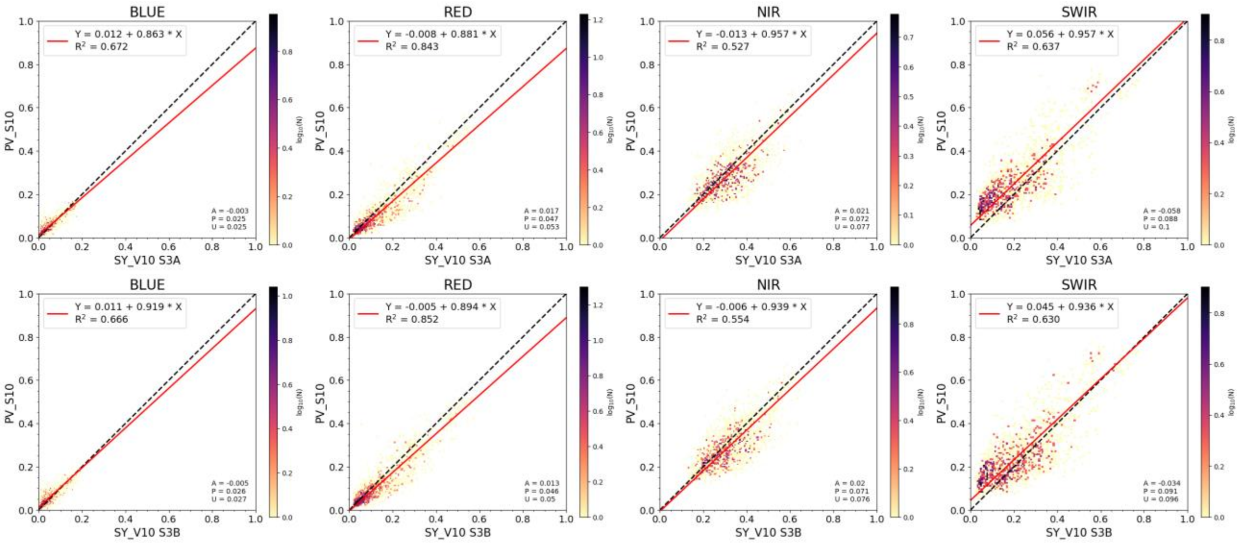

Figure 123: Scatter density plots between SY_V10 S3A (top) or S3B (bottom) and PROBA-V C2 S10-TOC for BLUE, RED, NIR and SWIR bands (left to right), June/2023 vs. June/2020

Temporal consistency

The temporal evolution of APU statistics derived from intercomparison of SY_2_V10 NTC products January/2021 –July/2023 with those of PROBA-V S10-TOC January/2017 – July/2019 (Figure 124). The APU statistics show stable evolution over time, although some seasonal pattern is observed for the mainly the SWIR channel, and to a lesser extent the RED and NIR channel. The temporal behaviour is stable, except for a strong discontinuity for the SWIR band, with improved statistics at the end of July/2023, related to the updated processing baseline with improved SWIR calibration (see above).

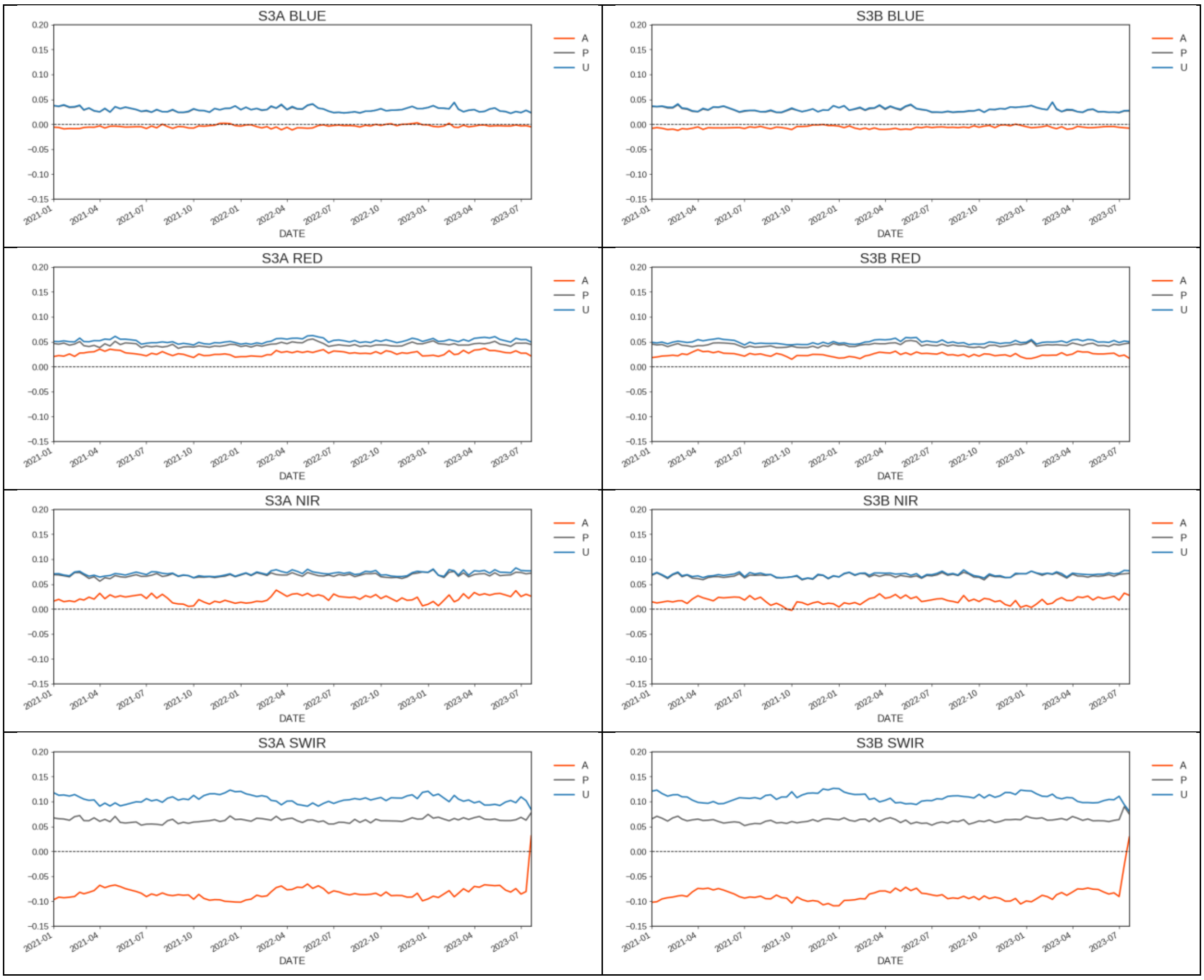

Figure 124: Temporal evolution of APU statistics between SY_2_V10 S3A (left) or S3B (right) and PROBA-V S10-TOC for BLUE, RED, NIR and SWIR bands (top to bottom), January/2021 - June/2023 (S3 SYN VGT) vs. January/2018 - June/2020 (PROBA-V)

Figure 125 shows the temporal evolution of APU statistics derived from the intercomparison of SY_2_V10 NTC products based on S3A with those based on S3B January/2021 –June/2023. The APU statistics show a stable temporal evolution, except for a strong discontinuity for SWIR, related to the different timing of the processing baseline update for S3A resp. S3B (see above).

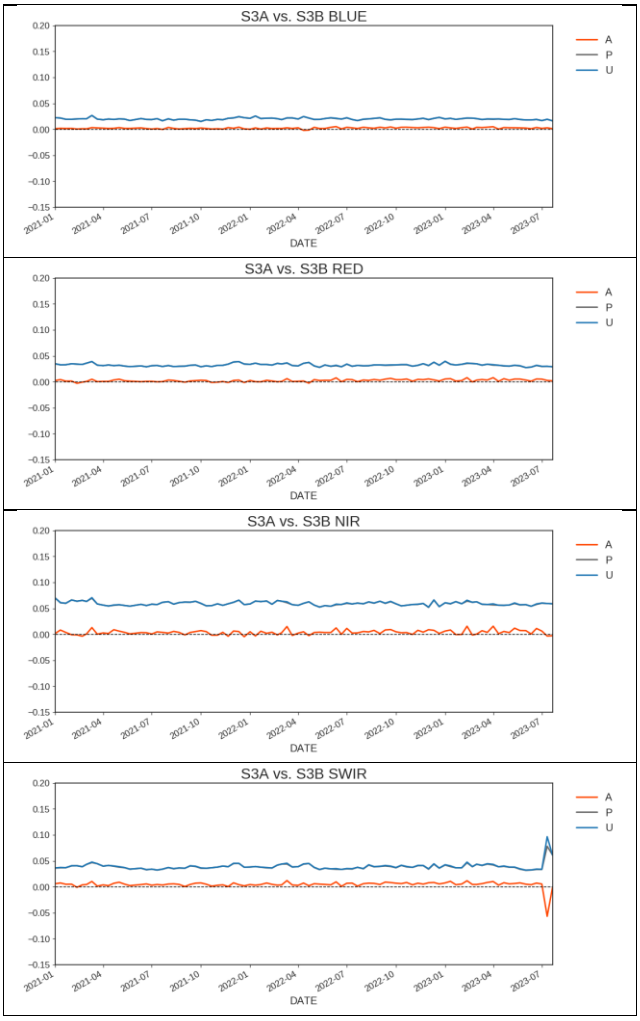

Figure 125: Temporal evolution of APU statistics between S3A_SY_2_V10 and S3B_SY_2_V10 for BLUE, RED, NIR and SWIR bands (top to bottom), January/2021 - July/2023

References

[1] B. Fuster *et al.*, “Quality Assessment of PROBA-V LAI, fAPAR and fCOVER Collection 300 m Products of Copernicus Global Land Service,” *Remote Sens.*, vol. 12, no. 6, p. 1017, Mar. 2020, doi: 10.3390/rs12061017.

6.3 SYN L2 AOD NTC products

There has been no new result during the reporting period. The last figures (reported in OLCI Data Quality Report covering June 2023) are considered valid.

7 Events

For OLCI-A, three Radiometric Calibration sequences have been acquired during the reported period:

- S01 sequence (diffuser 1) on 06/07/2023 23:28 to 23:30 (absolute orbit 38460)
- S01 sequence (diffuser 1) on 23/07/2023 00:55 to 00:57 (absolute orbit 38689)
- S05 sequence (diffuser 2) on 23/07/2023 02:36 to 02:38 (absolute orbit 38690)

For OLCI-B, three Radiometric Calibration sequences have been acquired during the reported period:

- S01 sequence (diffuser 1) on 09/07/2023 01:19 to 01:21 (absolute orbit 27096)
- S01 sequence (diffuser 1) on 24/07/2023 21:43 to 21:45 (absolute orbit 27322)
- S05 sequence (diffuser 2) on 24/07/2023 23:24 to 23:26 (absolute orbit 27323)

8 Appendix A

All Data Quality Reports, as well as past years Data Quality Reports and Annual Performance Reports, are available on dedicated pages in Sentinel Online website, at:

- https://sentinel.esa.int/web/sentinel/technical-guides/sentinel-2-msi/data-quality-reports
- https://sentinel.esa.int/web/sentinel/technical-guides/sentinel-3-olci/data-quality-reports
- https://sentinel.esa.int/web/sentinel/technical-guides/sentinel-3-slstr/data-quality-reports
- OPT Annual Performance Report Year 2022 (PDF document)

End of document